Iran Gas Institute

JGT

JOURNAL OF GAS TECHNOLOGY

Volume 2 . May 2017 . www.irangi.org

Journal of Gas Technology, JGT

Volume 2. May 2017

Technical Editor
Mohamad Reza Jafari Nasr

Layout
Mona Ghahari

Cover Design
Sanaz Yousefi

Contact Information
Iranian Gas Institute:
http://www.irangi.org
Journal Email Address:
journalofgastechnology@irangi.org

Table of Contents

A Novel Design for Plate Heat Exchangers in LNG Liquefaction Cycle 4
M.R. Jafari Nasr and E. Mohammadi

Wettability Alteration in Near-Wellbore Regions of Gas Reservoirs to Mitigate Liquid Blockage Using Super Water- and Oil-Repellent ZnO/SiO_2 Nanofluid Treatment 16
Pouriya Esmaeilzadeh, Mohammad Taghi Sadeghi,* and Alireza Bahramian

Asphaltene and Normal Paraffin Effect on Gas-Oil Interfacial Tension During CO_2 Injection into Asphaltenic Oil Reservoir 31
Masoud Riazi, Yousef Kazemzadeh and Rafat Parsei

Reducing Energy Consumption in Gas Purification Plants (MDEA Base) by Retrofit Design 43
Omid Sabbagh, Maissam Vahidi Ferdowsi and Mohammad Ali Fanaei

Utilizing Chemical Looping Combustion instead of Fired-Furnace in a Steam Methane Reforming for Enhancement of Hydrogen Production in a multi Tubular Reactor 50
Sedigheh Kabiri, Mohammadreza Rahimpour

A New Method to an Enhance Separation of Acid Gas from Natural Gas by Mixed Amine Solution 67
Abolfazl Gharibi Kharaji, Vahid Madadi Avergani* and Parviz Darvishi

A Novel Design for Plate Heat Exchangers in LNG Liquefaction Cycle

- M.R. Jafari Nasr and E. Mohammadi
Islamic Azad University, Science and Research Branch, Tehran-Iran.
(Email: nasrmrj@ripi.ir)

Received: Feb 14, 2017 / Accepted: Apr 12, 2017

Abstract

LNG production is an intense and complex process, in which the liquefaction accounts for more than 50% of costs. In recent years, design engineers have been made several attempts to optimize this process. The main objective was to increase the production yield and capacity, and minimize the costs. The most important process equipment in liquefaction stage is devoted to compact heat exchangers of Plate Fin or Spiral Wounded types. This article described the simulation of liquefaction cycle of Iran LNG project with triple mixed refrigerant to provide a new method for designing the plate heat exchanger used in this cycle; in addition, a simple method was introduced for selecting the best secondary surface based on the conceptual development of the volume performance index (VPI). The designed exchanger had the minimum surface area and volume. The reduction of required heat transfer surface area had a significant role in the reduction of investment capital cost in LNG production process.

The liquefaction cycle of Iran LNG was fully investigated in this article as an industrial case. According to the simulation, the cold and hot surface areas of the plate heat exchanger, used in the given process, are as large as 3001m^2 and 1933m^2 with the overall heat transfer coefficient of 425 W/m^{2}K°; whereas, designing this exchanger by developed rapid design algorithm (RDA) significantly can be reduced the required cold and hot surface areas by 5.2 and 3.3 times, respectively. The overall heat transfer coefficient was also increased by 2 times.

Keywords: Liquefied Natural Gas, Volume Performance Index, Rapid Design Algorithm

Introduction

Liquefied natural gas (LNG) is the best and healthiest fuel gas. LNG is an odorless, transparent, and non-toxic liquid with a specific weight of about 0.45 grams per cubic centimeter. It is produced with cooling and liquefying natural gas at around -160°C, under a pressure of about 1atm. The liquefaction of the natural gas decreases its volume by 600 times, which makes its transportation to more remote areas simpler and more cost-effective. Moreover, it produces low amount of combustion-produced pollutants and large amount of combustion-produced energy. LNG consists of a complex and costly process, in which liquefaction accounts for the 50% of the process costs. Several attempts have been made in recent years to improve the performance of this process and to reduce investment costs. In liquefaction stage, the plate fin heat exchanger (PFHE) and spiral wounded heat exchanger (SWGE) are the main elements. These exchangers are substituted for common shell-and-tube exchangers, as they are safer and more cost-effective.

The PFHE is a stack of alternating flat and corrugated (fin) plates. Flows exchange heat through pathways surrounded by corrugated sheets separated by flat plates. Fins are used as surfaces for secondary heat transfer and a mechanical barrier against intra-layer pressure. There are different types of fins that allow optimal design of these exchangers in terms of cost, weight, thermal efficiency, and/or pressure drop. The fin-plate heat exchangers are superior to other types of heat exchangers, due to having several advantages including small temperature difference between the cold-and-hot fluids, high thermal efficiency, large heat transfer surface area per unit of volume (almost 1000m^3), low weight, and the feasibility of heat exchange between different flows [2].

Several attempts have been made by process design engineers in recent years to improve the performance of compact heat exchangers, especially for cooling, through developing modern designs. Among the most important causes are saving energy, cost, and equipment space which should be taken into account by design engineers before other things [3]. Therefore, they look for strategies to develop optimal designs, increase efficiency, and finally reduce costs.

In this article attempts were made to take a fresh step towards improving LNG production through optimization of the main element of LNG liquefaction cycle (compact plate-fin exchanger) with a modern design method. To this end, liquefaction cycle of Iran LNG project with pre-cooled propane along with the triple mixed refrigerant was simulated using Aspen HYSYS. This simulation was done to extract data of compact heat exchanger's inflows in this cycle, and to obtain the overall surface areas of the cold and hot sides, as well as the overall coefficient of heat transfer. Using this information and modern design method, the exchanger was optimally designed. This method is based on a thermo-hydraulic model (RDA) that shows the relationship of pressure drop, heat transfer coefficient, and exchanger volume. Given that the maximum pressure drop is considered as the objective of design in RDA, a smaller surface area is obtained. This reduction in the surface of exchanger has a major role in decreasing investment costs. In addition, a simple method is provided for the selection of the secondary surface of the exchanger based on VPI. Surfaces that produce smaller volumes will generate larger VPI. Therefore, surfaces with the largest VPI within the operational Reynolds ratio can be selected by the designer and then the given exchanger can be designed through coding in MATLAB. Finally, the overall heat transfer coefficient and the overall surface of the exchanger are obtained.

Performance Description of Liquefaction Cycle of LNG

The liquefaction of LNG or pre-cooled propane and a mixture of triple refrigerants (C3MR) (Fig.1) includes an initial pre-cooled stage that is done in the presence of almost pure propane (421). In this stage, the NG feed initially enters into two heat exchangers (E-104 and E-105), and leaves them at the temperature of 272°K. Then, it enters into the separator (V-103). After the separation of liquids and gases, its gaseous flow (V) enters into the heat exchanger (LNG-101). In the cooling stage, the gas temperature significantly decreases and reaches to 137.7°K with a mixture of methane, ethane, and propane (11) refrigerants. Natural gas is liquefied after leaving this exchanger. The parameters required before the initiation of simulation are presented in Table 1.

Table 1. Specifications of Feed in Iran LNG Project

	Vaper Phase	Liquid Phase
Vaper phase fraction	1	-
Temperature	318 °K	-
Pressure	9150 kPa	-
Mass density	69/03 kg/m^3	-

Feed	Mass Velocity(kg/s)
CO_2	0/02084
N_2	14/31458
CH_4	145/42181
C_2H_6	14/77288
C_3H_8	0/79788
i C_4H_{10}	0/01407
n C_4H_{10}	0/00701
Total	175/34929

Table 2. Physical and process specifications of hot fluid (V) to PFHE in liquefaction cycle

	Vaper Phase	Liquid Phase
Vaper phase fraction	1	-
Temperature	282.28 °K	-
Pressure	7809 kPa	-
Mass density	82/58 kg/m^3	-

Feed	Mass Velocity(kg/s)
CO_2	0/02084
N_2	14/31458
CH_4	145/42181
C_2H_6	14/77288
C_3H_8	0/79788
i C_4H_{10}	0/01407
n C_4H_{10}	0/00701
Total	175/34929

Table 3. Physical and process specifications of cold fluid (11) to PFHE in liquefaction cycle

	Vaper Phase	Liquid Phase
Vaper phase fraction	0.2764	0.7236
Temperature	132.7 °K	-
Pressure	214 kPa	-
Mass density	19 kg/m^3	-

Feed	Mass Velocity(kg/s)
CH_4	1225/47
C_2H_6	626/44
C_3H_8	1837/36
Total	3689/33

In this simulation, the selection of the equation of state is very important. The Peng-Robinson equation of state is commonly used for the mixture of light hydrocarbons such as natural gas. Since our simulation feed is a natural gas that consists of methane, ethane, propane and butane (three light hydrocarbons), the Peng-Robinson Equation was selected.

In general, this liquefaction process consists of three heat exchangers, one compact heat exchanger and six compressors. This process also accounts for the majority of investment costs. In this article, the compact heat exchanger (LNG-101) and reduction of investment costs through its usage are considered.

This simulation was done using Aspen HYSYS to extract the process and physical specifications of the compact heat exchanger inflows (11 and V flows) and to calculate the surface of LNG-101. This information was used for designing the exchanger.

Modified Volume Performance Index (VPI)

To start the design, the selection of surfaces, which provide the smallest units of weight and volume with high performance, is the first choice in design. If one of the limitations was violated in the first design, frequent stages in the selection of different surfaces with lower functional features should be taken. A number of indices have been provided by researchers to select the best secondary surface (fin) within the operational Reynolds ratio. This index is indeed the modified version of the index $\left(\mathrm{VPI} = \frac{\left(\frac{St^3}{f}\right)^{\frac{1}{2}}}{d_h}\right)$ previously provided by Polley et al. [8]. In the original index, the effects of inferences from other thermal resistances on the heat transfer coefficient inside the tubes were not well taken into consideration; whereas, the effect of fouling coefficient and other thermal resistances were considered in the modified version of the index [6]: $\mathrm{VPI} = \left(\frac{1}{1 + R_{opp.}h_t}\right)^{1/5} . \sqrt{\frac{St^3}{f}}$

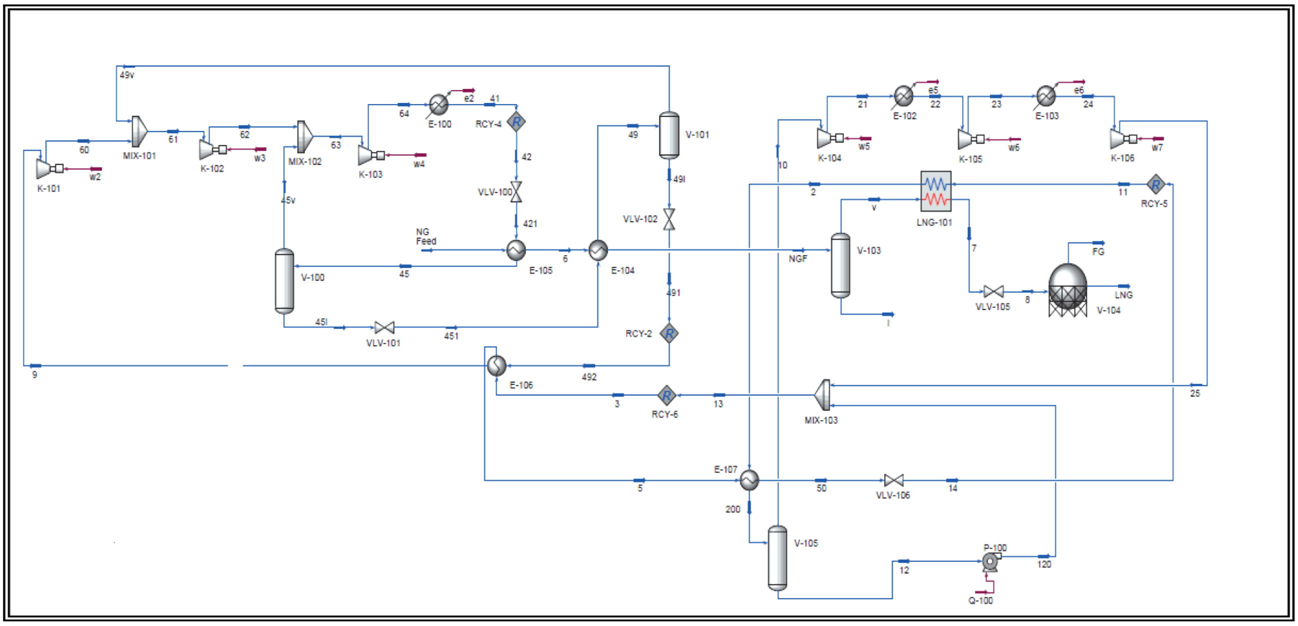

Fig 1. Liquefaction cycle or pre-cooled propane, and a mixture of refrigerants per unit of natural gas

The Stanton number and fraction factor are functions of Reynolds; therefore, the VPI is also a function of Reynolds number. It has been shown that the higher rate of this index implies greater compaction of the exchanger and selection of a surface with higher performance

[6]. We can draw the VPI diagram can be plotted for different surfaces based on Reynolds to be capable of selecting the best surface quickly. The VPIs of different surfaces of various types are drawn in fig.2 and 3. These surfaces have been based on the give data by Keyes and London [7]. In this demonstration the surfaces with the best performance are shown for every range of Reynolds. In this way, the smallest volume of exchanger is obtained by making sure of having access to complete pressure drop for the flow and the selection of the most effective surface. For the first case, a great need for the development of a design method that allows maximum use of pressure drop is felt; whereas, the second case allows the selection of surfaces with the best performance for a certain Reynolds number.

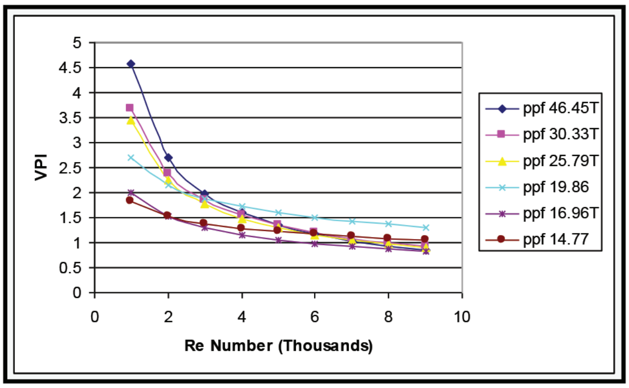

Fig 2. VPI based on Reynolds number for Plain Fin [5]

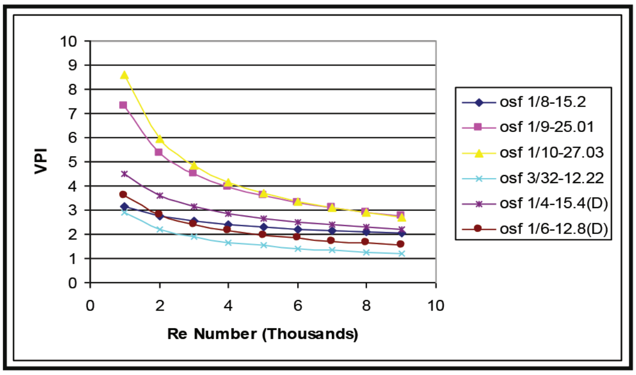

Fig 3. VPI based on Reynolds number for Offset Strip Fin [5]

Thermo-Hydraulic Model

The design model, which is based on the maximum use of pressure drop and development of thermo-hydraulic model, is used to design the compact plate-fin exchangers [12]. This model of pressure drop correlates a certain flow to the overall volume of the exchanger and the heat transfer coefficient of the same side of it. The performance of heat transfer for different compact surfaces is correlated by Reynolds number as follows:

$$j = a\,Re^{-b} \tag{1}$$

Where, J is known as Colburn factor and defined as follows:

$$j = St.\,Pr^{\frac{2}{3}} \tag{2}$$

The Prandtl and Stanton numbers are defined as follows:

$$Pr = \frac{C_p \mu}{k} \tag{3}$$

$$St = \frac{hA_C}{mC_P} \tag{4}$$

For the plane heat exchanger, the Reynolds number is defined as a function of hydraulic diameter of the surface:

$$Re = \frac{md_h}{\mu A_C} \tag{5}$$

Equations 4 and 5 are combined and its solution for the heat transfer coefficient (h) is as follows:

$$h = K_h \left(\frac{1}{A_C}\right)^{1-b} \tag{6}$$

where A_c is the free surface and K_h is defined as follows:

$$K_h = \frac{am^{1-b}\mu^{b}C_P}{d_h^{b}\,Pr^{\frac{2}{3}}} \tag{7}$$

The Equation 6 presents the heat transfer coefficient as a function of physical properties, mass flow rate, and free surface of flow.

It can be used to obtain a relationship that correlates pressure drop to free surface of the flow and physical properties. The term that expresses pressure drop in the heat exchanger is as follows:

$$\Delta P = \frac{f}{2\rho} \cdot \frac{A}{A_C} \cdot \frac{m^2}{A_{C_2}} \tag{8}$$

For the majority of secondary surfaces, the values of friction factor (f) can be correlated with the Reynolds number ranging from 500 to 10,000 as follows:

$$f = x\,Re^{-y} \tag{9}$$

where x and y are constant values. The overall heat transfer surface area of one side of the exchange is defined as a function of overall volume of the exchanger through following equation:

$$\hat{A} = \alpha V_T \tag{10}$$

where α is called "geometric parameter", which is indeed the ratio of the overall surface area of one side of the exchanger to overall volume of it. The combination of Equations 5 and 8-10 is obtained as follows:

$$\Delta P = K_P V_T \left(\frac{1}{A_C}\right)^{3-y} \tag{11}$$

Where,

$$K_P = \frac{x m^{2-y} \mu^y \alpha}{2\rho d_h^y} \tag{12}$$

By taking AC from Equation 2 and placing it in Equation 7, we have:

$$\Delta P = \frac{K_P}{K_h^z} V_T h^z \tag{13}$$

Where,

$$z = \frac{3-y}{1-b} \tag{14}$$

Equation 13 represents a thermo-hydraulic model that correlates flow pressure drop to the overall volume of the exchanger and heat transfer coefficient of the flow.

Equations Required in Volume Design

The main equation for heat transfer design is as follows:

$$Q = UAF\Delta T_{LM} \tag{15}$$

After combination of it with the overall heat transfer coefficient, following equation is obtained:

$$A_1 = \frac{Q}{F\Delta T_{LM}} \left[\frac{1}{\eta_1} \left(\frac{1}{h_1} + R_1\right) + \frac{1}{\eta_2} \left(\frac{A_1}{A_2} \cdot \frac{1}{h_2} + R_2\right) \right] \tag{16}$$

where A_2 and A_1 represent the overall surface of heat transfer at the Sides 1 and 2, receptively.

The overall volume of the exchanger and overall heat transfer surface of one side of the exchanger are correlated according to Equation 10. After the placement of A in the Sides 1 and 2 of the Equation 10, we have:

$$V_T = \frac{Q}{F\Delta T_{LM}} \left[\frac{1}{\eta_1 \alpha_1} \left(\frac{1}{h_1} + R_1\right) + \frac{1}{\eta_2 \alpha_2} \left(\frac{1}{h_2} + R_2\right) \right] \tag{17}$$

Equation 17 presents the overall volume of the exchanger as a function of heat duty, surface geometry, and heat transfer coefficients.

The heat efficiency of the surface of both sides of the exchanger is defined as:

$$\eta = 1 + f_s \left\{ \frac{\tanh\left[\left(\frac{2h}{k\tau}\right)^{\frac{1}{2}} \left(\frac{\delta}{2}\right) \right]}{\left(\frac{2h}{k\tau}\right)^{\frac{1}{2}} \left(\frac{\delta}{2}\right)} - 1 \right\} \tag{18}$$

The cross flow plate-fin heat exchangers function in a way that the flow pathways are independent in the cross flow; in addition, the maximum pressure drop becomes possible in both sides of the exchanger. The solution of the pressure drop equation for each flow determines the overall length and width of the exchanger along the flow. For a certain volume and front surface, access to the desired number of pathways or unique suitable dimensions is possible via manipulation of the width and height of the exchanger.

Rapid Design Algorithm (RDA)

Rapid design algorithm of heat exchangers is indeed the simplest method of direct design of heat exchangers. Given that the calculation of heat transfer coefficient and pressure drop are important elements of design, an allowable pressure drop is usually defined in exchanger design. If the pressure drop exceeds the normal level, a vibration will be made by the system; whereas, if this pressure drop is far lower than the threshold allowed by the design, heat transfer coefficient will be reduced. Thus, we have:

$$\Delta P_{\mathrm{Hot\,Stream}} < \Delta P_{\mathrm{Hot\,stream/allowable}} \tag{19}$$

$$\Delta P_{\mathrm{Cold\,Stream}} < \Delta P_{\mathrm{Cold\,stream/allowable}} \tag{20}$$

Taking the allowable pressure drop into consideration as the system drop seems dangerous and illogical. This technique is a procedure that generates an acceptable result in the optimization of the exchanger.

The general design technique is as follows: For hot stream (HS), we have:

$$h_{HS} = f(V_{HS}) \tag{21}$$

$$\Delta P_{HS} = f'(V_{HS}) \tag{22}$$

We remove V_{HS} from the equations:

$$\Delta P_{HS} = F(h_{HS}) \tag{23}$$

The same is true for the cold stream:

$$h_{CS} = f(V_{CS}) \tag{24}$$

$$\Delta P_{CS} = f'(h_{CS}) \tag{25}$$

After the removal V_{CS}, we have:

$$\Delta P_{CS} = F'(h_{CS}) \tag{26}$$

According to the owing equations:

$$\begin{cases} Q = UAF_T\Delta T_{LM} \\ \dfrac{1}{U} = \dfrac{1}{h_{HS}} + \dfrac{1}{h_{CS}} + R_D \\ \Delta P_{HS} = F(h_{HS}) \\ \Delta P_{CS} = F'(h_{CS}) \end{cases} \tag{27}$$

A nonlinear A-based equation is obtained, which is solved through Newton-Raphson method.

Using the briefly described thermo-hydraulic model and RDA method, an algorithm was developed for designing plate-fin heat exchanger in LNG liquefaction cycle.

Rapid Design Algorithm of Plate Heat Exchanger

According to RDA and the thermo-hydraulic model, the design algorithm of cross flow plate-fin heat exchanger is as follows:

1. The physical properties of the cold and hot fluids include thermal capacity of thermal conductivity (C_p)(K), density (P), viscosity (μ), and fouling resistance (R) are considered as inputs.
2. Operational parameters including input and output temperature of cold and hot fluids, mass flow rate (m°), and pressure drop (ΔP) are considered as inputs.
3. Type of the secondary surface for the cold and hot fluids, thickness of separating plate (a), and thermal conductivity of the separating plate (K) are considered as inputs.
4. Values of α_C, α_h for the cold and hot flows are computed via $\alpha_h = \frac{b_h\beta_h}{b_h + b_c + 2a}$ and $\alpha_C = \frac{b_c\beta_C}{b_h + b_C + 2a}$; where, b and β are surface-related geometric parameters that are determined with the selection of the surface type; and α is the ratio of overall transfer surface of one side of the exchanger to the overall volume of the exchanger, extracted from Keyes-London's book.
5. K_h and K_p values are computed according to the Formulas 7 and 12 for the hot and cold sides.
6. The h values for the hot and cold sides are

calculated via Formula 13 and based on V_T (overall volume of the exchanger).

7. The η (thermal efficiency of surface) values for the hot and cold sides are computed using Formula 18, based on h which is a function of V_T.

8. Values of $\alpha_C, \alpha_h, \eta_C, \eta_h, h_C, h_H$ are placed in Equation 17. The obtained equation is a nonlinear equation based on V_T, which is solved using Newton-Raphson method. In this way, V_T (i.e. the overall volume of the exchanger) is obtained.

9. $R_C, R_h, h_C, h_h, \eta_C, \eta_h, V_T$, A_C, A_h are produced as the outputs of the computer program.

A Case Study Designing Plate Heat Exchanger

The introduced algorithm was used for the design of compact plate-fin heat exchanger in the liquefaction cycle of Iran LNG project. Simulation-extracted information of inflows was used as input of the algorithm programing. Moreover, results related to the cold and hot sides and the overall heat transfer coefficient obtained from the simulated exchanger were compared with the results obtained from rapid algorithm program. The post-design results of the exchanger were acceptable.

Information related to the operational conditions and physical properties of the problem, and data related to the surfaces used in the exchanger are summarized in Table 4.

In this design, the maximum allowable pressure drop has been considered for the

Table 4. Process information and physical properties for design of the simulated cross flow exchanger

	Cold stream(1)	Hot stream(2)
Process Information		
Mass Flow Rate $(\frac{kg}{s})$	3688.888	175.361
Allowable Pressure Drop (Pa)	15000	140000
Inlet Temp. $(^{\circ}K)$	132.7	282.277
Outlet Temp. $(^{\circ}K)$	135.3	137.7
Physical Properties Information		
Density (kg/m^3)	19	85.58
Mass Heat Capacity $(\frac{J}{kg^{\circ}K})$	2120	2924
Thermal Conductivity $(\frac{W}{m^{\circ}K})$	0.134752	0.04066
Viscosity (kg/m.s)	0.0278698	0.001383
Surface Information		
Type of Surface	$ofs\frac{1}{10}-27-03$	$ofs\frac{1}{10}-27-03$
Heat Transfer Coefficient (a)	0.5231	0.5231
Heat Transfer Exponent (b)	0.5042	0.5042
Friction Factor Coefficient (x)	1.5369	1.5369
Friction Factor Exponent (y)	0.4648	0.4648
Thermal Conductivity of the Fin $(\frac{W}{m^{\circ}K})$	220	220
Plate Thickness (m)	0.0003	0.0003

Table 5. Design of the simulated cross flow heat exchange (comparison of results)

	Simulation	Program
Re (Cold=1)	-	2469
Re (Hot=2)	-	102090
Efficiency(Cold=1)	-	0.56
Efficiency(Hot=2)	-	0.53
Total Surface(Cold) (m^2)	3001	575
Total Surface(Hot) (m^2)	1933	575
Heat Transfer Coefficient(Hot) $(\frac{W}{m^2.^\circ K})$	-	3980
Heat Transfer Coefficient(Cold) $(\frac{W}{m^2.^\circ K})$	-	4545
Total Volume (m^3)	-	0.46
Overall Heat Transfer Coefficient* Surface (W/hr-°C)	2.3×10^6	4.84×10^5

cold and hot sides. This maximum pressure drop maximizes the rate and thus increases Reynolds. According to the Nusselt Equation, an increase in Reynolds produces the maximum heat transfer coefficient for the hot and cold surfaces; therefore, the overall coefficient of heat transfer is maximized. According to $Q=UAFAT_{LM}$, despite the maximum rate of overall heat transfer coefficient and fixed temperature difference between the cold and hot sides, the minimum surface area is obtained. Surfaces obtained via programing with secondary surface of $\text{ofs}\frac{1}{10}-27-03$ for both cold and hot sides are 575m^2, which decreased by 2.5 and 3.3 times as compared to the surfaces areas of 3001m^2 and 1933m^2 for the cold and hot sides in the simulation, respectively. This surface area reduction was highly desirable as it significantly decreased investment costs of developing such types of exchangers.

Results Using VPI in Design of Plate Heat Exchanger

Using the modified VPI and drawn diagrams, surfaces with maximum VPI within the range of operational Reynolds were selected. The given exchanger was designed using the computer program, and the overall volume and surface area of it were obtained. A comparison was provided in Tables 5 and 6 between the surface obtained from designing cross flow LNG exchanger using VPI and the surface obtained from the simulated exchanger.

Between different secondary surfaces (Table 5), ppf46.45T for the hot side and $\text{ofs}\frac{1}{10}-27-03$ for the cold side presented the minimum surface areas (422m^2 for the hot side and 556m^2 for the cold side). The overall heat transfer coefficient 785 (W/m^{2}K) increased by 1.8 times. Reduction by 1.1 and 5.1 times was observed in the hot side as compared to the hot side (1933m^2) and the cold side (3001m^2) in the simulated exchanger, respectively. After comparison of the obtained surfaces in Tables 5 and 6, $\text{ofs}\frac{1}{10}-27-03$ was selected for the hot and cold sides. This is because it presented the minimum surface area for the given exchanger. For example, the overall surface area of the heat transfer obtained for $\text{lpf}\frac{1}{2}-6.06$ and $\text{ofs}\frac{1}{10}-27-03$, ppf 46.45T under a certain pressure drop, is presented in figure 4. Also, figures 5 and 6 compared the heat transfer levels obtained for the cold and hot sides of these three different secondary surfaces with the heat transfer levels of the cold and hot surfaces in the simulated exchanger.

In figures 7 and 8, the overall volume and heat transfer coefficient of the simulated and designed exchangers were compared. According to the figures, the overall volume of the designed exchanger decreased by 5.4 times; in addition, the overall heat transfer coefficient increased by 2 times.

Conclusion

The design procedure developed in this article shows that this method is well capable

Table 6. Comparison of Novel Designed Heat Exchanger with the Simulated Exchanger

No. of HS	No. of CS	Re (H)	Re (C)	V(m^3)	Hot Surface	Cold Surface	Heat transfer .surfac coefficiente	Heat transfer coefficient
					1933	3001	2.3×10^6	425
ppf46.45T	$ofs\frac{1}{10}-27.03$	107160	2629	0.61	1620	587	1.2723×10^6	785
ppf11.11	$lpf\frac{3}{8}-6.06$	366140	9524	1.041	605	450	6.2656×10^5	1034
ppf46.45T	ppf30.33T	109260	3512	0.66	1553	830	8.8344×10^5	568
ppf46.45T	$lpf\frac{1}{4}-11.11$	79040	7363	1.014	3138	356	3.825×10^6	1218
$ofs\frac{1}{10}-27.03$	$lpf\frac{3}{8}-11.1$	80255	7793	08.6	1058	379	1.1948×10^6	1128
ppf11.11	$lpf\frac{3}{8}-11.1$	421360	6729	0.81	422	556	3.8310×10^5	906
ppf46.45T	$lpf\frac{3}{8}-6.06$	65549	10473	1.5	4711	346	5.8723×10^6	1246
ppf46.45T	$wpf11.5-\frac{3}{8}w$	69567	6521	1.35	4140	461	3.9966×10^6	965
ppf30.33T	$wpf11.5-\frac{3}{8}w$	148160	6353	1.32	2366	493	2.1649×10^6	914
ppf25.79T	ppf30.33T	203480	3272	08.2	981	969	4.8956×10^5	498

Table 7. Comparison of Novel Designed Heat Exchanger with Simulated Heat Exchanger (Equal Surfaces)

No. of HS	No. of CS	Re (H)	Re (C)	V(m^3)	Hot Surface	Cold Surface	Heat transfer .surfac coefficiente	Heat transfer coefficient
-	-	-	-	6.04	1933	3001	23.10^6	425
$ofs\frac{1}{10}-27-03$	$ofs\frac{1}{10}-27-03$	102090	2649	0.46	575	575	484150	842
ppf46.45T	**ppf46.45T**	123040	1732	0.54	1201	1201	484003	403
ppf30.33T	**ppf30.33T**	224480	3301	0.7	951	951	483108	508
ppf25.79T	**ppf25.79T**	198290	3144	0.75	1039	1039	483135	465
$lpf\frac{1}{2}-6.06$	$lpf\frac{1}{2}-6.06$	294120	9933	1.12	473	473	482933	1021
$wpf11.5-\frac{3}{8}w$	$wpf11.5-\frac{3}{8}w$	201450	5662	1.16	664	664	483392	728

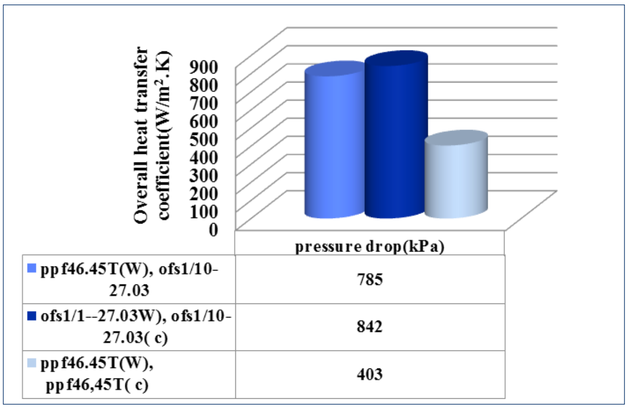

Fig 4. Comparison of the overall surface of heat transfer with different secondary surfaces under a certain pressure drop

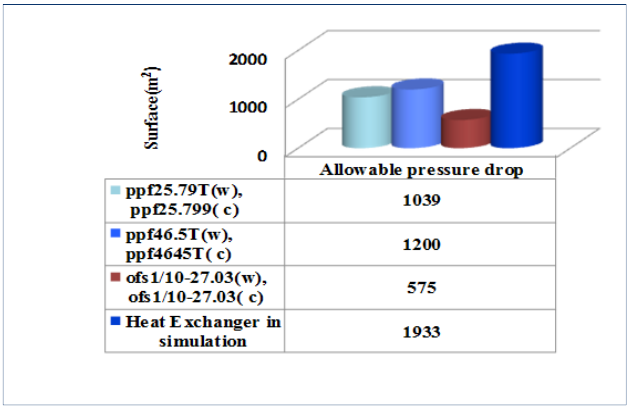

Fig 5. Comparison of heat transfer surface of the cold side of the simulated exchanger with the surface obtained after the optimal design

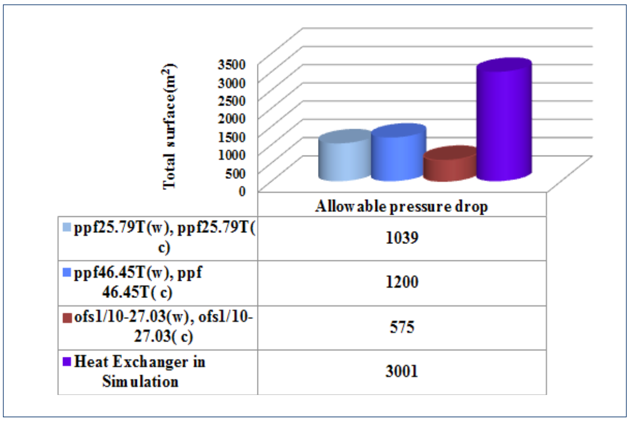

Fig 6. Comparison of the heat transfer surface of the hot side of the simulated exchanger with the surface obtained after the optimal design

of developing an optimal design of plate fin heat exchanger in terms of the surface area, volume, and overall heat transfer coefficient in Iran LNG project. In design of this exchanger, predetermination of the specification of surface involved in thermal process in both sides of the exchanger is needed. The rational objective of the design is an exchanger with the minimum

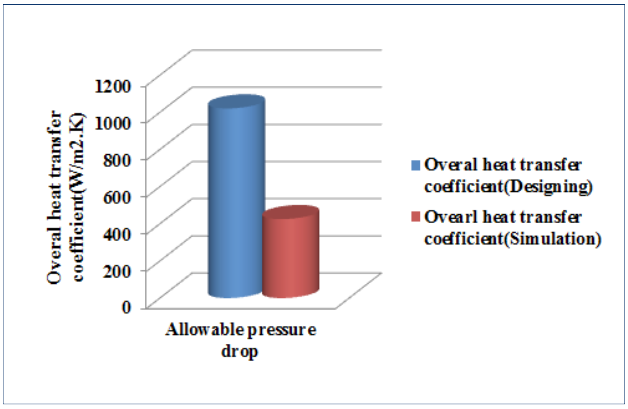

Fig 7. Comparison of volume of the simulated exchanger with that of the designed exchanger

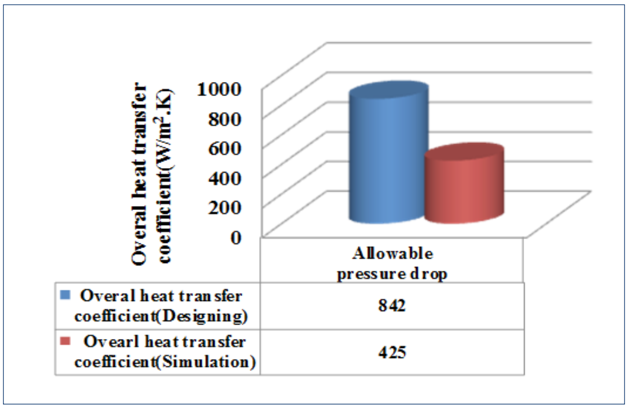

Fig 8. Comparison of the overall heat transfer coefficient of the simulated exchangerwith that of the designed exchanger

surface area within the block dimensions. This goal is achieved by ensuring about having full access to allowable pressure drop, and selecting a heat transfer surface with high efficiency. A correlation can be made between simultaneous design and selection of surface using VPI curves.

The provided design algorithm has been used for the case of Iran LNG project. Results obtained from designing the plate heat exchanger with the computer program show a good consistency with the results obtained from the simulated exchanger in the LNG cycle. Moreover, those fins were selected that provided surfaces of several times smaller than those of the simulated exchanger, using performance index. The cold and hot surfaces of the designed exchanger were 5.2 and 3.3 times smaller than those of the simulated exchanger; in addition, its overall heat transfer coefficient increased by 2 times. Given this significant reduction in surface area, a reduction will be achieved in investment costs in LNG process.

Symbols

A: Overall heat transfer surface area (m^2)
A_c: Free surface of flow (m^2)
a: Correlation coefficient of heat transfer
b: Correlation power of heat transfer
C_p: Thermal capacity of fluid $(\frac{J}{kg.^\circ K})$
d_h: Hydraulic diameter (m)
f: Friction coefficient of fluid in tube, friction factor
f_s: Secondary surface to overall heat transfer surface ratio
h: Heat transfer coefficient $(\frac{W}{m^2.^\circ K})$
J: Colburn heat factor
K_h: Dimensional constant
K_p: Dimensional constant
K: Thermal conductivity $(\frac{W}{m^2.^\circ K})$
M: Mass flow rate (kg/s)
Pr: Prandtl number (-)
ΔP: Pressure drop (kPa)
Q: Thermal load (J)
R: Fouling resistance $(\frac{m^2.^\circ K}{W})$
St: Stanton number (-)
ΔT_{LM} : Logarithmic mean temperature difference $(^\circ K)$
ΔT: The temperature difference between two ends of the flow $(^\circ K)$
Re: Reynolds number
U: Overall heat transfer coefficient $(\frac{W}{m^2.^\circ K})$
V: Exchanger volume (m^3)
VPI: Volume performance index
x: Correlation coefficient of friction factor
y: Correlation power of friction factor

Greek letters

α: Overall heat transfer surface of one side of the exchanger to overall volume of the exchanger $(\frac{m^2}{m^3})$

β: Overall heat transfer surface of one side of the exchanger to overall volume of the exchanger $(\frac{m^2}{m^3})$

δ: Distance between surfaces (m)
η: Fin efficiency
μ: Viscosity $(\frac{kg}{ms})$
ρ: Density $(\frac{kg}{m^3})$
σ: Ratio of free surface of flow to surface of flow in one side of the exchanger
σ: Fin thickness (m)

Footnotes

T: Total
C: Cold
H: Hot

References

1. Baek, S., Hwang, L., Jeong, C., "Novel design of LNG (liquefied natural gas liquefaction process", Energy convection and management, 52(8-9), 2807-2814, (2011).
2. Cesar, P., Julio,"A review on heat exchanger thermal hydraulic models for cryogenic applications", Cryogenics, 51(7), 366-379, (2011).
3. Fossas, Joan, S., «Modeling of multi stream LNG heat exchanger«, A thesis for degree of M.Sc., Norwegian University of science and technology, 8-10, (2011).
4. Fredheim AO, H.R, "Possibilities of cost reductions in base-load". EUROGAS96. Proceedings from the European applied research conference on natural gas, 1, (1996).
5. Jafari Nasr, M. R., Kalantari, A., "Choose surface &design of plate fin heat exchanger by RDA method" RIPI, 10, (2005).
6. Jafari Nasr, M. R., Zoghi, A. T., Khakdaman, H. R., "Performance evaluation of heat transfer enhancement in heat exchanger design«, RIPI, 43, (2002).
7. Kays, W. M., London, A. L., "Compact heat exchanger", McGraw Hill, (1984).
8. Nunez, M., Polley, G. T., Reyes, E., Munoz, A., »Surface selection and design of plate-fin heat exchangers«, Applied thermal engineering, 19- 917- 931, (1999).
9. Mohammadi, E., "Design and optimization of compact heat exchanger in LNG production unit" A Dissertation submitted to Chem. Eng. Dept. of Azad University, 87-89, (2013).
10. Saffari, H., »Modeling and optimization of C3MR LNG plant efficiency by change ff mixed refrigerants' components«, LNG research laboratory of mechanical engineering, Iran university of Science and Technology, 2-4, (2011).
11. Sanggyu, L., Ngyyen V. D., "Design and optimization of natural gas liquefaction and recovery process for offshore floating liquefied natural gas plant«, School of chemical engineering, Yeungnam University, Gyeongsan, 712-749, South Korea, (2012).
12. Walker, V., Wilkie, D., "The wider application of roughened surface as developed for advanced gas cooled reactors, Symp. on high pressure gas as a heat transport medium, IMechE, London, 26, (1967).
13. Wang, L., Sunden, M., "Optimal design of plate heat exchangers with and without pressure drop specifications", Applied thermal engineering, 23-295-311, (2003).
14. Wang, M., Zhang, J., "Optimal design and operation C3MR refrigeration system for natural gas liquefaction",Computer&Chem.Eng.,36,48-95,(2012).

Wettability Alteration in Near-Wellbore Regions of Gas Reservoirs to Mitigate Liquid Blockage Using Super Water- and Oil-Repellent ZnO/SiO_2 Nanofluid Treatment

- Pouriya Esmaeilzadeh, Mohammad Taghi Sadeghi*
  Chemical Engineering College, Iran University of Science and Technology (IUST), Narmak, Tehran 16765-163, Iran
  * (E-mail: sadeghi@iust.ac.ir)
- Alireza Bahramian
  Institute of Petroleum Engineering, University of Tehran, Iran

Received: Nov 29, 2016/ Revised: Dec 15, 2016 / Accepted: March 6, 2017

Abstract

In gas-condensate reservoirs as the bottom hole pressure drops below the hydrocarbon dew point of the reservoir fluid, liquids drop out from the gas phase and establish condensate banking near the wellbore, resulting in lower gas productivity. Changing the reservoir rock wettability from liquid-wetting to gas-wetting has outstanding potential in improving the productivity of gas wells. In this work, we report the highly water- and oil-repellent properties of carbonate reservoir rocks treated with a nanofluid based on synthesized ZnO/SiO_2 nanocomposites and fluoro-containing materials PTFE, TFE, and PFOS. Carbonate plates coated with the prepared nanofluid exhibits a high contact angle of 162° for brine (contact angle hysteresis=0° and roll-off angle <2°), together with 135° for liquid gas-condensate, supporting significant super-amphiphobicity with self-cleaning properties. Surface characterization of the rock using SEM, SP, and EDX analyses reveals that the rough morphology of ZnO/SiO_2 nanocomposites combined with low surface energy of fluorochemical provides the surface superamphiphobicity. Moreover, the efficiency of the nanofluid in wettability alteration of carbonate core from liquid-wetting to ultra gas-wetting under reservoir conditions was investigated by performing gas/liquid two-phase flow tests with single-phase liquid-injection into the gas-saturated core. The results indicate that the mobility of liquid for both gas/brine and gas/liquid-condensate systems increases significantly after wettability alteration.

Keywords: Gas-wetness; Wettability alteration; Nanofluid; ZnO/SiO_2 nanocomposites; Gas condensate reservoir; liquid-repellent.

1. Introduction

Gas-condensate reservoirs experience a significant loss in well productivity as reservoir pressure drops below the hydrocarbon dew point owing to condensate banking in the near-wellbore region and subsequent reduction in gas relative permeability [1,2]. Water blocking also decreases the relative permeability of gas [2,3] and increases the impact of liquid blockage on lowering the gas well deliverability. A major factor in liquid accumulation is the low mobility of liquids due to strong liquid-wetting of the reservoir rock. Through wettability alteration of the rock from liquid-wetting to gas-wetting, the mobility of liquid phase for a gas/liquid system increases dominantly, preventing the liquid accumulation in high saturation and resulting in elevated gas production rates. The principal requirement is the permanent alteration of wettability to gas-wetting. Li and Firoozabadi were the first who demonstrated both theoretically [4] and experimentally [5] that the approach of wettability alteration to gas-wetting is promisingly effective for improving the productivity in gas-liquid systems. In the theoretical work, they studied the relative permeability of gas and liquid phase using a phenomenological network model. Their results showed that substantial increase in gas well deliverability may be obtained when the wettability of porous media alters to gas-wetting and is the most effective approach. They moreover showed experimentally that the oil recovery and phase relative permeability in gas/oil system can be increased by wettability alteration of rock to preferential gas-wetting using fluoro-polymer chemicals. Later many other researchers investigated experimentally the efficiency of various fluorochemical polymers/surfactants on changing the wettability of different rock types to gas-wetting [6-14]. However, some of these chemicals fail to be utilized for field applications because they were not cost-effective, environmentally friendly or losing their effectiveness under reservoir conditions.

Nanofluids are a new class of solid/liquid mixtures engineered by dispersing nanometer-size particles or any nanostructures in conventional base liquids [15,16]. Over the past decade, the innovative concept of nanofluids, as a part of nanotechnology, has developed largely and used in various industrial and biological processes, such as drug delivery [17], surface coating [18], heat transfer [19], environmental remediation [20], etc. [16,21]. Nanofluids also revealed their potential applications in oil and gas industries through wettability alteration of reservoir rock [22], enhanced oil recovery (EOR) process [23,24], drilling technology [25], reservoir exploration, and natural gas transportation [26,27].

Recently, few papers have been published that report the impact of silica based nanofluids which are capable of altering the wettability of rock towards gas-wetting [28,29]. Although their studies were promising, they have not succeeded to change the wettability of reservoir rock to ultra gas-wetting state; hence, the issue is still an ongoing field of research.

In this paper, It is revealed report the super water- and oil-repellent properties of a novel ZnO/SiO_2-based nanofluid, applied to alter the wettability of a carbonate reservoir rock to ultra gas-wetting state. We verified the change of wettability by measuring contact angle and characterizing the rock surface using SEM images, EDX, and SP analyses. In continue, we investigate the practical efficiency of the superamphiphobic nanofluid in flow tests which represents better the reservoir conditions, by conducting a set of coreflooding experiments. Accordingly, the changes in the pressure drop and the liquid permeability in two-phase (gas/oil or gas/water) flow tests using single-phase liquid-injection into a gas-saturated core are measured before and after wettability alteration. It can be canclouded believe that the novel formulated ZnO/SiO_2 nanofluid can improve the productivity of the reservoirs and mitigate water and condensate blockage in gas wells.

2. Materials and methods

2.1. Preparation of super liquid-repellent ZnO/SiO$_2$ nanofluid

In order to prepare the nanofluid, as a first step ZnO/SiO$_2$ nanocomposites were synthesized via wet-chemical co-precipitation method through a hydrothermal process. Accordingly, 0.02 mol of Zinc nitrate hexahydrate (Zn(NO$_3$)$_2$.6H$_2$O, 98%, Merck) and 0.08 mol tetraethyl orthosilicate (TEOS, Si(OC$_2$H$_5$)$_4$, 95%, Merck) were dissolved in water/isopropyl alcohol (C$_3$H$_8$O, Merck) solution and stirred magnetically for 15 min. then 10 g of acetylacetone (C$_5$H$_8$O$_2$, >99%, Merck) dissolved in water/isopropyl alcohol solution and 20 g of oleic acid (C$_{18}$H$_{34}$O$_2$, Merck) were added gently to the basic solution and hydrolyzed by addition of sodium hydroxide (NaOH, Merck)/water-ethanol solution in a dropwise manner, under vigorous stirring to obtain a mixture with pH of 10-11. After refluxing for 1 h at 80-90 °C, the prepared mixture was quenched rapidly for 45 min and then dried hydrothermally in an oven for 72 h at 90 °C. Next, it was filtered, washed with water and alcohol solution and then dried. The resultant product was finally calcined in a furnace in 3 steps at 200-900 °C for 10 h. This procedure results in achieving fine hydrophobic ZnO/SiO$_2$ nanocomposites.

Super water- and oil-repellent ZnO/SiO$_2$ nanofluid was fabricated by using of the synthesized nanocomposites and fluorochemicals. For this purpose, ZnO/SiO$_2$ nanocomposites, polytetrafluoroethylene (PTFE, Sigma–Aldrich), 2,2,2-Trifluoroethanol (TFE, SDFCL Co., 99%), ethanol and a mixture containing Trichloro(1H,1H,2H,2H-perfluorooctyl) silane (PFOS, 97%, Sigma–Aldrich) were dissolved with mass ratio of 0.002:0.2:0.003:1:1 at room temperature. Using ultrasonic bath, the resultant solution was sonicated then for 30-40 min, followed by 1 h agitation on a magnetic stirrer at 50 °C [30,31].

2.2. Porous medium and fluids

A cylindrical carbonate reservoir core with a length of 6 cm, the diameter of 3.8 cm and porosity of 20.7% used in this work to perform core displacement tests. Static and dynamic contact angle measurements were also done on small circular rock plates that have been taken from a similar large slab of this carbonate reservoir core, respectively.

The plates and core being subjected to different tests, they were cleaned in Soxhlet extraction apparatus where they were flushed with toluene and methanol for 24 and 72 h, respectively. The pre-treatment process was followed by drying of rock in an oven at 80 °C for 24 h.

Distilled water and 2 wt% NaCl brine were used as the aqueous phase in order to investigate the hydrophobicity of rocks. Normal decane (C$_{10}$H$_{22}$, Merck, >99%) and a gas-condensate liquid sample from an Iranian gas condensate reservoir were used as the oil phase to study the oleophobicity of rocks. At 25 °C, the gas-condensate sample has a specific gravity of 0.78 and a viscosity of 1.28 cP. Air and nitrogen were also used as the gas phase in contact angle measurements and core displacement tests, respectively.

2.3. Treatment process

2.3.1. Contact angle tests

The clean and dry carbonate rock plates were totally submerged in fabricated nanofluid and aged in an oven at 80 °C for 48 h to let the nanocomposites and fluoro-containing materials sediment on the surface of plates and create a liquid-repellent layer on them. Next, the plates were removed from the nanofluid and dried in an oven at 80 °C and finally the dried plates were subjected to the contact angle measurement test.

2.3.2. Core displacement tests

In order to change the wettability of the core to gas-wetting state, it was put in a coreflooding apparatus, which is capable of resisting reservoir condition of temperature and pressure (Fig. 1). The apparatus will be described in detail later. The dry core was initially evacuated and then saturated with ZnO/SiO$_2$ nanofluid. For this purpose, three to four pore volumes (PV) of nanofluid was injected at a fixed flow rate of 2 cc/min. The nanofluid-saturated core was then aged in the nanofluid at 80 °C and 3000 psig for 48 h. After that, nearly 5 PVs of brine was injected to displace the nanofluid and wash the core, followed by evacuation for about 6 h. At last, the core was removed from its holder and dried in an oven at 80 °C.

Fig. 1. Experimental set up for core displacement tests and chemical treatment.

2.4. Characterization

Fourier transform infrared spectroscopy (FTIR) spectra were acquired on a Bruker tensor 27 spectrometer to evaluate the functional groups of the synthesized nanocomposites in the wavenumber range of 4000–400 cm^{-1}. The surface morphology of ZnO/SiO$_2$ nanocomposites and the carbonate core with and without wettability alteration were revealed by scanning electron microscope (SEM) (KYKY model EM3200). X-ray diffraction (XRD) was used to study the size and crystallinity of the nanocomposites using Bruker D8-Advance diffractometer with Cu Kα radiation (λ=1.54Å). The surface topography and roughness of the treated and untreated core sample were determined by stylus profilometer (SP) (Dektak XT from Bruker). Energy dispersive X-ray (EDX) (SiriusSD) was used to characterize the surface elemental composition of the carbonate core before and after treatment with nanofluid.

2.5. Contact angle measurement

To study the wettability of the core quantitatively and evaluate preliminary the superamphiphobicity of nanofluid, the gas–liquid–rock contact angle was measured using an in-house contact angle measurement device (Fig. 2a). The static contact angles of aqueous and oil phases as probe liquids in air medium and at room temperature were measured using sessile drop technique. In each measurement, a ~5 µl drop of liquid was released from an accurate syringe on the surface of the core sample. A CCD camera with the microscopic lens was used to visualize the process and taking side images of high-resolution magnified liquid droplet, under sufficient illumination of the light source. Each contact angle measurement was repeated for 3-5 times at different locations on the solid surface and the average value was reported. Dynamic contact angles were also measured by force tensiometer KSV Sigma 700, using the Wilhelmy method (Fig. 2b).

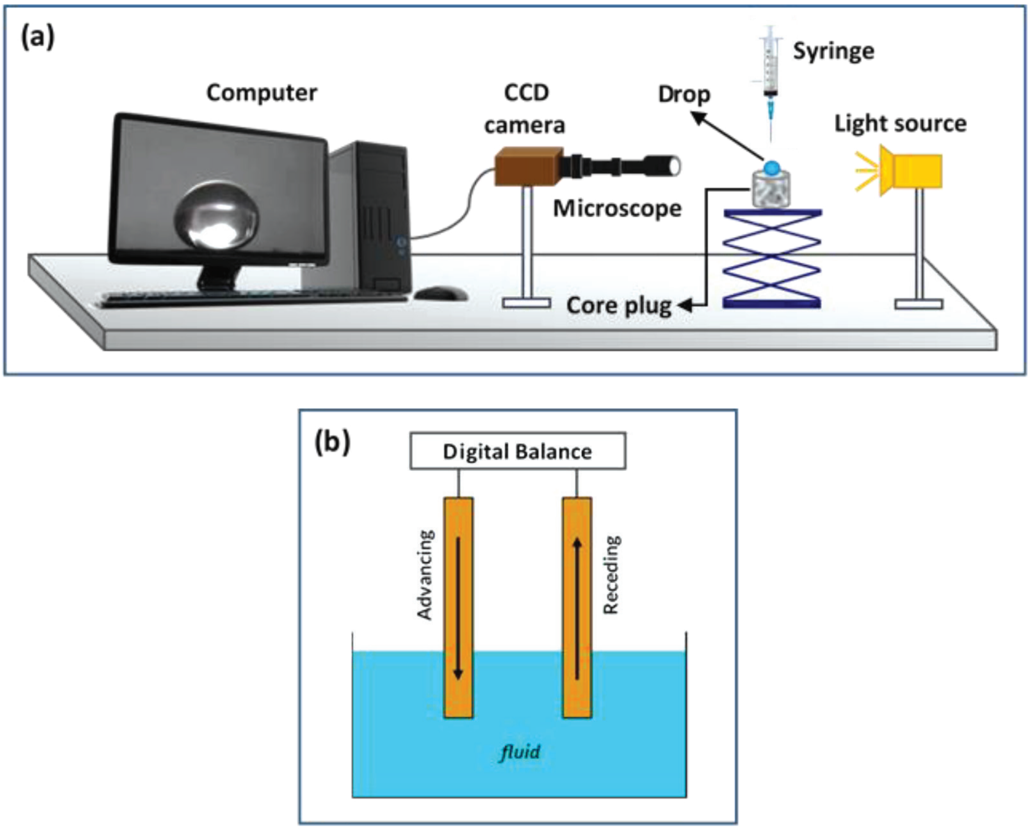

Fig. 2. Schematic for (a) static and (b) dynamic contact angle measurements.

2.6. Coreflooding apparatus and test procedure

Fluid flow tests were performed in core scale to investigate the efficiency of ZnO/SiO_2 nanofluid in wettability alteration to gas-wetting under reservoir temperature and pressure conditions. Fig. 3 illustrates a schematic of the coreflooding setup for the unsteady-state gas/liquid flow with gas displaced by liquid injection. The coreflooding apparatus contains high-pressure displacement pumps (Schlumberger DBR) with process control system for injecting the fluid at constant rate, a back pressure regulator for controlling the downstream core pressure, a differential pressure transducer (Rosemount 3051) for measuring the pressure drop across the core and a data acquisition system for collecting and storing the differential pressure information. The gas and liquid are discharged through the back pressure regulator and transmitted to a separator. The effluent Liquid is collected in a calibrated tube and the amount of it measured versus time. The outlet gas flow rate is also measured by a mass flow meter (Alicat M) in the range of 0-50 cm^3/s with the accuracy of about 0.8%. Other apparatuses such as liquid transfer vessels and a cylindrical core holder were placed inside a temperature-controlled oven. The core sample is fixed inside the core holder covered with a Viton rubber sleeve to confine the core. The core holder is placed horizontally to avoid gravity effect. For packing the core, an overburden pressure of 800-1000 psig above the inlet pressure is applied. The temperature of the system was maintained at 80 °C during all tests, which is high enough for most reservoir applications.

The goal of this study is to quantify the effectiveness of the nanofluid by measuring the effective and relative permeability of liquid flow in gas/oil or gas/water systems through liquid flooding of a gas-saturated core. Before wettability alteration, the core was evacuated first by a vacuum pump to get rid of air and

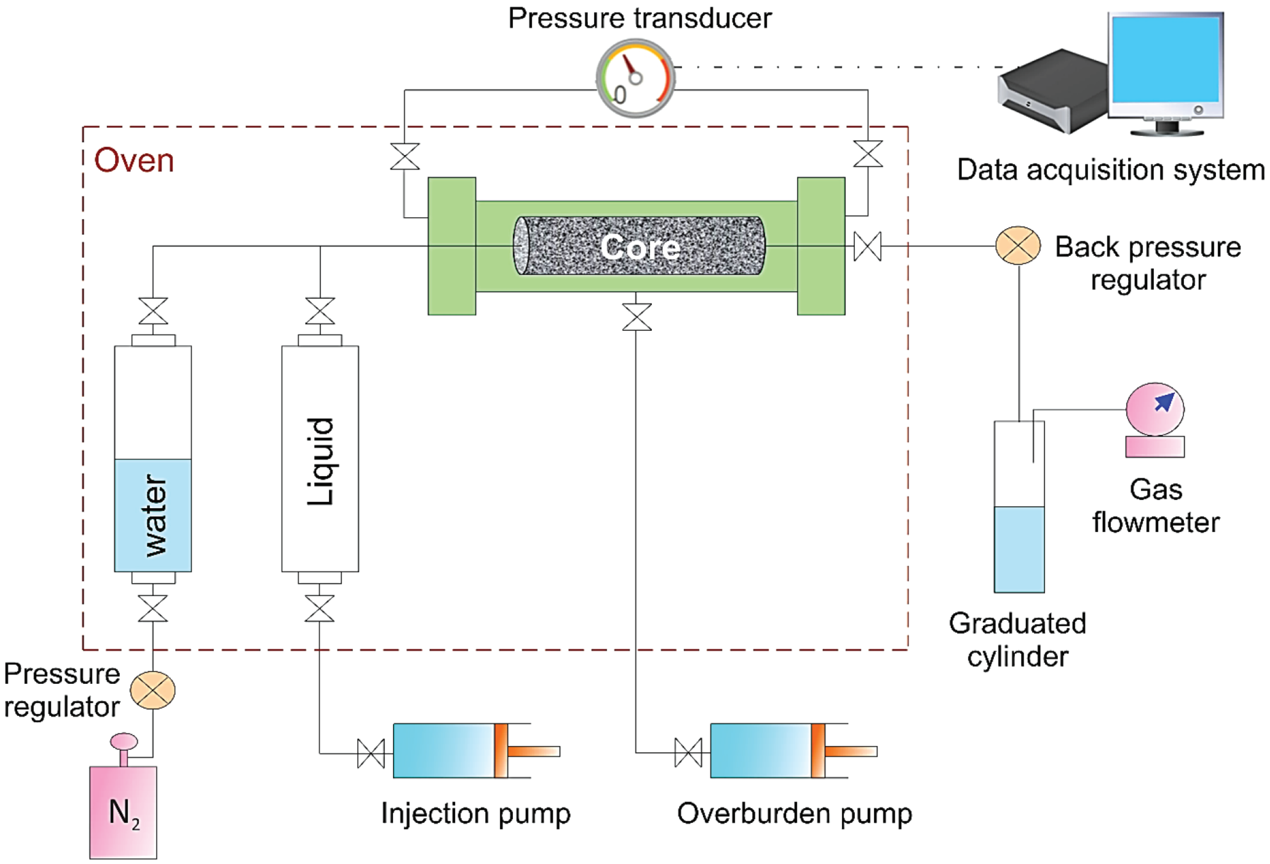

Fig. 3. Schematic of apparatus for core flooding experiments.

then it was saturated with the nitrogen which injected at a constant injection pressure by a gas-pressure regulator. Next, the displacement process of gas was started by injection of liquid (brine or gas-condensate) at a constant rate. The amount of produced gas and liquid versus time was recorded until surely no more gas recovered. Moreover, the transient pressure drop is recorded until steady-state is obtained. The effective and relative permeability of liquid flow were calculated subsequently, as explained in section 3.3. After that, the core was cleaned by a solvent and dried and evacuated before starting the next test.

After conducting the evaluation testing in the untreated core, the wettability alteration tests. Were performed for this purpose, the core was treated with nanofluid (as described earlier in section 2.3.2.) and the same experiments to those performed for untreated core were repeated to calculate the effective and relative permeability of the liquid flow after the wettability alteration.

3. Results and Discussion

3.1. Characterization of ZnO/SiO_2 nanocomposites

To confirm the formation of ZnO/SiO_2 through the synthesis process, the FTIR spectrum of the ZnO/SiO_2 nanocomposites is shown in Fig. 4. The bands positioned at 459, 577 and 615 cm^{-1} are attributed to Zn–O stretches [32,33]. The peaks at 868 cm^{-1} are related to the Si–O–Si asymmetric stretching vibrations while the peak at 979 cm^{-1} is for the Si–O–Si symmetric stretching [34]. The peak observed at 1457 cm^{-1} corresponds to Si–OH stretching vibration [34]. Furthermore, peak at 1628 cm^{-1} and a broad band at 3445 cm^{-1} are associated with O–H bending and O–H stretching vibrations of ZnO/SiO_2 [34]. Moreover, the appearance of the absorption band at 933 cm^{-1} is assigned to the Si–O–Zn stretching which confirms that SiO_2 indeed binds with ZnO [35jX].

The SEM image for the synthesized nanocomposites is presented in Fig. 5. It can be seen that the ZnO/SiO_2 nanostructures consist of the hybrid morphologies of nanospheres and nanoplates.

Fig. 6 illustrates the XRD patterns for the as-prepared ZnO/SiO_2 nanocomposites. The measured diffraction angles are reasonably compatible with the standard spectrum of willemite Zn_2SiO_4 (JCPDS card number 37–1485), indicating that the crystallographic structure of these nanocomposites is hexagonal. The diffraction peaks at $2\theta=31.48°, 33.95, 36.18°$ $65.58°$, $55.92°$, $48.89°$ and $66.68°$ can be attributed to the (100), (002), (101), (102), (110), (112) and (201) planes of ZnO, respectively [36,37]. The average crystallite size of ZnO/SiO_2 nanocomposites are calculated from the XRD analysis and Sherrer's equation,

$$t = \frac{0.9\lambda}{\beta \; Cos\Theta} \tag{1}$$

where is the full-width-at-half-maximum (fwhm) of the diffracted peak, is the diffraction angle, and is the wavelength of X-ray radiation (1.548 Å for Cu Kα). The estimated average crystallite size value for ZnO/SiO_2 nanocomposites is found to be 46 nm.

3.2. Contact angle determination and surface characterization

The wetting properties of carbonate core rock without and with wettability alteration to gas-wetting by nanofluid were identified through contact angle measurements of distilled water and 2 wt% NaCl brine as the aqueous phase, and n-decane and gas-condensate as the oil phases. The native carbonate plate was completely wetted by both water and oil liquid drops, which indicates the fact that the carbonate sample is strongly liquid-wet (i.e., the static contact angle of water and oil= 0°). However, the measured distilled water, brine, n-decane, and condensate contact angles of the rock plate were exceeded to 162°, 162°, 136°, and 135°, respectively, after treatment with nanofluid which demonstrates the superhydrophobic property of the treated surfaces. According to this results, ZnO/SiO_2 nanofluid has successfully increased the contact angle of water and oil drops to a much greater degree than the various chemicals reported in the previous studies [5-14,28,29]. Fig. 7 shows the brine and condensate contact angles on the surface of a rock plate, before and after wettability alteration.

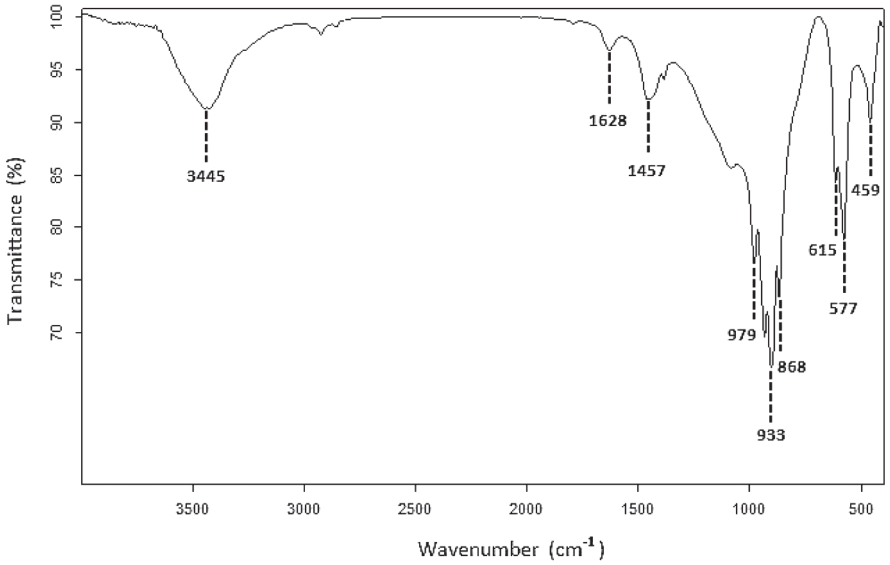

Fig. 4. FTIR spectra of ZnO/SiO$_2$ nanocomposite powders in 4000–400 cm $^{-1}$ region.

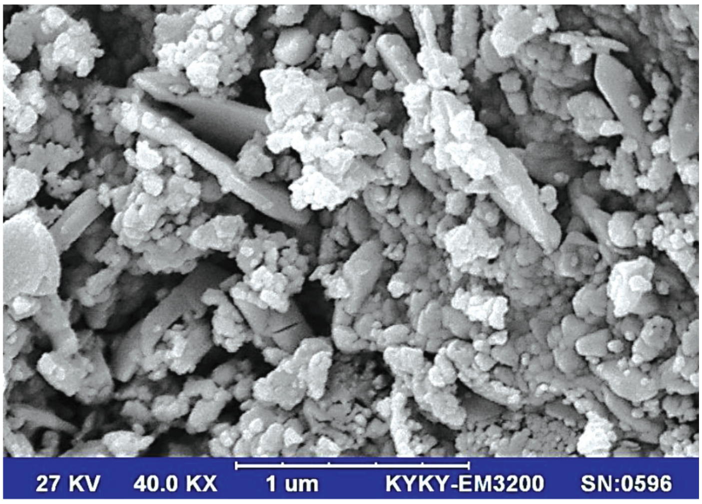

Fig. 5. SEM image of synthesized ZnO/SiO$_2$ nanocomposites.

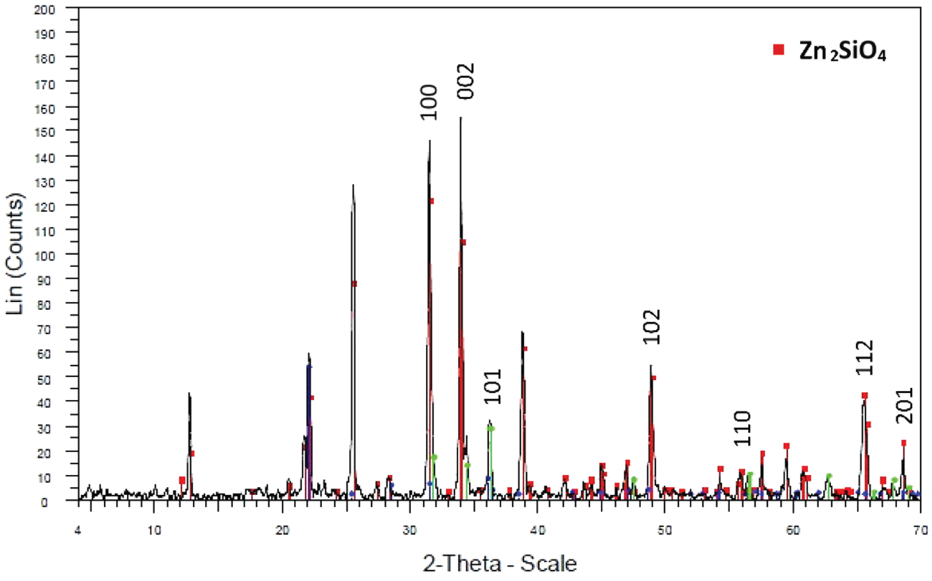

Fig. 6. XRD pattern of hexagonal ZnO/SiO$_2$ nanostructures.

Furthermore, it was observed that the aqueous phase droplets freely rolled-off on the treated core surface while there was no apparent tilt of the surface (2°), which made it difficult to control for measuring the static contact angle. Such a minimum sliding angle reveals that water has low adhesion to the rock surface and the core sample gained self-cleaning property [38,39]. Besides, it is known that for the self-cleaning property of a liquid-repellent surface, contact angle hysteresis of 10° is desired [40,41]. Contact angle hysteresis which is defined as the difference between the advancing and receding angles was measured using the Wilhelmy method. The value of contact angle hysteresis for the rock plate treated with nanofluid was measured quasi-null for the aqueous phase. Such an ultralow contact angle hysteresis, confirms that the rock surface benefits the drop-rolling ability and the self-cleaning property as well.

The improved hydrophobicity, oleophobicity, and self-cleaning properties of the treated rock are attributed to the combination of surface roughening by the ZnO/SiO_2 nanocomposites and lowering the surface energy by fluoro-containing coating [42-44]. The surface topography is generally known as the decisive factor in specifying the liquid-repellency of rough surfaces. Therefore, SP analysis and SEM images were employed to study the morphological features of the core surface structure. Fig. 8 illustrates the SP micrographs of both native rock plate and treated rock plate with nanofluid. Fig. 8a indicates that the pristine rock substrate generally offers a primary roughness with microscale structure. Regarding the corresponding contact angles of water and oil drops which are equal to 0°, the liquid-wetting nature of native rock plate can be ascribed to the several cavities existed throughout the roughness, which allows the liquids entering easily into them. After treatment, the deposition of nanofluid's contents provides the secondary roughness to repel the liquid penetration, referring the Cassie model [45]. In other words, the hierarchial rough structure on the surface, similar to the structure of a lotus leaf [44], can simply trap a large amount of microscopic air layer in the craters between the protrusions that reduces the contact area between the liquid and the surface. The air pocket makes a floating force against water and oil drops that leads to superamphiphobicity.

Besides the surface roughening by ZnO/SiO_2 nanocomposites, using the fluoro-containing materials as PTFE, TFE and PFOS solution enhanced the liquid-repellency of the core surface, especially the oleophobicity, owing to impressive reduction of surface free energy. TFE and PFOS have very low surface energy owing to their high content of $–CF_3$ and $–CF_2$ groups. $–CF_3$ terminated surfaces are known to possess the lowest surface free energy of ~6 mN m^{-1} followed by $–CF_2$ groups as the next lowest [46-48]. Teflon also has the low surface energy of 18.5 mN m^{-1} [48]. Hence, the deposition of fluorochemicals on the outermost layer of surface coating decreases the surface energy and the intrusion of liquids into cavities of the surface.

SEM investigations of the carbonate plate before and after wettability alteration to gas-wetting, distinctly confirm the formation of a layer containing fluorochemicals and ZnO/SiO_2 nanocomposites on the microstructure core surface, after treatment with nanofluid (Fig. 9). The average size of the sphere-like nanotextures was determined to be in the range of 34-60 nm in diameter.

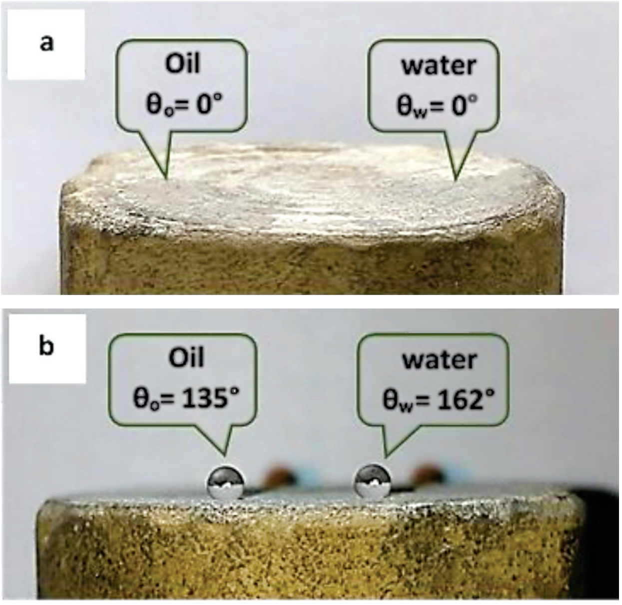

Fig. 7. Static Contact angle of brine and gas-condensate on the surface of carbonate rock plate (a) before and (b) after wettability alteration.

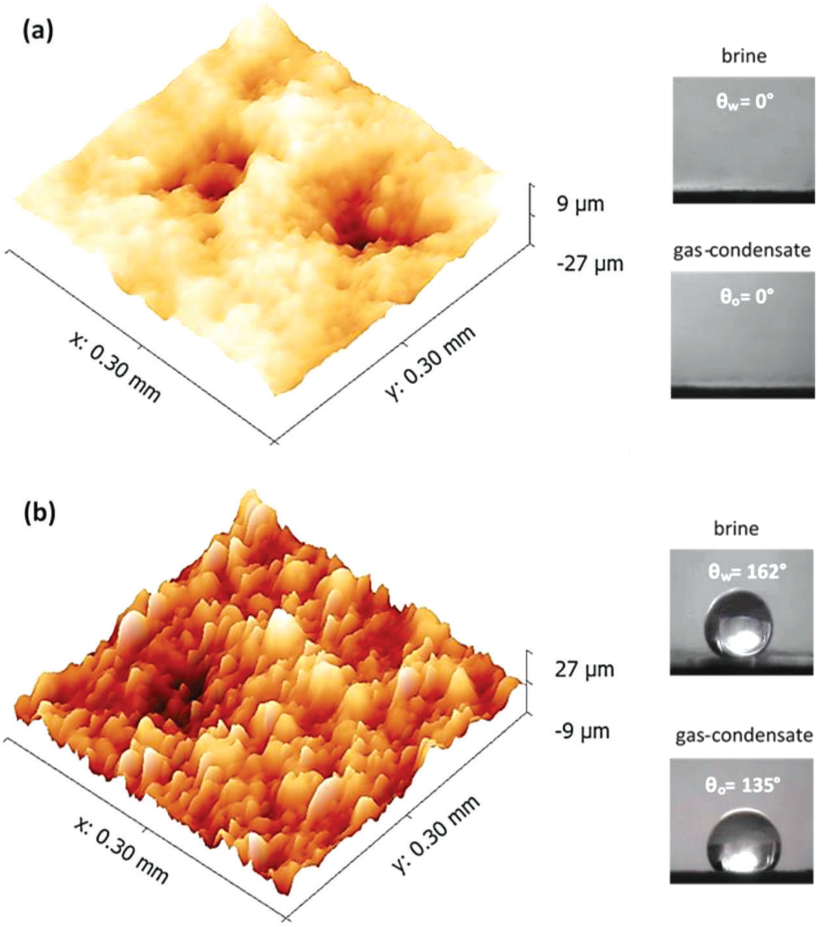

Fig. 8. 0.3 mm × 0.3 mm 3D SP topography images of the (a) untreated and (b) treated core substrate. Cross-view shapes of brine and gas-condensate droplets placed on the corresponding surfaces are shown in the insets.

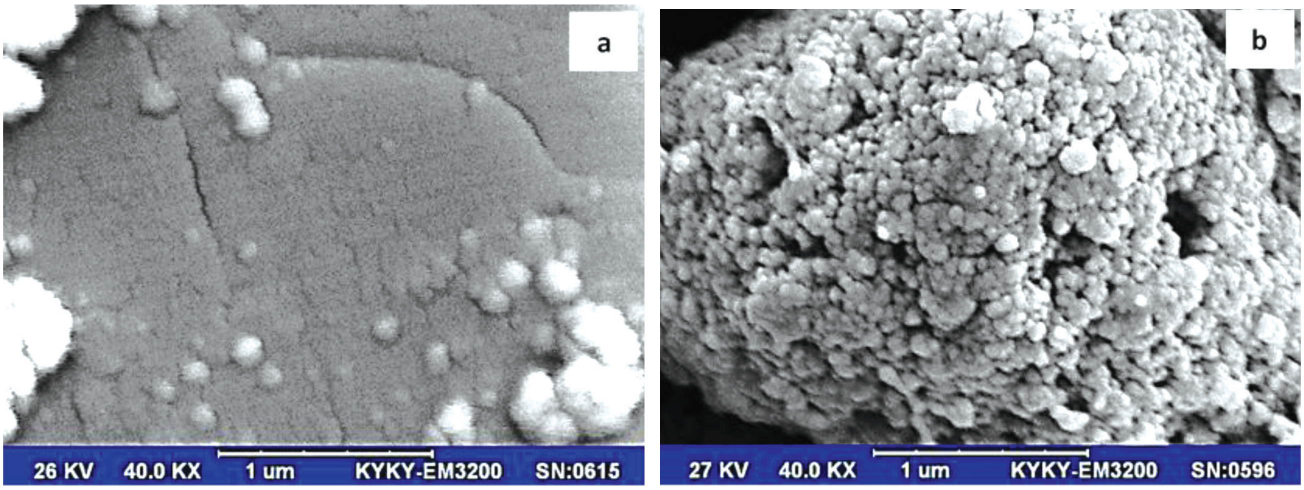

Fig. 9. SEM images of (a) untreated rock plate and (b) treated rock plate with ZnO/SiO_2 nanofluid.

3.3. Core displacement results

After a preliminary evaluation of the formulated nanofluid by contact angle measurements, fluid flow tests were used to investigate the effect of wettability alteration on water and condensate blocking in the carbonate core. The result of pressure drop across the core as a function of pore volumes injected of liquid is presented in Fig. 10. As seen from Fig. 10a for gas/water system, in both untreated and treated cores, the pressure drop increases initially until it reaches the maximum value. Afterward, the pressure drop decreases gradually and stabilized at a constant value of 15.0 psi for untread core and 6.5 psi for treated core at the steady-state. Hence, nanofluid treatment reduced the steady-state two-phase flow pressure drop about 56%. The same trend is also observed in gas/oil system (Fig. 10b), with the pressure drop plateaus at 17.7 psi for untread core and 7.8 psi for treated core. The treatment of carbonate core with nanofluid could also improve the steady-state pressure drop of this case about 56%. These results imply the pronounced capability of the nanofluid in altering the wettability from liquid-wetting (hydrophilic and oleophilic) to ultra gas wetting (superamphiphobic).

The single-phase liquid-injection in a core saturated with gas is a transient two-phase gas/liquid flow experiment in which the gas inside the core is displaced by the liquid. In late stage of liquid injection, when the residual gas is left in the core and the pressure drop reaches steady-state, we apply Darcy's low for calculating the effective permeability of liquid flow (K_{el}):

$$\Delta p = Q_l\left(\frac{\mu_l}{K_{el}}\right)\left(\frac{L}{A}\right) \tag{2}$$

where the pressure (Δp) is described as a function of the liquid volumetric flow rate (Q_l), with the parameters of core length (L), Liquid viscosity (μ_l), cross-sectional area (A), and the liquid effective permeability (K_{e1}) .

The liquid relative permeability (K_{rl}) is also calculated from the ratio of the liquid effective permeability to the liquid absolute permeability (K_l) which is received from single-phase liquid flow:

$$K_{rl} = \frac{K_{el}}{K_l} \tag{3}$$

The absolute permeability to water was measured to be 11 and 10.4 mD for untreated and treated core, respectively, which demonstrates the treatment of the core with nanofluid slightly reduces the absolute permeability due to plugging of small pore throats.

We quantify the nanofluid treatment effectiveness in liquid flow then by calculating the change in the liquid effective and relative permeability as follows:

$$\frac{\Delta K_{el}}{K_{el}} \equiv \frac{K_{el}\,(treated\ core) - K_{el}\,(untreated\ core)}{K_{el}\,(untreated\ core)} \tag{4}$$

$$\frac{\Delta K_{rl}}{K_{rw}} \equiv \frac{K_{rl}\,(treated\ core) - K_{rl}\,(untreated\ core)}{K_{rw}\,(untreated\ core)} \tag{5}$$

Table 1 gives the results of calculated effective and relative permeability of liquid flow in the pre-treated and post-treated cores. I it is obvious, the treatment of core with ZnO/SiO_2 nanofluid predominantly increases the brine and gas-condensate mobility under reservoir condition, according to increase in the effective and relative permeability of liquid. The results support the theory that the nanofluid successfully alters the wettability of carbonate core from strongly liquid-wetting to the ultra gas-wetting condition.

In order to investigate the penetration of the nanocomposites and fluorine species into the pores of carbonate core, since the coreflooding tests were accomplished, we have cut the core by a trimming machine from middle along the radius and analyzed the surface chemical composition by EDX spectra. As evidence from Fig. 11, the surface of native carbonate core is mainly composed of Ca, C and O elements. After treatment with nanofluid, the constituent materials of ZnO/SiO_2 nanofluid containing of Si and Zn elements as nanocomposite, and F element which comes from fluorochemicals were determined on the surface. The presence of these elements reflect the ability of nanocomposites accompanied with fluorochemicals to diffuse into the core and adsorb onto the surface.

Moreover, it is noteworthy to point out that the quality of the contact angle of brine and condensate drops on the treated rock plate in small slab scale and core scale (after injection of 5 PVs of water to displace the nanofluid) demonstrates the durability of nanofluid treatment at the reservoir conditions.

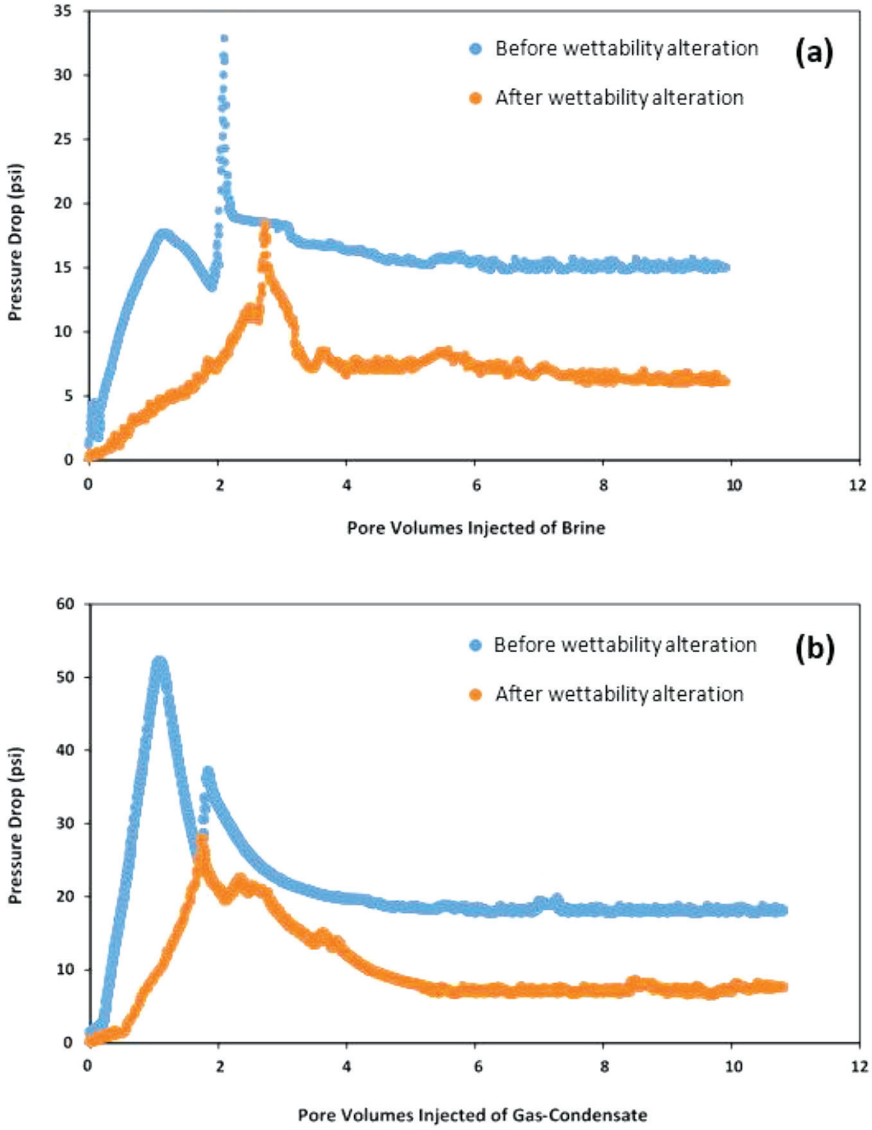

Fig. 10. The pressure drop across the core versus pore volumes injected of (a) brine and (b) condensate before and after treatment with ZnO/SiO_2 nanofluid.

Table 1. Liquid effective permeability and relative permeability data, before and after wettability alteration

System	Liquid effective and relative permeability					
	Pre-treatment		Post-treatment		change	
	K_{el} (mD)	K_{rl}	K_{el} (mD)	K_{rl}	(%) $\Delta K_{el} / K_{el}$	(%) K_{rl} / K_{rl}
Gas/Brine	3.20	0.29	7.38	0.70	+130	+141
Gas/liquid condensate	3.60	0.33	8.14	0.78	+126	+136

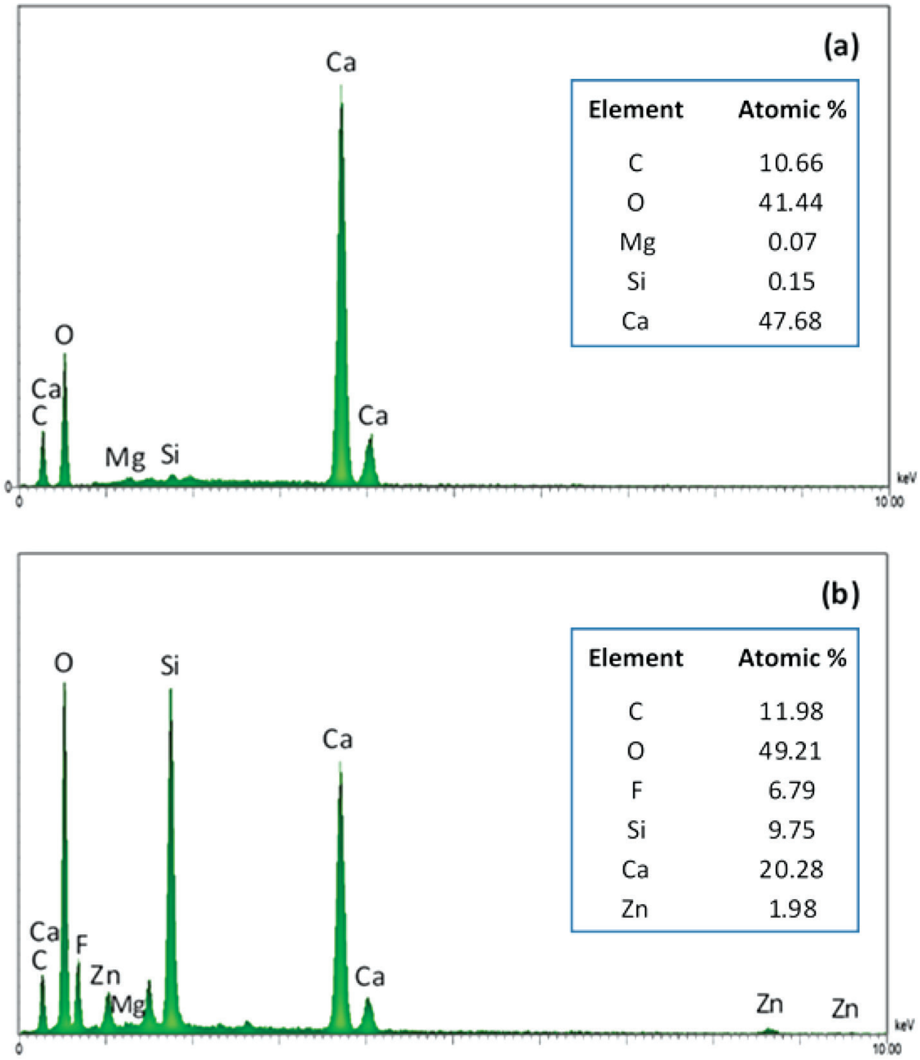

(a)

Element	Atomic %
C	10.66
O	41.44
Mg	0.07
Si	0.15
Ca	47.68

(b)

Element	Atomic %
C	11.98
O	49.21
F	6.79
Si	9.75
Ca	20.28
Zn	1.98

Fig. 11. EDX analysis of carbonate core (a) before and (b) after aging in ZnO/SiO_2 nanofluid.

4. Conclusion

Liquid blockage (water or condensate accumulation) near the wellbore regions leads to major productivity reduction in gas condensate reservoirs. Through wettability alteration to gas-wetting, the mobility of liquid phase for a gas/liquid system increases remarkably, showing great potential for enhancing the gas-well deliverability. It is successfully changed the wettability of carbonate reservoir rocks from strongly liquid-wetting to super water- and highly oil-repellent condition using a novel formulated nanofluid consisted of synthesized ZnO/SiO_2 nanocomposites and fluorochemicals PTFE, TFE, and PFOS. The water (distilled water or brine) and oil (n-decane or liquid gas-condensate) contact angle increased significantly from 0° to 162° and about 135°, respectively, after treatment of the rock with the prepared nanofluid. It is also observed that the rock surface exhibit excellent self-cleaning ability due to the minimum contact angle hysteresis (0°) and very low sliding angle (<2°) for water. Surface characterization of the treated plates was carried out by SEM, SP, and EDX analyses. Accordingly, the improved super liquid-repellency is attributed to the roughness of the nanocomposites that adsorb onto microscale texture of rock and the low surface energy of fluoro-containing materials. Moreover, our measurements of core displacement tests indicate that treatment of wettability alteration to ultra gas-wetting using ZnO/SiO_2 nanofluid is promisingly effective. It is found that such a wettability alteration decreases the pressure drop across the core which leads to a reduction of the amount of liquid trapping in pore space owing to a dominant increase in the liquid relative permeability. It is supposed the achieved results would pave the way for solving the problem of condensate blockage in gas condensate reservoirs.

Acknowledgments

The authors sincerely wish to thank Dr. Matthias Menzel from Fraunhofer Institute for Microstructure of Materials and Systems IMWS, Halle (Germany) for performing SP experiments. We do also gratefully acknowledge Dr. Pegah Esmaeilzadeh and Dr. Stefan L. Schweizer from Martin Luther University Halle-Wittenberg of Germany for their worthful help with the SP analyses.

References

[1] D. Afidick, N.J. Kaczorowski, S. Bette, Production performance of a retrograde gas reservoir: a case study of the Arun Field, in: SPE Asia Pacific Oil and Gas Conference, Melbourne, Australia, 1994.
[2] A. El-Banbi, W.D. McCain, M.E. Semmelbeck, Investigation of well productivity in gas-condensate reservoirs, in: SPE/CERI Gas Technology Symposium, Calgary, Canada, 2000.
[3] M.P. Cimolai, R.M. Gies, D.B. Bennion, D.L. Myers, Mitigating horizontal well formation damage in a low-permeability conglomerate gas reservoir, in: SPE gas Technology Symposium, Calgary, Canada, 1993.
[4] K. Li, A. Firoozabadi, Phenomenological modeling of critical condensate saturation and relative permeabilities in gas/condensate systems, SPE Journal, 5 (2000) 138-147.
[5] K. Li, A. Firoozabadi, Experimental study of wettability alteration to preferential gas-wetting in porous media and its effects, SPE Reservoir Evaluation and Engineering, 3 (2000) 139-149.
[6] G.Q. Tang, A. Firoozabadi, Wettability alteration to intermediate gas-wetting in porous media at elevated temperatures, Transport in Porous Media, 52 (2003) 185-211.
[7] V. Kumar, G.A. Pope, M.M. Sharma, Improving the gas and condensate relative permeability using chemical treatment, in: SPE Gas Technology Symposium, Calgary, Canada, 2006.
[8] M. Fahes, A. Firoozabadi, Wettability alteration to intermediate gas-wetting in gas condensate reservoirs at high temperatures, SPE Journal, 12 (2007) 397-407.
[9] M. Noh, A. Firoozabadi, Wettability alteration in gas-condensate reservoirs to mitigate well deliverability loss by water blocking, SPE Reservoir Evaluation and Engineering, 11 (2008) 676-685.
[10] X. Xie, Y. Liu, M. Sharma, W.W. Weiss, Wettability alteration to increase deliverability of gas production wells, Journal of Natural Gas Science and Engineering, 1 (2009) 39-45.
[11] S. Wu, A. Firoozabadi, Permanent Alteration of porous media wettability from liquid-Wetting to intermediate gas-wetting, Transport in Porous Media, 85 (2010) 189-213.
[12] K. Li, Y. Liu, H. Zheng, G. Huang, G. Li, Enhanced gas-condensate production by wettability alteration to gas wetness, Journal of Petroleum Science and Engineering, 78 (2011) 505-509.
[13] S. Sharifzadeh, S. Hassanajili, M.R. Rahimpour, Wettability alteration of gas condensate reservoir rocks to gas wetness by sol-gel process using fluoroalkylsilane, Journal of Applied Polymer Science, 128 (2012) 4077-4085.
[14] C. Feng, Y. Kong, G. Jiang, J. Yang, C. Pu, Y. Zhang, Wettability modification of rock cores by fluorinated copolymer emulsion for the enhancement of gas and oil recovery, Applied Surface Science, 258 (2012) 7075-7081.
[15] S.K. Das, S.U.S. Choi, W. Yu, T. Pradeep, Nanofluids: Science and Technology, John Wiley & Sons, Inc Publishing, Hoboken, New Jersey, 2008.
[16] R. Taylor, S. Coulombe, T. Otanicar, P. Phelan, A. Gunawan, W. Lv, G. Rosengarten, R. Prasher, H. Tyagi, Small particles, big impacts: a review of the diverse applications of nanofluids, Journal of Applied Physics, 113 (2013) 0113011–01130119.
[17] D. Tripathi, O. Bég, A study on peristaltic flow of nanofluids: Application in drug delivery systems, International Journal of Heat and Mass Transfer, 70 (2014) 61-70.
[18] H.T. Phan, N. Caney, P. Marty, S. Colasson, J. Gavillet, Surface coating with nanofluids: the effect of pool boiling heat transfer, Nanoscale and Microscale Thermo Physical Engineering, 14 (2010) 229-244.
[19] D. Wen, G. Lin, S. Vafaei, K. Zhang, Review of nanofluids for heat transfer applications, Particuology, 7 (2009) 141-150.
[20] D.T. Wasan, A.D. Nikolov, Spreading of nanofluids on solids, Nature, 423 (2003) 156-159.

[21] R. Saidur, K.Y. Leong, H.A. Mohammad, A review on applications and challenges of nanofluids, Renewable and Sustainable Energy Reviews, 15 (2011) 1646-1668.

[22] A. Karimi, Z. Fakhroueian, A. Bahramian, N. Pour Khiabani, J. Babaee Darabad, R. Azin, S. Arya, Wettability Alteration in Carbonates using Zirconium Oxide Nanofluids: EOR Implications, Energy and Fuels, 26 (2012) 1028-1036.

[23] L. Hendraningrat, O. Torsæter, A coreflood investigation of nanofluid enhanced oil recovery, Journal of Petroleum Science and Engineering, 111 (2013) 128-138.

[24] B.A. Suleimanov, F.S. Ismailov, E.F. Veliyev, Nanofluid for enhanced oil recovery, Journal of Petroleum Science and Engineering, 78 (2011) 431-437.

[25] J.S. Nam, P. Lee, S.W. Lee, Experimental characterization of micro-drilling process using nanofluid minimum quantity lubrication, International Journal of Machine Tools and Manufacture, 51 (2011) 649-652.

[26] S. Mokhatab , M.A. Fresky , M.R. Islam Applications of nanotechnology in oil and gas E&P, Journal of Petroleum Technology, 58 (2006) 48-51.

[27] M.S. Zaman, M.R. Islam, S. Mokhatab, Nanotechnology Prospects in the Petroleum Industry, Petroleum Science and Technology, 30 (2012) 1053-1058.

[28] M. Mousavi, S. Hassanajili, M.R. Rahimpour, Synthesis of fluorinated nano-silica and its application in wettability alteration near-wellbore region in gas condensate reservoirs, Applied Surface Science, 273 (2013) 205-214.

[29] M. Aminnaji, H. Fazeli, A. Bahramian, S. Gerami, H. Ghojavand, Wettability alteration of reservoir rocks from liquid wetting to gas wetting using nanofluid, Transport in Porous Media, 109 (2015) 201-206.

[30] Y. Hwang, J. Lee, J. Lee, Y. Jeong, S. Cheong, Y. Ahn, S. Kim, Production and dispersion stability of nanoparticles in nanofluids, Powder Technology, 186 (2008) 145-153.

[31] A. Ghadimi, R. Saidur, M. H., A review of nanofluid stability properties and characterization in stationary conditions, International Journal of Heat and Mass Transfer, 54 (2011) 4051-4068.

[32] I. Uysal, F. Severcana, Z. Evis, Characterization by Fourier transform infrared spectroscopy of hydroxyapatite co-doped with zinc and fluoride, Ceramics International, 39 (2013) 7727-7733.

[33] K. Sowri babu, A. ramachandra Reddy, C. Sujatha, K. Venugopal Reddy, A.N. Mallika, Synthesis and optical characterization of porous ZnO, Journal of Advanced Ceramics, 2 (2013) 260-265.

[34] J.V.G. Tinio, K.T. Simfroso, A.D.M. Peguit, R.T. Candidato Jr, Influence of OH^- Ion Concentration on the Surface Morphology of ZnO-SiO_2 Nanostructure, Journal of Nanotechnology, 2015 (2015) 1-7.

[35] E.G. Pantohan, R.T. Candidato Jr, R.M. Vequizo, Surface characteristics and structural properties of sol-gel prepared ZnO-SiO_2 nanocomposite powders, IOP Conference Series: Materials Science and Engineering, 79 (2015) 1-6.

[36] J. El Ghoul, K. Omri, L. El Mir, C. Barthou, S. Alaya, Sol–gel synthesis and luminescent properties of SiO_2/Zn_2SiO_4 and SiO_2/Zn_2SiO_4:V composite materials, Journal of Luminescence, 132 (2012) 2288-2292.

[37] S. Tripathi, R. Bose, R. Roy, S. Nair, N. Ravishankar, Synthesis of hollow nanotubes of Zn_2SiO_4 or SiO_2: mechanistic understanding and uranium adsorption behavior, Appled Materials and Interfaces, 7 (2015) 26430-26436.

[38] H. Butt, C. Semprebon, P. Papadopoulos, D. Vollmer, M. Brinkmann, M. Ciccott, Design principles for superamphiphobic surfaces, Soft Matter, 9 (2013) 418-428.

[39] N. Valipour Motlagh, F.C. Birjandi, J. Sargolzaei, N. Shahtahmassebi, Durable, superhydrophobic, superoleophobic and corrosion resistant coating on the stainless steel surface using a scalable method, Applied Surface Science, 283 (2013) 636-647.

[40] H. Ogihara , J. Xie , J. Okagaki , T. Saji Simple Method for Preparing Superhydrophobic Paper: Spray-Deposited Hydrophobic Silica Nanoparticle Coatings Exhibit High Water-Repellency and Transparency, Langmuir 28 (2012) 4605-4608.

[41] P. Muthiah, B. Bhushan, K. Yun, H. Kondo, Dual-layered-coated mechanically-durable superomniphobic surfaces with anti-smudge properties, Journal of Colloid and Interface Science, 409 (2013) 227-236.

[42] M. Nosonovsky, B. Bhushan, Superhydrophobic surfaces and emerging applications: Non-adhesion, energy, green engineering, Current Opinion in Colloid and Interface Science, 14 (2009) 270-280.

[43] E. Celia, T. Darmanin, E.T. Givenchy, S. Amigoni, F. Guittard, Recent advances in designing superhydrophobic surfaces, Journal of Colloid and Interface Science, 402 (2013) 1-18.

[44] N. Valipour Motlagh, F.C. Birjandi, J. Sargolzaei, Super-non-wettable surfaces: A review, Colloids and Surfaces A: Physicochemical and Engineering Aspects, 448 (2014) 93-106.

[45] A.B.D. Cassie, S. Baxter, Wettability of porous surfaces, Transactions of the Faraday Society, 40 (1994) 546-551.

[46] Q. Xie, J. Xu, L. Feng, L. Jiang, W. Tang, X. Luo, C.C. Han, Facile creation of a super-amphiphobic coating surface with bionic microstructure, Advanced Materials, 16 (2004) 302-305.

[47] T. Nishino, M. Meguro, K. Nakamae, M. Matsushita, Y. Ueda, The lowest surface free energy based on $-CF_3$ alignment, Langmuir, 15 (1999) 4321-4323.

[48] S. Shibuichi, T. Yamamoto, T. Onda, K. Tsujii, Super water- and Oil-repellent surfaces resulting from fractal structure, Journal of Colloid and Interface Science, 208 (1998) 287-294.

Asphaltene and Normal Paraffin Effect on Gas-Oil Interfacial Tension During CO_2 Injection into Asphaltenic Oil Reservoir

- Masoud Riazi
  Enhanced Oil Recovery (EOR) Research Centre, School of Chemical and Petroleum Engineering, Shiraz University, Shiraz, Iran
- Yousef Kazemzadeh
  Department of Petroleum Engineering, School of Chemical and Petroleum Engineering, Shiraz University, Shiraz, Iran
- Rafat Parsaei
  Department of Petroleum Engineering, School of Chemical and Petroleum Engineering, Shiraz University, Shiraz, Iran
  * (E-mail: sadeghi@iust.ac.ir)

Received: Dec 25, 2016/ Accepted: March 8, 2017

Abstract

Asphaltene precipitation in oil reservoirs has been involved with numerous problems. Therefore, it is required to understand the precipitation mechanisms in detail in order to diminish the associated difficulties. There are several ways to detect asphaltene precipitation. One of these methods is vanishing interfacial tension (VIT) method. In this method by plotting the equilibrium interfacial tension (IFT) versus pressure, the asphaltene precipitation conditions can be predicted. In this study, for more accurate evaluation of asphaltene precipitation in oil reservoirs by using IFT versus pressure plots, synthetic oil solutions made up of toluene and normal paraffins are used. Solutions with different compositions of toluene and normal paraffins such as n-decane and n-heptane with and without asphaltene (extracted from crude oil) are prepared. Then, the equilibrium IFT of the solutions in the proximity of CO_2 at different pressure conditions is measured. By plotting the IFT data versus pressure, the onset of asphaltene precipitation in presence of gas and the impact of different parameters on this phenomenon are investigated. Experimental results show that the presence of asphaltene in synthetic solutions changes the behavior of IFT data with pressure. For a solution of toluene and normal paraffin containing asphaltene, the IFT of the solution in presence of CO_2 decreases linearly with two different slopes at low and high pressure ranges. The results confirm that the presence of normal paraffin intensifies asphaltene precipitation. The experimental results show that the higher mass fraction of asphaltene is, the higher would be the intensity of the asphaltene precipitation for the attempted mass fractions.

Keywords: asphaltene precipitation, interfacial tension, minimum pressure of miscibility, carbon dioxide, normal paraffin.

1. Introduction

Nature of heavy organics in crude oil and their role in extraction, transfers and processing, has been well understood [1-3]. Comprehensive investigations at different area such as exploration, drilling, production, enhanced oil recovery and processing of low quality oil have been performing. Injection and re-injection of gas into oil reservoirs are cost-effective methods [4]. One of the major problems in these recovery processes is blockage of pores by asphaltene precipitation, which could significantly reduce oil recovery efficiency [5]. Combination of a miscible fluid with oil could significantly affect phase behavior. However, precipitation of heavy organic materials is a major drawback of phase change that could consequently affect production from oil reservoirs or oil flow rate through wells and pipelines [6]. Precipitation of heavy organic material usually yields pore blockage and wettability alteration of reservoir rock [7].

Asphaltene precipitation in porous media can also lead to a decrease of 20 percent effective permeability [8-9]. Due to damage to the formation, oil and gas production rate from the reservoir decreases [9]. When the reservoir pressure is close to the precipitation pressure, asphaltene precipitation in reservoir takes place; this creates a failure condition at the wellbore [10]. Asphaltene precipitation process and its consequences have been shown to be very complex [11-12].

Various methods has been used and proposed to detect asphaltene precipitation process. These methods include microscopic method [13], light absorption method [14], gravimetric method, electrical conductivity method [15], viscometer method, heat transfer measuring method and vanishing interfacial tension (VIT) method [16-17]. The vanishing interfacial tension (VIT) method is a new method that can accurately detect the starting point of asphaltene precipitation [18-19]. In this method, the equilibrium IFT data of oil and gas is plotted against pressure, and the trend of the resultant curve is interpreted to discover mechanisms, the start point and intensity of asphaltene precipitation [20]. In this method, as soon as the precipitation starts, the trend of the IFT plot versus pressure changes sharply [21]. This method is quite accurate, and a small amount of sample is required for evaluation [22]. The optimum conditions of miscible gas injection can be determined using the rapid VIT method [22-23].

The VIT method has been developed and employed to measure the miscibility conditions of various crude oils with deferent gases. The following are some of the studies in this field. Nobakht et al. showed that equilibrium CO_2 gas-oil IFT often reduces linearly with pressure to the pressure from which the IFT-pressure trend changes. This pressure is known as threshold pressure. They also observed that if the equilibrium pressure is higher than the threshold pressure, light oil components quickly get out from the oil droplet and turn into the gas phase. This physical phenomenon is known as the extraction of very light components [24].

Nobakht et al. also measured the solubility of CO_2 at different equilibrium pressures and at 27 °C. They concluded that by extrapolating the first slope of the IFT data versus pressure down to the point at which IFT becomes zero, the minimum miscible pressure (MMP) can be estimated [25].

Wang et al. investigated the interaction of three Canadian crude oil (two light oil and a medium one) with CO_2, by using the VIT method. They found that the equilibrium IFT decreases linearly with the equilibrium pressure at three distinct pressure ranges. In the first interval, with increasing pressure, IFT reduces due to increasing solubility of CO_2 in oil. In the second interval, IFT suddenly increases, then quickly decreases, and again becomes linear. They stated that the sudden increase in IFT was owing to asphaltene precipitation, and rapid separation of light compositions. They concluded that, in this range, the measured IFT is between relatively heavy compositions of crude oil and CO_2. At the last stage, different light components began to separate from oil. At this stage, the measurement of IFT is between the heaviest compositions of crude oil and CO_2 gas [26].

In this study the impact of parameters such as pressure, asphaltene content and oil composition on asphaltene precipitation is investigated through VIT method.

2. Experimental

Synthetic solutions are prepared by mixing different amounts of toluene, normal paraffins and asphaltene, which was extracted from an Iranian crude oil sample. The composition of this crude oil sample is shown in Table 1.

To extract asphaltene from crude oil, different standards are available. In this study, the ASTM (D2007-80) was applied [17].

After extracting asphaltene from the crude oil sample, synthetic oil sample is prepared. Asphaltene is insoluble in the normal paraffins; however, it is soluble in toluene due to similar ring structure. To study the effect of synthetic oil composition on IFT, solutions with different volume percent of toluene and normal paraffins are used. For preparing the samples, the normal paraffins and toluene, with desired volume percents are mixed. Then, 5 wt% asphaltene is added and the prepared mixture is shaken for 6 hours by magnetic stirrer so that the whole asphaltene dissolves in the solution. Table 2 shows 18 oil solutions used in IFT tests.

Table 2. Compounds of solutions used as oil in IFT experiments

Component	CO_2	C_1	C_2	C_3	iC_4	nC_4	iC_5	nC_5	C_6	C_7	C_8	C_9	C_{10}	C_{11}	C_{12}^+
Mole fraction	0.01	0.38	0.51	1.28	0.44	1.84	1.44	2.33	7.43	8.73	6.74	8.69	7.73	5.04	47.41

Table 1. Composition of the oil used for asphaltene extraction

Sample	Toluene (volume percent)	n-Heptane (volume percent)	n-Decane (volume percent)	Asphaltene (mass percent)
T-100-A	100	0	0	0
T-100-B	100	0	0	wt% of the solution 5
H-10-A	90	10	0	0
H-10-B	90	10	0	wt% of the solution 5
H-20-A	80	20	0	0
H-20-B	80	20	0	wt% of the solution 5
H-30-A	70	30	0	0
H-30-B	70	30	0	wt% of the solution 5
H-40-A	60	40	0	0
H-40-B	60	40	0	wt% of the solution 5
D-10-A	90	0	10	0
D-10-B	90	0	10	wt% of the solution 5
D-20-A	80	0	20	0
D-20-B	80	0	20	wt% of the solution 5
D-30-A	70	0	30	0
D-30-B	70	0	30	wt% of the solution 5
D-40-A	60	0	40	0
D-40-B	60	0	40	wt% of the solution 5

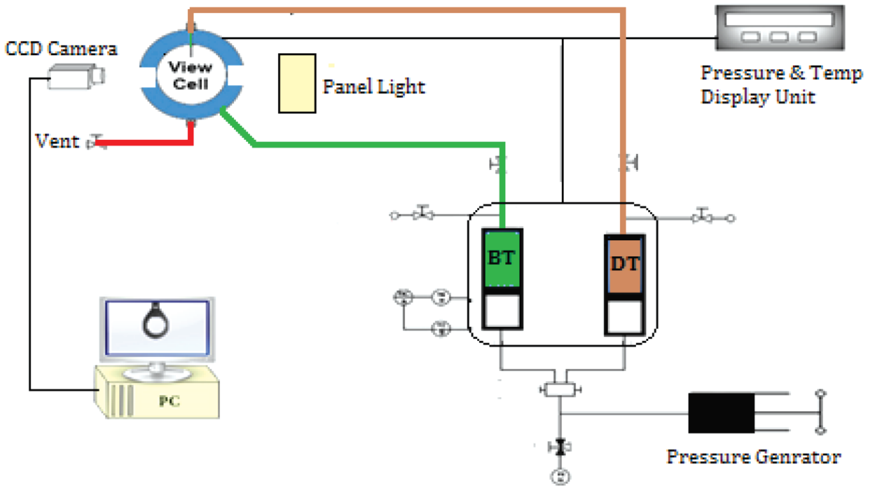

Figure 1. Schematic illustration of the experimental setup

CO_2 gas (with a purity of more than 99.99%) was prepared from a local company. The pendant drop method was applied to determine the IFT of gas-oil at reservoir conditions. Figure 1 shows the IFT measuring device, which includes a visible high pressure chamber.

The apparatus also includes a high pressure pump and a pressure gauge employed to measure the pressure in the system. The whole system is covered with a controllable thermal chamber. The IFT device is equipped with a high resolution camera, which is located at one side of the chamber, and a light source placed at the other side of the chamber. The camera is connected to a computer with drop shape analysis software to estimate the IFT of oil and gas based on the shape of the pendant drop.

The IFT value is very sensitive to impurities; therefore, cleaning different parts of the device is very crucial; hence, before starting any test, cleaning of the inside parts of the device is performed by injecting toluene, then, acetone followed by rinsing with de-ionized water. To start a test, the oil phase is transferred into the droplet fluid storage tank (DT) using a piston and the gas phase is transferred into the bulk fluid storage tank (BT). Next, the temperature of visible chamber and reservoir tanks of bulk fluid and drop are set to a desired temperature. A pressure producer is used to inject the gas into the cell and to pressurize it at a desired value. A capillary tube is mounted at the top of the high pressure cell from which the oil droplet is injected to the bulk gas. To achieve equilibrium conditions (i.e. constant temperature and pressure conditions) enough time should be given. Then the IFT between two fluids is recorded over time until reaching the thermodynamic equilibrium conditions. In order to reach to thermodynamic equilibrium at a shorter time, several drops (20-30 drops) of oil are injected into the chamber. The test is considered at the equilibrium condition when the IFT does not change with time significantly. All experiments were performed at constant temperature of 323.15 K. To estimate IFT, it is necessary to determine the density of two fluids at experimental temperature and pressure conditions. Therefore, the fluids density was measured at different pressures and temperatures using a hydrometer (Anton Parr device) with high accuracy (i.e., 0.00001 (g/ml) .)Density of CO_2 gas at any pressure and temperature is taken from valid references [27].

3. Results and Discussion

3. 1 Impact of normal paraffin on asphaltene precipitation

Interfacial tension of toluene-n heptane solutions and CO_2 gas was measured at different pressure conditions ranging from 3 to 7 MPa and the temperature of 323.15 K, and the results are shown in Figure 1. Since n-heptane is lighter than toluene (in terms of molecular weight), as more heptanes is added to the mixture, molecular weight of the solution decreases. Thus, the IFT between synthetic solution and CO_2 decreases by increasing the heptanes content.

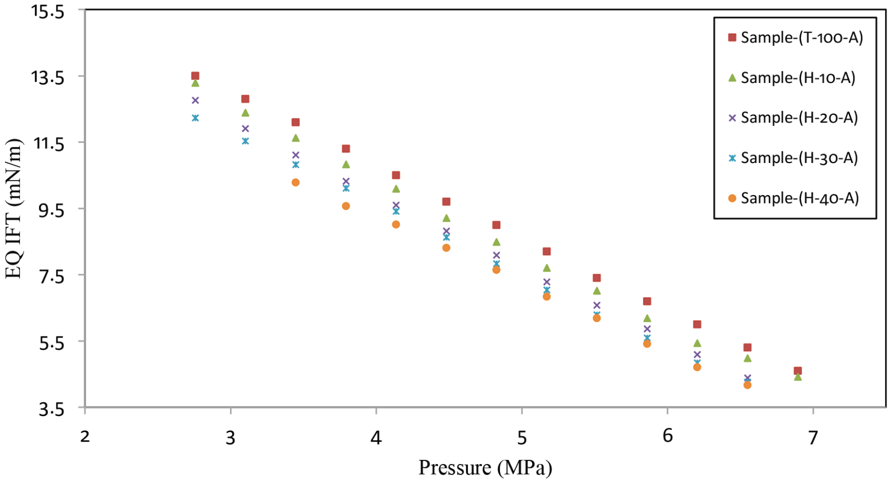

Figure 2. The equilibrium IFT versus pressure diagram of toluene-n heptane and CO_2 solutions at temperature 323.15 K

The linear data presented in Figure 2 shows that the difference between IFT data of various solutions reduces at high pressure conditions. That is at high pressures the impact of heptane content on IFT values reduces. The IFT of toluene-normal paraffins solutions containing 5 wt% asphaltene with CO_2 was measured in order to investigate the impact of asphaltene on IFT in the synthetic solutions. Figure 3 shows the IFT of toluene-n heptane-asphaltene and CO_2 at different pressures.

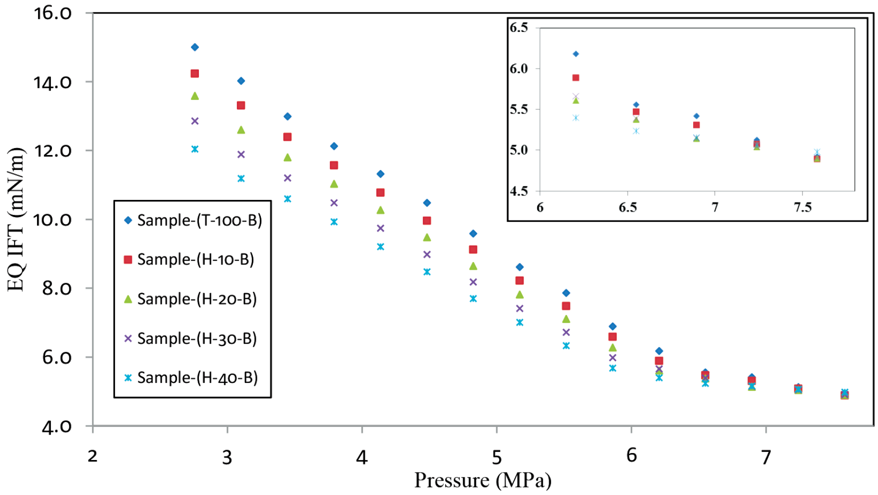

Figure 3. The equilibrium IFT versus pressure diagram of toluene-n heptane-asphaltene and CO_2 at 323.15K

As shown in Figure 3, IFT decreases with two different trends at low and high pressure intervals. The IFT reduction at low pressure interval (i.e. 3-5.5 MPa) could be mainly due to higher mass transfer between the gas and oil phase as the system is more pressurized. As pressure increases, more CO_2 dissolves in the oil phase and hence the oil phase swells and gas-oil IFT decreases. However, the rate of IFT reduction at high pressure range (i.e. 6-8 MPa) is smaller compared to that of the low pressure interval. At high pressure range, although dissolving CO_2 causes the reduction of IFT value, accumulation of asphaltene at the interface of the oil phase and CO_2 occurs, which results in increasing IFT. Increasing trend of IFT critically intensifies when the surface coverage of the particles surpassed a threshold value (e.g., + 60 % surface coverage) [28-29]. However, the effect of CO_2 solubility on IFT is more intense than surface coverage. Therefore, at high pressure range the rate of IFT reduction is much smaller than that of the first interval.

From the experimental data shown in Figure 3, it can be also concluded that as the heptane content increases in the oil solution, more asphaltene accumulation and precipitation would take place. Tracking the trends of the plots indicates that upon raising the heptane content of the oil solution, the second trend starts at a lower pressure. This means that asphaltene starts to precipitate at lower pressures if heptane content of the test oil increases.

Table 3 shows the correlations obtained to relate IFT and pressure for each one of the oil solutions at two different pressure regions. The first column of the table specifies the tested sample. The second column shows the test pressure ranges and correlations relating IFT to pressure are given in the third column. The corresponding R^2 values for each of the proposed equations are reported in the fourth column, showing the goodness of fit. Minimum miscible pressure was estimated for each mixture by putting P equal to zero in the pertinent IFT-pressure correlation and is presented in the fifth column. The last column shows the percent increase of minimum miscible pressure calculated from the second interval equation compared to that of the first period.

Table 3. IFT and minimum miscible pressure of different mixtures of toluene-n heptane-asphaltene and CO_2 at temperature of 323.15 K

Sample	Pressure P:	IFT vs Pressure correlation P:	R^2	MMP (MPa)	FCM / MCM
Sample-(T-100-B)	$2.75 \leq P \leq 6.55$	$IFT = -2.5096P + 21.73$	0.9984	8.66	1.76
	$6.55 \leq P \leq 7.58$	$IFT = -0.6410P + 9.79$	0.9844	15.27	
Sample-(H-10-B)	$2.75 \leq P \leq 6.21$	$IFT = -2.4173P + 20.79$	0.9995	8.60	1.79
	$6.21 \leq P \leq 7.58$	$IFT = -0.6236P + 9.60$	0.9913	15.40	
Sample-(H-20-B)	$2.75 \leq P \leq 6.21$	$IFT = -2.3018P + 19.79$	0.9993	8.59	1.91
	$6.21 \leq P \leq 7.58$	$IFT = -0.5511P + 9.03$	0.9548	16.38	
Sample-(H-30-B)	$2.75 \leq P \leq 6.21$	$IFT = -2.1925P + 18.79$	0.9994	8.57	1.95
	$6.21 \leq P \leq 7.58$	$IFT = -0.5337P + 8.91$	0.9627	16.70	
Sample-(H-40-B)	$2.75 \leq P \leq 5.76$	$IFT = -2.0503P + 17.65$	0.9994	8.60	2.39
	$5.76 \leq P \leq 7.58$	$IFT = -0.3787P + 7.80$	0.9302	20.59	

As shown in Table 3, for each oil solution, the IFT plot versus pressure could be treated as two lines with two different slopes for low and high pressure ranges. The decrease of IFT with pressure in the first period could be related to the accumulation of asphaltene particles [23], and the decrease in the second period would be caused by asphaltene precipitation at the interface [23]. The latter gentle slope would be due to asphaltene precipitation, and consequently altering the intermolecular forces at the interface of two phases. As Figure 3 and the corresponding equations in Table 3 show, slope of the first and the second lines become gentler by increasing n-heptane content of the oil solution. For instance, for sample (T-100-B), which is free of n-heptane, decline slopes of the first and second period reduce from 2.5096 ((mN/m)/MPa) to 2.0503 ((mN/m)/MPa) and from 0.6410 ((mN/m) /MPa) to 0.3787 ((mN/m)/MPa), respectively, when the amount of n-heptane in the solution reaches to 40 percent. This change in the slopes could be an indication of this point that asphaltene precipitation in solutions containing n-heptane is more severe. According to the theory of vanishing interfacial tension (VIT), when IFT of two fluids becomes zero two fluids dissolve completely in each other. Based on the presented relationships in each of the pressure periods, there will be a certain pressure at which the IFT is zero. In the fourth column of Table 3, the minimum miscible pressure estimated from extrapolating the data of each period to zero IFT is given. As shown in this table, the minimum miscible pressure estimated from the first period is lower than that from the second period. This is because the minimum miscible pressure (MMP) estimated from the first period represents the multiple minimum miscible pressure (MCM) and the minimum miscible pressure estimated from the second period represents first contact miscible pressure conditions (FCM) [30]. The MMP at MCM conditions is not significantly affected by heptane content of the oil solution, whereas the MMP at FCM conditions is drastically affected by heptane content. The last column shows the ratio of the MMP estimated based on the data of the second period (high pressure range) to that based on the data of the first period (low pressure range). This column shows that this ratio increases as the heptane content increases. This could be due to asphaltene precipitation, which mainly increases the FCM pressure condition up to two times. The level of change in MMP shows the need for accurate prediction of asphaltene precipitation pressure.

Figure 4 shows the IFT versus pressure of toluene - n decane solutions in the proximity of CO_2 gas. Molecular weight of n-decane is closer to molecular weight of toluene compared to that of n-heptane. Therefore, the IFT values at a constant pressure are closer to each other for different solutions of n-decane and toluene in comparison with different solutions of n-heptane and toluene.

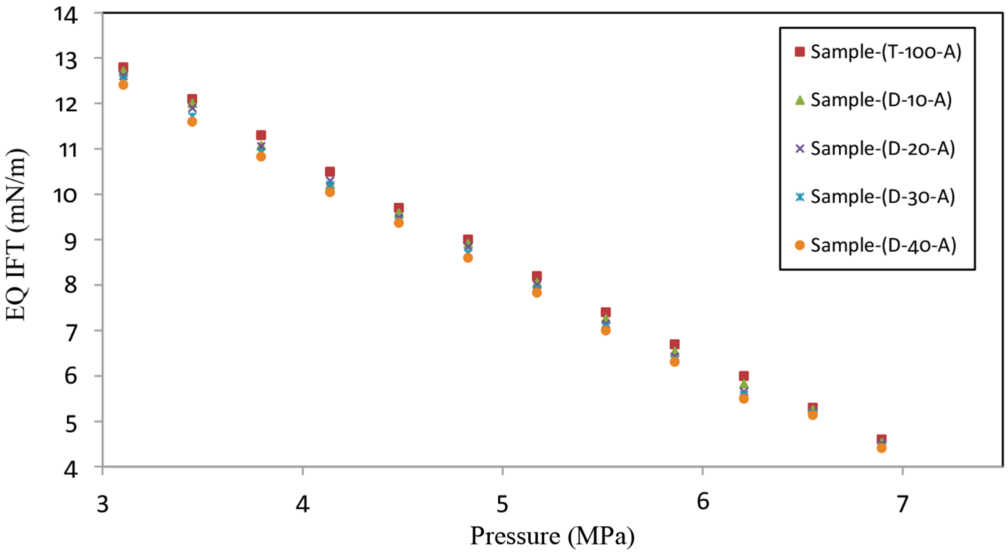

Figure 4. The equilibrium IFT versus pressure diagram of toluene-n decane solutions and CO_2 at temperature of 323.15 K

Figure 5 also shows that IFT values reduce linearly with pressure for different oil solutions and CO_2 systems.

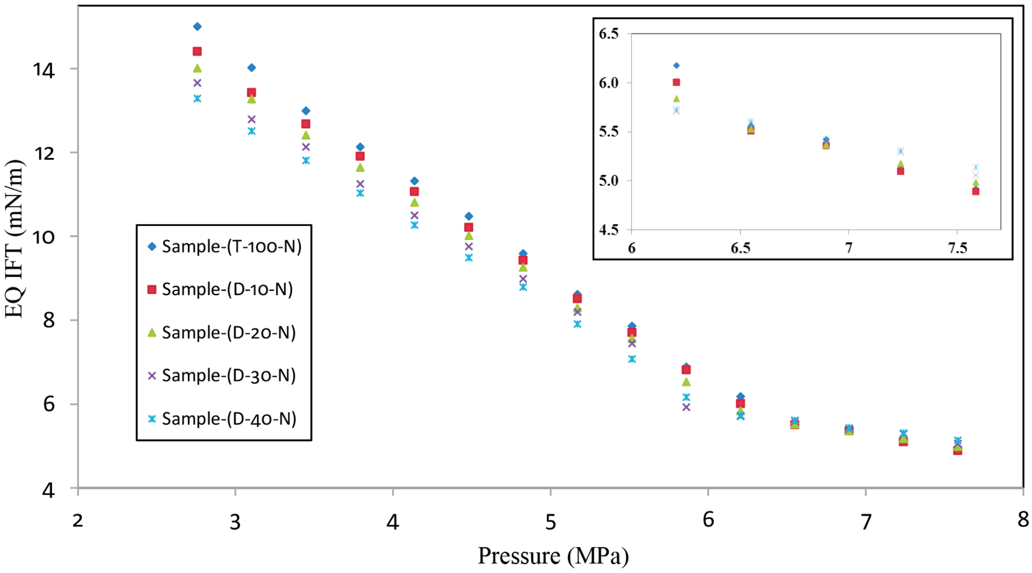

Figure 5. The equilibrium IFT versus pressure diagram of toluene-n decane-asphaltene solutions and CO_2 at 323.15 K

Figure 5 shows the IFT versus pressure of different toluene-n decane solutions with 5 wt% of asphaltene at temperature 323.15 K. Similar to the data of n-heptane solutions, these data can be divided into two groups, each with different slope. The trend of the experimental data specifies that asphaltene precipitation occurs at lower pressure, if the amount of n-decane in the oil solution increases.

Table 4 shows the equations fitted to the experimental data of IFT versus pressure for each of the oil solutions at two different pressure periods. The minimum miscible pressure estimated for each solution, and their percent increase in each period have been also reported in Table 4.

Table 4. IFT and minimum miscible pressure of mixtures of toluene-n decane-asphaltene and CO_2 at temperature of 323.15 K

Sample	**Pressure** P= (MPa)	**IFT vs Pressure correlation** $IFT: \left(\frac{mN}{m}\right)$ P= (MPa)	**R²**	**MMP (MPa)**	**FCM / MCM**
Sample-(T-100-B)	$2.75 \leq P \leq 6.55$	$IFT = -2.5096P + 21.73$	0.9984	8.66	1.76
	$6.55 \leq P \leq 7.58$	$IFT = -0.6410P + 9.79$	0.9844	15.27	
Sample-(D-10-B)	$2.75 \leq P \leq 6.55$	$IFT = -2.4205P + 21.05$	0.9997	8.70	1.79
	$6.55 \leq P \leq 7.58$	$IFT = -0.6149P + 9.56$	0.9904	15.55	
Sample-(D-20-B)	$2.75 \leq P \leq 6.21$	$IFT = -2.3893P + 20.68$	0.9993	8.65	1.84
	$6.21 \leq P \leq 7.58$	$IFT = -0.5946P + 9.48$	0.9859	15.94	
Sample-(D-30-B)	$2.75 \leq P \leq 6.21$	$IFT = -2.3578P + 20.23$	0.9934	8.58	1.97
	$6.21 \leq P \leq 7.58$	$IFT = -0.5641P + 9.51$	0.9873	16.87	
Sample-(D-40-B)	$2.75 \leq P \leq 6.21$	$IFT = -2.2694P + 19.615$	0.9990	8.64	2.26
	$6.21 \leq P \leq 7.58$	$IFT = -0.5462P + 9.24$	0.9960	19.57	

According to Table 4, as the amount of n-decane increases in the oil solution, asphaltene precipitation starts to occur at a lower pressure. Similar to heptane solutions, FCM pressure increases more than MCM pressure as n-decane in the oil solution increases.

3.2. Impact of asphaltene content on precipitation

As stated before, the change and rate of change of the IFT slopes specify the onset and strength of asphaltene precipitation. Figure 6 shows the impact of asphaltene mass fraction in the synthesized solutions on the change of IFT slope at different pressure regions and consequently the intensity of asphaltene precipitation.

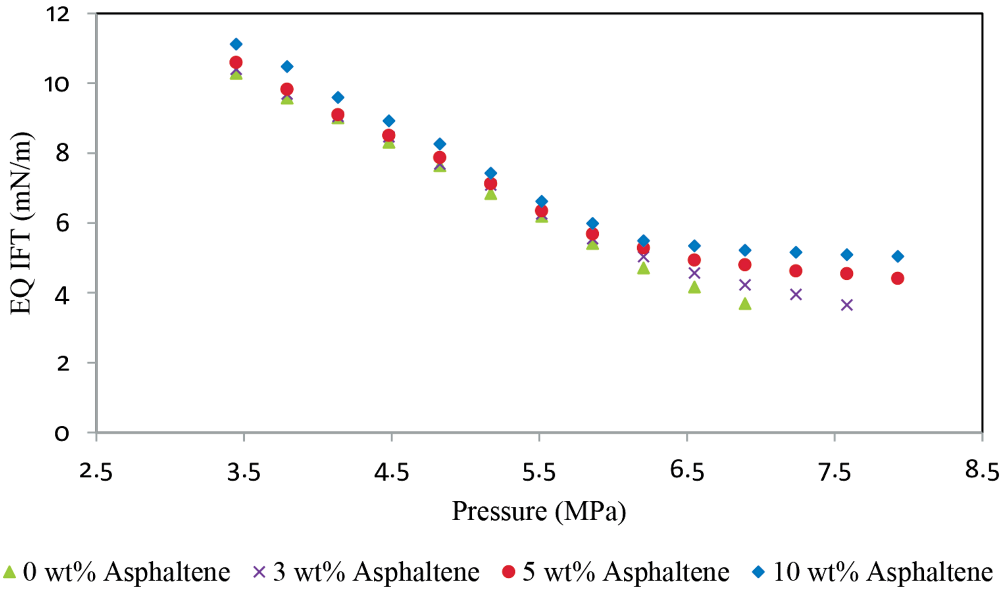

Figure 6. The equilibrium IFT versus pressure for CO_2 and oil solutions with different asphaltene content at temperature 323.15 K

Figure 6 also illustrates the variation of IFT versus pressure for different mass fractions of asphlatene in the solution along with CO_2 gas. At low pressures i.e. the first region, IFT decreases as pressure increases with a sharp slope, though, the trend is nearly similar for all four tested solutions. However, at high pressures, because of asphaltene precipitation, the rate of IFT reduction declines for all three solutions containing asphaltene (3, 5, 10 wt%). Nevertheless, for solution with 10 wt% asphaltene the slope of second region is the smallest compared to those of other two solutions because of more asphaltene precipitation. Intense precipitation of large asphaltene molecules in this solution at the interface of CO_2 gas and oil has led to disruption of intermolecular forces and IFT increase. Percentage change in the slope of the second region than in the first region is an appropriate criterion for assessment of the rate of asphaltene precipitation. Figure 7 shows the percent of change in the slope of the second region than the slope of the first region for four solutions with different asphaltene percent.

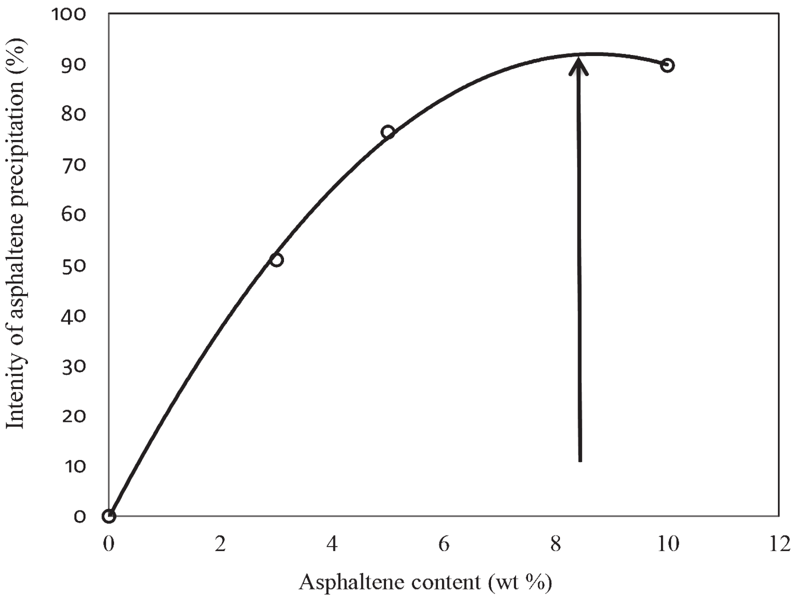

Figure 7. Intensity of asphaltene precipitation for four solutions with different asphaltene content

According to figure 7, increasing asphaltene particles increases asphaltene aggregation at the surface. In the second region (e.g., + 60 % surface coverage) the asphaltene particles aggregation increases the IFT, on the other hand, the CO_2 solubility decreases the IFT. Therefore, the percent change in the slope of the second region in comparison with the first region increases with increasing asphaltene content. The maximum asphaltene precipitation is for 8-9% asphaltene solutions, according to the second polynomial function. This means that the suspended particles do not tend to be at the fluids interface after surpassing a certain concentration. Therefore, the increase of IFT extent, which is because of asphaltene precipitation at fluids interface, decreases and asphaltene precipitation extent decreases accordingly.

3. 3. Validating the experimental data

The reproducibility of the experimental results presented here was examined by repeating the IFT test three times at each pressure and temperature conditions. The amount of the standard deviation between the data was observed to be less than 0.1 (mN/m). In this study, average of three data was used as the IFT corresponding to the desired pressure and temperature conditions. To compare the measured data from the experiments of this study with those from the previous studies, the IFT of n-heptane and CO_2 versus pressure were measured at temperatures of 333.15 and 323.15 K. The estimated minimum miscible pressure (using vanishing interfacial tension in this study) is compared with the values estimated from the similar systems in other studies [22, 31]. The results are shown in Table 5.

Table 5. The experimental results of this study versus the literature data

	$T = 323.15$ K			$T = 333.15$ K		
	Experimental Result	Ref [22]	Percent Difference	Experimental Result	Ref [31]	Percent Difference
Decline Slope (10^9 m)	1.90	2	% -5	1.63	1.64	-0.60%
Estimated MMP (MPa)	8.40	8.5	% -1.2	8.93	9.00	-0.77%

4. Conclusions

Based on the results of this study, the following conclusions can be drawn:

- IFT data of toluene-normal paraffins solutions, containing asphaltene and CO_2, versus pressure shows two different slopes. The data in the first interval represents the conditions at which the solubility of CO_2 gas in the oil solution takes place, while the second slope represents the asphaltene precipitation conditions at the interface of two phases (i.e. oil and gas). With increase in the normal paraffin content in the solution both slopes decrease, however, the decrease of the second slope is more pronounced. The asphaltene particles cover the interface of two fluids more rapidly by increasing the n-paraffin content of the oil phase, consequently:

i) n-paraffins act as the asphaltene particles instability compounds, therefore, increasing normal paraffins means transferring more asphaltene to the fluids interface and hence increasing IFT. On the other side, CO_2 solubility decreases IFT. The overall effect is that these two opposite factor make the slope of interfacial tension versus pressure plot to change at a lower pressure, showing that the asphaltene precipitates earlier.

ii) Increasing n-paraffin means putting more asphaltene particles at the fluid surface. Thus, at a specific pressure for second region, by increasing n-paraffin, the size of asphaltene particles at surface grows. Accordingly, the IFT gets larger. On the other hand, rising pressure makes CO_2 more soluble in the oil. This event decreases the IFT. Consequently, these two inconsistent phenomena cause lower slope for IFT plot and more n-heptane inside the oil drop.

Therefore, normal paraffin in the oil solution containing asphaltene improves and accelerates asphaltene precipitation.

- In oil solution-CO_2 systems, both trends of IFT data versus pressure have zero real roots. Based on the theory of vanishing interfacial tension (VIT), the pressure root would represent the MMP. The root that is estimated from the data at low pressure conditions (i.e. the first slope) is equal to MCM pressure and the root of the data at high pressure conditions (i.e. the second slope) is equal to FCM. Due to the asphaltene precipitation, the difference between these two parameters becomes larger when the amount of normal paraffins in the solution increases.
- The amount of asphaltene precipitation depends on asphaltene concentration in the solution. By increasing asphaltene concentration until a certain amount, the particles will move toward gas-liquid interface. Presence of particles at the interface disturbs intermolecular forces and increases IFT. Also, dissolving CO_2 in oil causes IFT to decrease. On the whole, these two different factors decrease the IFT. Therefore, presence of asphaltene at interface increases by increasing asphaltene concentration in solutions until a certain amount and it leads to decrease of IFT. However, presence of particle has a negligible effect after surpassing a certain amount of asphaltene concentration.

5. Acknowledgments

We would like to thank Prof. Sh. Ayatollahi and Dr. M. Escorochi, Ms. S. Noorbakhsh, Mr. A. Golkari and Mr. E. Mahdavi for their helps over the course of this study. Special thanks to the core analysis laboratory director, Ms. Sh. Meratian, for helping us with the related lab equipment.

6. References

[1] Andersen, S. I., “Effect of Precipitation Temperature on the Composition of n-Heptane Asphaltene,” Fuel Sci. Tech. Int., 1995, 13, 579.

[2] Mansoori, G.A., Jiang, T.S., Kawanaka, S., 1988. “Asphaltene Deposition and its Role in Petroleum Production and Processing”, Arab. J. Sci. Eng. 13, 17 – 34.

[3] Vasquez, D., Mansoori, G.A., “Identification and Measurement of Petroleum Precipitates”, J. Pet. Sci. Eng. 2000, 26 (1 – 4), 49 – 56.

[4] Sherman, P., “The Flow Properties of Emulsions”, J. Pharm. Pharmacol, 1964, 16, 1 – 25.

[5] Sheu, E.Y., Mullins, O.C. (Eds.), 1995. “Asphaltenes Fundamentals and Applications”, Plenum Press, New York.

[6] Vuong, L.T. "A Simple and Accurate Experimental Technique for Measurement of the Onset of Asphaltene Deposition from Petroleum Reservoir Fluids", MSc Thesis, Chemical Eng. Department, University of Illinois, 1985.

[7] Waxman, M.H., Deeds, C.T., Closmann, P.J., "Thermal Alterations of Asphaltenes in Peace River Tars", Paper SPE 9510 presented at the 1980 SPE Annual Fall Technical Conference and Exhibition, Dallas, Sept. 1980, 21-24.

[8] Swanson, J., "A Contribution to the Physical Chemistry of the Asphalts", J. Phys. Chem, 1942, 46, 141 – 150.

[9] Minssieux, L. "Core Damage from Crude Asphaltene Deposition. Presented at the International Symposium on Oilfield Chemistry", Houston, 18-21 February 1997, SPE-37250-MS.

[10] Galoppini, G., M. Tambini, "Asphaltene Deposition Monitoring and Removal Treatments: An Experience Deep Wells", Soc Pet Eng, 1994, SPE 27622.

[11] Andersen, S. I., Speight, J. G. "Thermodynamic Models for Asphaltene Solubility and Precipitation", J. Pet. Sci. Eng. 1999, 22 (1), 53–66.

[12] Mohammadi, A. H.; Richon, D. "A Mono disperse Thermodynamic Model for Estimating Asphaltene Precipitation", AIChE J. 2007, 53 (11), 2940–2947.

[13] Hirschberg A., deJong, L.N.J., Schipper, B.A., Meijer, J.G., "Influence of Temperature and Pressure on Asphaltene Flocculation" SPE 11202, June 1984.

[14] Burke, K. C., Burke, J. D. Jr., Regier, D. A., "Age at Onset of Selected Mental Disorders in Five Community Populations. Archives of General Psychiatry", 1990, 47, 511 -518.

[15] Clarke, P.F., Pruden, B.B., "Asphaltene Precipitation: Detection using Heat Transfer Analysis, and Inhibition using Chemical Additives", Fuel, 1997, 76(7): 607.

[16] Escobedo, J., Mansoori, G.A., "Viscometric Determination of the Onset of Asphaltene Flocculation: a Novel Method", SPE Prod. Facil, May 1995, 115 – 118.

[17] Malayeri, M. Matourian, R, "Asphaltene in Oil Industry", Setayesh, 2012.

[18] Rao, D.N., "A New Technique of Vanishing interfacial Tension for Miscibility Determination," Fluid Phase Equilibria, 1997, 139, 311-324.

[19] Rao, D.N., Lee, J.I., "Application of the New Vanishing Interfacial Tension Technique to Evaluate Miscibility Conditions for the Terra Nova Offshore Project," Journal of Petroleum Science and Engineering, 2002, 35, 247-262

[20] Rao, D.N., Lee, J.I., "Determination of Gas-Oil Miscibility Conditions by Interfacial Tension Measurements," Journal of Colloid and Interface Science, 2003, 26474-482 ,.

[21] Zolghadr, A., "Determination of Optimum Gas Injection Conditions in EOR Process by Interfacial Tension Investigation", M.Sc. thesis, Shiraz University, Shiraz, Iran, 2011.

[22] Zolghadr, A., Escrochi, M., Ayatollahi, Sh., "Temperature and Composition Effect on CO_2 Miscible Injection by Interfacial Tension Measurement", Journal of Chemical Engineering Data, 2013, 58 (5), 1168-1175.

[23] Escrochi, M., Mehranbod, N., Sh. Ayatollahi, "The Gas–Oil Interfacial Behavior during Gas Injection into an Asphaltenic Oil Reservoir", Journal of Chemical Engineering Data, 2013, 58 (9), 2513-2526.

[24] Nobakht, M., Moghadam, S., Gu, Y., "Mutual Interactions Between Crude Oil and CO_2 Under Different Pressures", Fluid Phase Equilibria, Vol. 2008, 265, 94-103.

[25] Nobakht, M., Moghadam, S., Gu, Y., "Determination of CO_2 Minimum Miscibility Pressure from Measured and Predicted Equilibrium Interfacial Tensions", Industrial and Engineering Chemistry Research, Vol. 2008, 47, 8918-8925.

[26] Wang, X., Zhang, S., Gu, Y., "Four Important Onset Pressures for Mutual Interactions between each of Three Crude Oils and CO_2", J. Chem. Eng. Data, 2010, 55 (10), 4390–4398.

[27] National Institute of Standards and Technology, www.nist.gov, it was available on 6/4/2014.

[28] Tambe, D. E., Sharma, M. M., "The Effect of Colloidal Particles on Fluid–Fluid Interfacial Properties and Emulsion Stability", Adv. Colloid Interface Sci. 1994, 52,1–63., 1847–1853.

[29] Cadena-Nava, R. D., Cosultchi, A., Ruiz-Garcia, J. "Asphaltene Behavior at Interfaces", Energy and Fuels, 2007, 21, 2129–2137.

[30] Hemmati-Sarapardeh, A., Ayatollahi, Sh., Ghazanfari, M., Masihi, M., "Experimental Determination of Interfacial Tension and Miscibility of the CO_2-Crude Oil System; Temperature, Pressure, and Composition Effects", Journal of Chemical Engineering Data, 2014, 59 (1), 61–69.

[31] Jaeger, Ph. T., Eggers, R., "Interfacial Properties at Elevated Pressures in Reservoir Systems Containing Compressed or Supercritical Carbon Dioxide", J. Supercritical Fluids, 2012, 66, 80–85.

Reducing Energy Consumption in Gas Purification Plants (MDEA base) by Retrofit Design

- Omid Sabbagh, Maissam Vahidi Ferdowsi, Mohammad Ali Fanaei
  Department of Chemical Engineering Ferdowsi University of Mashhad, Mashhad, Iran
  (fanaei@um.ac.ir)

Received: Feb 24, 2015/ Revised: Dec 20, 2016 / Accepted: Feb 5, 2017

Abstract

This study evaluates the effect of Structural modifications on energy consumption of gas treatment units of BIDBOLAND refinery (Iran's first gas refinery). To this aim, Aspen HYSYS (V.8.3) software was employed for the unit simulation in rate based method. The results show that as CO_2 content in inlet sour gas is less than 2 percent and MDEA solution is used as solvent, using multiple feeds to the absorption column, static mixers and absorption column sidestream cannot reduce energy consumption level; while using desorption column sidestream and a flash unit can reduce the unit energy consumption up to 10 percent.

Keywords: Aspen HYSYS, Superstructure optimization, MDEA, Energy consumption, Natural gas sweetening.

I. Introduction

Nowadays, one of the most conventional methods of natural gas sweetening is using chemical absorption property of amine solutions which has high energy consumption in spite of various advantages. There are several methods to reduce energy consumption and increase unit capacity. The most important of which are amine type alteration, column internal modification and process flow diagram modification which are known as retrofit design.

Since 1930 when amine solutions were used to remove acid gases in sour gas sweetening process (Figure 1), multiple structures have been proposed for modification and optimization of this process. In 1934, Sholed suggested for the first time a structural modification for early sweetening process optimization [1]. He suggested that a semi-lean stream leaving intermediate stages of the regenerator and its feeding back to the absorption column can reduce energy consumption.

In a simple absorption and desorption process (Figure 1), the absorption liquid circulates as one single stream from the bottom of the absorption column to the desorption column, and from the bottom of the desorption column to the top of the absorption column. There are however possibilities to have multiple feeds or draws in both the absorption column and the desorption column. Such configurations are called split-stream or split-flow configurations. Different alternatives for the split-stream principle are explained in Kohl and Nielsen (1997) and in Polasek et al. (1982) [2, 3]. A survey of process flowsheet modifications for CO_2 removal is given by Cousins et al. (2011) [4]. Energy efficient alternatives are lean amine flash and multiple pressures in the regenerator (Oyenekan and Rochelle, 2006)[5]. Very few calculations of CO_2 removal from exhaust gas based on split-stream have been found in the open literature. A paper by Aroonwilas and Veawab (2006) is one example [6], but the details in the calculations are not shown. Karimi et al. (2010) use the program Unisim [7] and Cousins et al. (2011) using Aspen Plus show process simulations of different split-flow configurations [8]. The main advantage with a split-flow configuration is a reduction in heat consumption in the regenerator. One reason for the reduction in energy consumption is that only a part of the circulating liquid needs to be fully regenerated. Another explanation is that the driving force especially in the absorption column is reduced so that the absorption column normally has higher driving force when using split-flow.

In 2010, based on the work of Vozniuk [9], the traditional gas purification process with and without split-flow has been investigated with using Aspen HYSYS version (V 7.0), and the Kent-Eisenberg amine model. This work was one of the first studies that were focused on split-flow configuration effect quantitatively.

As studies have been so far based on qualitative evaluation of proposed structures, this study has attempted to quantitatively investigate the reduction of gas sweetening unit energy consumption using superstructure optimization. For this investigation, Aspen HYSYS (V 8.3) is used as a process simulator.

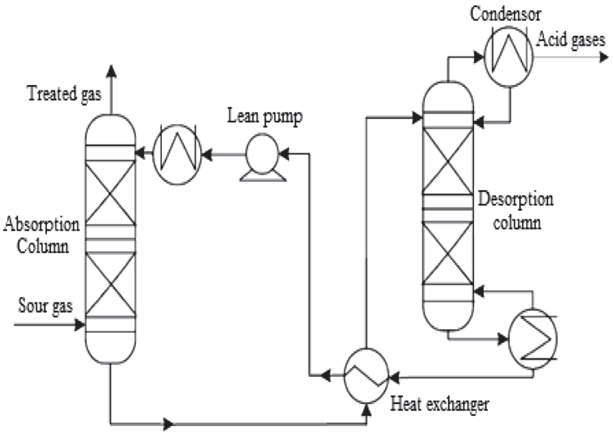

Figure 1.Traditional gas purification process based on amine absorption

II. THE LOGIC OF METHODOLOGY

In this section, the most important alterations in order to optimize sweetening units are summarized briefly.

A. Multiple Feeds to the Absorption Column

In this method, lean amine solution is divided into multiple streams and then enters from different stages into the absorption column. According to the previous research, this makes flat the absorption column's thermal profile and in turn increases the reaction rate of amine with hydrogen sulfide.

B. Split Flow (Absorption Column Sidestream)

In this structure, multiple sidestreams are withdrawn from the absorption column and recycled to the column after cooling. This reduces rich amine rate entering the regenerator column and in turn reduces reboiler and condenser duties.

C. Split Flow (Desorption Column Sidestream)

When the part of the liquid stream withdraws from an intermediate stage of the regenerator column and feeds back to an intermediate stage of the absorption column, on one hand the reboiler and condenser duties will fall down and the other hand this semi-lean solvent is less pure than the ultra-lean stream, and so is less able to absorb acid gases. Because of this, there are trade-offs between the quality of the sweet gas and energy demand.

D. Precontactor (Static mixer)

General structure of this device consists of a pipe with a helix blade inside and fluids are mixed by forced circulation inside this pipe. This device is usually made of materials such as stainless steel and polypropylene. The most important factor encouraging using static mixer is an increase in amine contact time which can increase acid gases absorption like an equilibrium stage.

E. Flash Unit

The absorption column operates at a high pressure, while regenerator takes place close to atmospheric pressure. An intermediate flash unit can exploit this pressure difference to provide an energy efficient method of removing some of the acid gases from the rich solvent stream. Therefore, using this additional structure also provide semi-lean amine which is partly regenerated.

III. Modelling and Validation

In this paper, an industrial life case study (BIDBOLAND gas refinery, Iran) has been used for validation of simulation results. The entire refinery has four parallel gas treatment units (GTU) with 4 absorbers and 4 regenerators. The absorber has an internal diameter of 2.896 meter and two sections. Each section is 6.5373 meters in height and filled with plastic random packing (2-inch Pall rings). The regenerator column has 17 sieve trays and internal diameter of 3.9624 meter. Based on tray spacing of 27 inch, the height of column is 11.6586 m. Table 1 shows the current operation conditions of mentioned units.

The validity of the simulation results depends heavily on selection of equilibrium and process model used in simulation. In this study, the ACID GAS thermodynamic package and ELECNRTL package (PMDEA Data package) are selected for process simulation in Aspen HYSYS (V 8.3) and Aspen Plus (V 8.2), respectively. The simulation results and operating data of the BIDBOLAND treatment unit have been provided in Table 2.

Table 1.Current operation conditions of BIDBOLAND gas refinery units

Absorption Column	
Column Pressure, bar	54
H_2S in Gas Feed, ppm	1950
CO_2 in Gas Feed, mol %	1.74
Gas Feed Temperature, °C	30.0
Amine Conc. in Solvent, wt %	40
Inlet lean Amine Temperature, °C	34
Amine Flow Rate, kmol.h^{-1}	4615
Feed Gas Flow Rate, kmol.h^{-1}	15860
Regenerator Column	
Column Pressure, bar	1.4
Condenser Temperature, °C	33.0
Feed Temperature, °C	93.60
Bottom Temperature, °C	116.70

As seen in Table 2, ACID GAS Package which has been inserted in Aspen HYSYS (V 8.3) software simulated the treatment unit with an acceptable accuracy and therefore used for following investigation steps.

IV. RESULTS AND DISCUSSION

In order to analyze the effect of proposed configurations on energy consumption, simulation results of each structure are evaluated separately.

A. Multiple Feeds to the Absorption Column

According to low CO_2 content in BIDBOLAND refinery feed gas, using this structure not only made help to increase absorption of acid gases, but also reduced amine residence time in the column and so reduced H_2S absorption.

B. Split Flow (Absorption Column Sidestream)

Split flow reduces rich amine entering the regenerator column. But since in this structure, a part of amine solution withdraws from intermediate stages of the column, if the major reactions occur in bottom stages, acid gas absorption will be reduced due to lack of amine.

Since the rate of MDEA solution reaction with CO_2 is slower than H_2S reaction, therefore, more amount of H_2S absorb in bottom stages. According to low CO_2 concentration in BIDBOLAND refinery feed stream, the highest reaction occurs in bottom stages of the column. Thus, using this structure will not be effective.

Table 2.Simulation results of BIDBOLAND GTU using ELECNRTL and ACID GAS packages

Parameters	Plant data	ACID GAS	ELECNRTL
H_2S in Sweet Gas, ppm	4.00	4.02	3.12
CO_2 in Sweet Gas, mole %	1.1065	0.9834	1.4893
Lean Amine Temperature, (°C)	21.20	20.81	20.67
Acid Gas Loading* (Lean amine)	0.328	0.327	0.294
Reboiler Duty, ($Btu.hr^{-1}$)	1.13×10^{8}	1.02×10^{8}	9.94×10^{7}

*moles of acid gases per mole of amine

C. Split Flow (Desorption Column Side stream)

According to energy balance, if the Amine circulation rate is fixed, using the split-flow configuration will reduce energy consumption of the reboiler. On the other hand, in case of a sidestream leaving from upper stages of the regenerator column which has richer amine compared to the lower stages, higher amine circulation rate is needed to consider H_2S limit in the sweet gas stream. And as sidestream leaving from lower levels that has higher potential for gas sweetening in absorption column compared to the former mode, lower amine circulation rate will be required. However, the reboiler duty is more sensitive to amine circulation rate compared to semi-lean side stream stage. Thus, according to the results in Table 3 and Figure 2, a side stream leaving tray 19 of the regenerator with the rate of 2500 kmol/hr leads to minimum energy consumption.

Table 3. Effect of sidestream stage and its flow rate on the energy consumption

Amine Flow (kmol/hr)	Sid stream Rate (kmol/hr)	Stage of Sidestream	Rich Loading	Total Energy (Btu/hr)
2830	2300	18	0.4261	123408093
2627	2300	19	0.4454	121831973
2777	2400	18	0.4335	123576531
2560	2400	19	0.4514	121569940
2762	2500	18	0.4271	123790928
2522	2500	19	0.4481	121484369
2752	2600	18	0.4228	124274162
2477	2600	19	0.4500	121531343
2740	2700	18	0.4215	124924927
2451	2700	19	0.4448	121653625

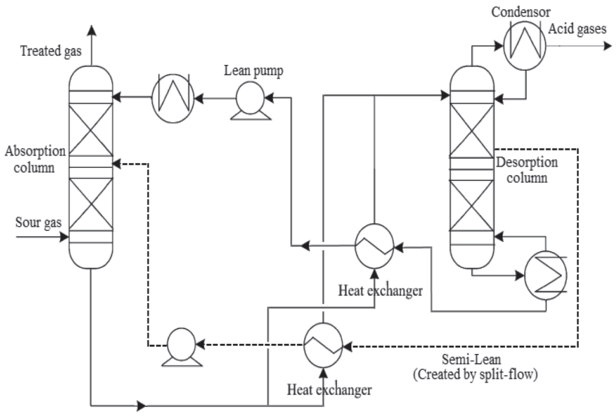

Figure 2.Effect of side stream flow rate leaving stage 19 on the amine circulation rate and energy consumption (H_2S limit: 4 ppm) to split-flow configuration

According to results presented in Table 4, using the Split-Flow configuration (Figure 3) in BIDBOLAND refinery can reduces the energy consumption about 10 million Btu per Hour compared to current configuration.

Table 4.Comparison of unit energy consumption with and without split-flow configuration*

Structure Type	Amine Flow Rate (kmol/hr)	Reboiler Duty (Btu/hr)	Total Energy (Btu/hr)
Current Configuration	4615	112744989	132415338
Split-flow	2522	103574975	121484369

*H_2S limit: 4 ppm

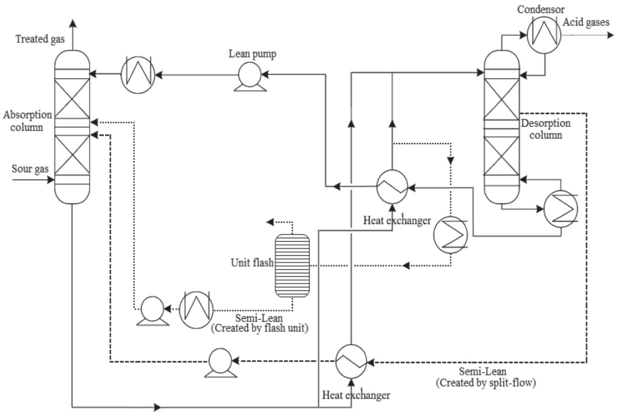

Figure 3.Gas purification process (MDEA base) combined to split-flow configuration

D. Precontactor (Static mixer)

Using static mixer, increases amine contact time and in turn improves absorption of CO_2. However, according to low concentration of CO_2 in BIDBOLAND refinery feed stream, using static mixer is not effective.

E. Flash Unit

Using flash unit for creating semi-lean amine, removed a part of acid gases from rich amine, reduced feed entering the regenerator column and in turn reduced energy consumption of the reboiler. On the other hand, using this unit leads to decreasing of the ultra-lean amine entering the top of the absorption column and in turn reducing absorption of acid gases. These two mutual effects create optimum temperature and stage for feeding semi-lean amine to the contactor column.

In order to remove acid gases from rich amine in flash unit, its temperature had to be increased which was done after pre-heating in lean-rich amine heat exchanger to be according to energy integration principles. In order to increase absorption efficiency, semi-lean amine stream temperature leaving the flash unit was also reduced by an air cooler and according to the sour gas temperature (20°C) and allowed temperature approach (8-15°C) it was set to 28°C to prevent foaming in the column. Entering of semi-lean amine from the top of the column reduces the solvent purity and in turn acid gases absorption rate. At the same time, entering of semi-lean amine from the intermediate stages of the column reduces contact time required for absorption of H_2S. Simulation results of new process(split-flow configuration, flash unit structure, Figure5), according to Table 5 and Figure 4, show that combining these structures increases hydrogen sulfide absorption, reduces corrosion risk and finally reduces energy consumption of the unit. However, it should be noted that with increasing the temperature of the stream entering the flash unit, the rate of make-up water will be increased in this structure compared to the previous structures.

Table 6 shows the effect of combining split-flow configuration with flash unit structure on the energy consumption in comparison to split-

Table 5. Effect of flash unit feed temperature and semi-lean feed stage to absorption column on amine circulation rate and energy consumption*

Semi-lean feed stage	Flash unit feed temperature (°C)	AmineFlow (kmol/hr)	Reboiler Duty (Btu/hr)	Total Energy (Btu/hr)
10	98	2892	100837678	119635106
10	99	2956	100099253	119218708
10	100	3142	100539336	120342903
11	96	2735	100643151	118908196
11	97	2743	99897896	118250324
11	98	2818	99709836	118318888
12	97	2776	100164631	118543610
12	98	2841	99865210	118484552
12	99	2932	99667283	118694581

*semi-lean amine stream is entered to absorption column with 28℃

Table 6.Comparison of unit energy consumption with and without split-flow configuration*

Structure Type	Amine Flow Rate (kmol/hr)	Reboiler Duty (Btu/hr)	Total Energy (Btu/hr)
Split-flow	2522	103574975	121484369
Split-flow Flash unit	2743	99897896	118250324

*H_2S limit: 4 ppm

flow configuration without flash unit. As can be seen, this combination will reduce further the energy consumption.

V. CONCLUSION

A review of gas purification process modifications aimed at lowering the energy consumption by providing semi-lean amine circulation highlighted two options, predominantly applicable in the gas processing industry. These options included the split-flow configuration, using flash unit structure on the way of rich amine stream and some heat integration concepts. The process modifications were assessed using commercially available process simulator software (Aspen HYSYS V8.3). Simulation results showed that using these options instantaneously, reduced energy

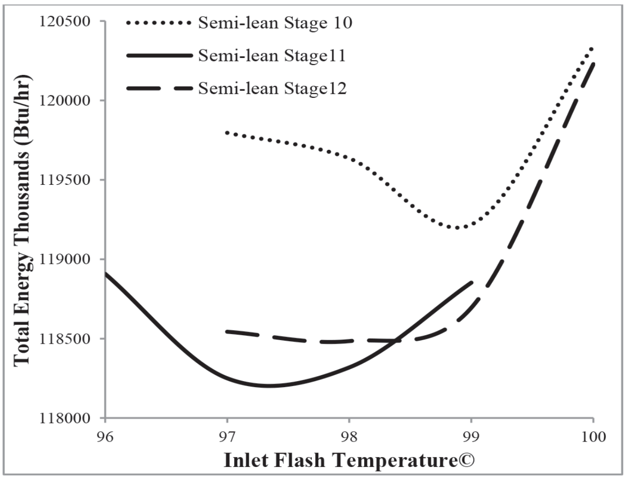

Figure 4. Effect of flash unit feed temperature and semi-lean feed stage to absorption column on energy consumption (semi-lean amine stream is entered to absorption column with 28°C)

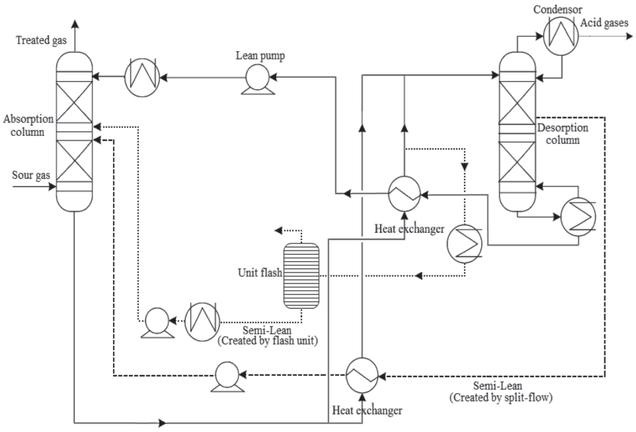

Figure 5.Proposed configuration, split-flow combined to flash unit (gas purification process, MDEA base)

consumption up to 10 percent.

Comparing energy consumption of the regenerator reboiler in the modified process with that in the current state shows that using the modification structures can reduce steam consumption up to 12% which is very important in conditions when steam production should be limited.

Acknowledgment

This project was carried out within the Research stream on optimization studies of BIDBOLAND gas refinery. The authors wish to thanks the refinery research unit officials for their valuable contributions, financial support of this research project and providing all necessary operating information.

References

[1] M. Shoeld, 1934, U.S patent 1,971,798.

[2] A. Kohl, R. Nielsen, Gas purification. Fifth edition, Gulf publishing company, 1997.

[3] J. Polasek, J. A. Bullin, S. T. Donnely, “Alternative flow schemes to reduce capital and operating costs of amine sweetening units,” AIChE Spring National Meeting, 1982.

[4] A. Cousins, L. T. Wardhaugh, P. H. M. Feron, “A survey of process flow sheet modifications for energy efficient CO_2 capture from flue gases using chemical absorption,” International Journal of Greenhouse Gas Control, vol. 4, pp. 1331-1338, 2011.

[5] B. A. Oyenekan, G. T. Rochelle, “Energy Performance of Stripper Configurations for CO_2 Capture by Aqueous Amines,” Industrial & Engineering Chemistry Research, vol. 45, pp. 2457–2464, 2006.

[6] A. Aroonwilas, A. Veawab, “Cost structure and performance of CO_2 capture unit using split-stream cycle,” 8th International Conference on Greenhouse Gas Control Technologies (GHGT-8), Trondheim, Norway, June, 2006.

[7] M. Karimi, M. Hillestad, H. F. Svendsen, “Capital costs and energy considerations of different alternative stripper configurations for post combustion CO_2 capture,” Distillation Absorption Conference, Eindhoven, Netherlands, 12-15 September, 2010.

[8] A. Cousins, L. T. Wardhaugh, P. H. M. Feron, “Preliminary analysis of process flowsheet modifications for energy efficient CO_2 capture from flue gases using chemical absorption,” Journal of Chemical Engineering Research and Design, vol. 89, pp. 1237–1251, 2011.

[9] I. O. Vozniuk, “Aspen HYSYS process simulation and Aspen ICARUS cost estimation of CO_2 removal plant,” MSC. Dissertation, Telemark University College, 2010.

Utilizing Chemical Looping Combustion instead of Fired-Furnace in a Steam Methane Reforming for Enhancement of Hydrogen Production in a Multi Tubular Reactor

- Sedigheh Kabiri and Mohammad Reza Rahimpour

Department of Chemical Engineering, School of Chemical and Petroleum Engineering, Shiraz University, Shiraz 71345, Iran
(sedighehkabiri@yahoo.com & rahimpor@shirazu.ac.ir)

Received: May 18, 2015/ Revised: Apr 1, 2017 / Accepted: May 7, 2017

Abstract

A novel thermally coupled reactor containing steam methane reforming in the endothermic side and chemical looping combustion as an exothermic side has been investigated in this study. In this innovative configuration, huge fired furnace of conventional steam reforming process is substituted by chemical looping combustion in a recuperative coupled reactor. This reactor has three concentric tubes where the steam methane reforming is supposed to occur in the middle tube and the inner and outer tubes are considered to be air and fuel reactors of chemical looping combustion, respectively. Copper is selected as solid oxygen carrier in the chemical looping combustion process. Both oxidation and reduction of Cu in the air and fuel reactor are exothermic and used as heat sources for endothermic steam methane reforming. A steady state heterogeneous model of fixed bed for steam reformer and a moving bed for chemical looping combustion reactor predict the performance of this new configuration. The counter-current mode is investigated and simulation results are compared with corresponding predictions of the conventional steam reformer. The results prove that synthesis gas production is increased in thermally coupled reactor in comparison with conventional steam reformer.

Keywords: Hydrogen production; Steam reforming of methane; Thermally coupled reactor; Chemical looping combustion; Cu- based oxygen carrier.

I. Introduction

Nowadays, there has been an enormous increase in energy demands due to fast growing of industrial development and population of the world. The shortage of fossil fuels as a main energy sources has brought energy crisis. In order to eliminate fossil fuels dependence, comprehensive research has been carried out on searching alternatives energy resources. Hydrogen is an excellent candidate due to its high potential energy.

1.1. Hydrogen

Hydrogen, the most common element in the earth, has been considered as an attractive energy carrier to support energy consumption. Hydrogen is an environmentally friendly, efficient, safe and sustainable energy source (Lokurlu et al., 2003; Heinzel et al., 2002). The products of hydrogen combustion are water and tiny amount of NO_x which can be reduced by proper methods. The use of hydrogen in energy sector enhances the security of energy supply and improves economic competitiveness (Muller-Langer et al., 2007). Except the nuclear fuels, hydrogen has the highest calorific value among fuels. A fuel contains higher proportion of hydrogen provides more energy (Sun et al., 2012). Therefore, pure hydrogen would be the leading fuel which can satisfy the increasing demand asked by many processes such as: methanol, electricity, ammonia, aniline, oil refining, fuel cell, vehicle engines, power plants, etc (F.Brown, 2001; Itoh et al., 2008). In fact, hydrogen is a secondary energy produced from traditional processes like: natural gas reforming, gasification of coal, electrolyses water, biomass gasification, catalytic steam reforming of natural gas, dehydrogenation of cyclic hydrocarbons, etc (Sun et al., 2012). It must be noted that hydrogen production must be low in CO_2 emissions and other pollutants. Among all mentioned technologies, catalytic steam reforming of natural gas is widely used for hydrogen production, 80-85% of the world's total hydrogen production is provided by this method (Simpson and Lutz, 2007).

1.2. Steam reforming

Steam reforming technology is the most commercial method for synthesis gas (CO, H_2) production, the hydrogen cost is less than hydrogen produced by using renewable energy sources or from gasification of solid fossil fuel (Rostrup-Nielsen, 1993; Tugnoli et al., 2008). Steam reforming may involve several catalytic steps: desulfurization of the fuel, steam reforming of methane, a water gas shift reactor and purification of hydrogen using PSA unit .This method is suitable for light hydrocarbons such as natural gas (mainly CH_4), naphtha, liquefied petroleum gas (Ryden and Lyngfelt, 2006). Three main catalytic reactions involved in steam reformer reactor are steam reforming of methane (SRM) and the water-gas shift reaction.

Conventional steam reformer consists of vertical tubes packed with Ni-based catalyst located inside huge furnace. The required heat for endothermic reforming reaction is provided by direct combustion of fuel in the furnace. Therefore, the reformer tubes are under very high thermal stress (F.Brown, 2001). In order to solve this issue, the recuperative coupled reactor has been suggested.

$$CH_4 + H_2O \leftrightarrow CO + 3H_2 \qquad \Delta H^0_{298} = -206.3 kJ/mol \quad (1)$$

$$CH_4 + 2H_2O \leftrightarrow CO_2 + 4H_2 \qquad \Delta H^0_{298} = -164.9 kJ/mol \quad (2)$$

$$CO + H_2O \leftrightarrow CO_2 + H_2 \qquad \Delta H^0_{298} = 41.1 kJ/mol \quad (3)$$

1.3. Coupled reactors

Recently, Coupling exothermic and endothermic reactions are more interested in order to improve the thermal efficiency of process and consequently enhance the production. This type of reactors aims to use energy released by exothermic reaction for proceeding endothermic reaction. In general, the coupled reactors exist into three main classes: direct coupling, recuperative coupling and finally regenerative coupling. At present, recuperative coupling has attracted the most attention of many researchers (Song et al. 2003). Hunter and McGuire (1980) were pioneers in coupling endothermic and exothermic reactions without direct heat transfer. A review on the process intensification for methane steam reforming in a thermally coupled membrane separation technology was studied by Bhat and Sadhukhan (2009). Patel and Sunol (2007) suggested a thermally coupled membrane reactor that is composed of three channels for methane steam reforming. A numerical model for natural gas steam reforming and coupling with a furnace was developed by Ventura and Azevedo (2010). In an interesting idea, Ryden and Lyngfelt (2006) studied steam methane reforming coupled with chemical looping combustion reactor in order to enhance H_2 production with CO_2 capture. In their suggested configuration, reformer tubes are located inside the fuel reactor of chemical looping combustion. A disadvantage of their innovative configuration is erosion of reformer tubes due to harsh environment of the fuel reactor. This issue can be solved by using thermally coupled multitubular reactor which is the main goal of this study.

1.4. Chemical looping combustion

Chemical looping combustion (CLC) is a high-quality candidate which has a good potential to become an efficient technique for separating CO_2. It is easy to produce clean energy from fossil fuel by using this novel method which separates CO_2 inherently (Villa et al., 2003; Hossain and de Lasa, 2008; Zhang et al., 2009). In chemical looping combustion, a gaseous fuel like natural gas or synthesis gas is burnt with oxygen carrier which is usually a metal oxide and used to transfer oxygen from the combustion air to the fuel. Therefore fuel and combustion air never mixed and combustion products (CO_2, H_2O) do not become diluted with N_2; thus pure CO_2 is obtained after condensation of water. The process consists of two separate reactors (a fuel and an air reactor) and solid oxygen carrier transports oxygen between them, see Fig. 1 (Anheden and Svedberg, 1998; Ishida et al., 1987

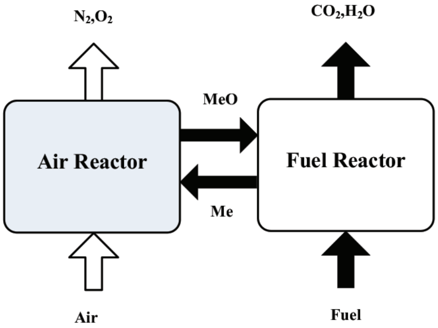

Figure 1. A schematic view of chemical looping combustion

CO_2 and H_2O exit from the fuel reactor while the outlet gas from the air reactor consists of N_2 and unused O_2. The oxygen carrier is reduced with fuel which occurs in the fuel reactor according to:

$$(2n+m)Me_xO_y + C_nH_{2m} \leftrightarrow (2n+m)Me_xO_{y-1} + mH_2O + nCO_2 \qquad (4)$$

Where Me_xO_y is the common abbreviation for metal oxide in chemical looping combustion and Me_xO_{y-1} stands for the reduced oxide which is then circulated to the air reactor and oxidized according to:

$$(2n+m)Me_xO_{y-1} + {}^{1}\!/_{2}O_2 \leftrightarrow (2n+m)Me_xO_y \qquad (5)$$

Reaction (5) is always exothermic while the amount of energy released or required in reaction (4) depended on choice of oxygen carrier. The net energy in the reactor is equal to the amount of heat released from normal combustion. That is apparent because summation of reaction (4) and (5) yields reaction (6); the conventional complete combustion of fuel.

$$C_nH_{2m} + (n + {}^{m}\!/_{2})O_2 \leftrightarrow mH_2O + nCO_2 \qquad (6)$$

The pressure and the temperature of air and fuel reactors are 10^5Pa and 800-1200^{O}C, respectively. Up to now, researchers suggest various designs for chemical looping combustion including: moving bed, fluidized bed, packed bed and dense membrane reactor but circulating fluidized beds is common to use (Nalbandian et al., 2011; Fan et al., 2008; Son and Kim, 2006; Noorman et al., 2007). Richter and Knoche, (1983) proposed the principle of CLC process to increase the thermal efficiency in fossil fuel fired power plants for the first time. Some years later, Lyngfelt and Leckner (1999), successfully ran a 10kW CLC prototype at Chalmers University of Technology. Choice of oxygen carriers is one of the critical steps in CLC and numbers of studies have been done on this course. An appropriate oxygen carrier has the following properties:

1) Have suitable rate of reaction both reduction and oxidation.

2) Be thermodynamically suitable to convert fully the fuel to CO_2 and H_2O.

3) Have good strength so that resistance to attrition and breakage.

4) Does not tend to agglomeration.

5) Be cheap and healthy.

6) Have high melting point.

7) Have low tendency to become deactivate with carbon and sulphur.

Based on above properties, some metal oxides like Ni, Cu, Fe, Mn could be probable oxygen carriers (Cho, 2005; Johansson, 2007; Adanez et al., 2004). In this work, Cu is used as solid particle. An advantage of chemical looping combustion compared with ordinary combustion would be the inherent capture of CO_2 from the rest of the flue gas without spending energy. (Ryden et al., 2009). Also, since indirect combustion in chemical looping combustion does not involve high temperature flame, the formation of NO_x is avoided.

1.5 Literature review

Many efforts have been done for improvement of steam methane reforming. Arab Aboosadi et al. (2011a) have considered a novel integrated thermally coupled configuration for methane steam reforming. In their simulated reactor, hydrogenation of nitrobenzene to aniline in the exothermic side is used as a heat source for endothermic reaction of steam methane reforming. The exothermic reaction takes place in the shell side and endothermic reaction occurs in the tube side. Moreover, Arab Aboosadi et al. (2011b) simulated and optimized tri-reformer (TRM) reactor for producing synthesis gas using differential evolution (DE) method. In TRM process, steam reforming, CO_2 reforming and partial oxidation of methane occurred in a single reactor. Finally, methane steam reforming and hydrogenation of nitrobenzene in hydrogen perm-selective membrane thermally coupled reactor has been optimized using differential evolution (DE) method by Rahimpour et al. (2012). Recently, Rahimpour et al. (2013) have simulated methane steam reforming technology coupled with fluidized bed chemical looping combustion using Fe- based as oxygen carrier. From previous studies, it is found that there is no modeling information available in the literature about using chemical looping combustion as a heat source for steam methane reforming in order to increase H_2 production. Therefore, it was decided to first study on this system.

1.6. Objectives

The main goal of this study is enhancement of hydrogen production theoretically in a thermally coupled steam reformer (TCSR). The endothermic and exothermic reactions are chosen the steam methane reforming and indirect combustion of methane in a chemical looping combustion process, respectively. The motivation is to combine the energy efficient concept of coupling exothermic and endothermic reactions and enhancement of hydrogen production. A steady state 1-D heterogeneous model of the thermally coupled multitubular reactor is used to estimate the performance of the proposed reactor. Ultimately, the simulation results of the TCSR were compared with the ones in conventional steam methane reforming.

2. Process description

2.1. Conventional steam reformer

Fig. 2 represents the schematic diagram of a conventional Lurgi-steam methane reformer (CR) to produce syngas for methanol synthesis process. This reactor has vertical tubes which are located inside a huge fired furnace. Natural gas is mixed with steam and entered to the steam reformer tubes as feed. Vertical tubes is packed with Ni- based catalyst, the generated heat related to natural gas combustion in burners of furnace transfers to reformer tubes (Methanol documents of Lurgi in Assaluyeh-Iran.). Table 1 shows the specification of reactor and operating conditions of the CR

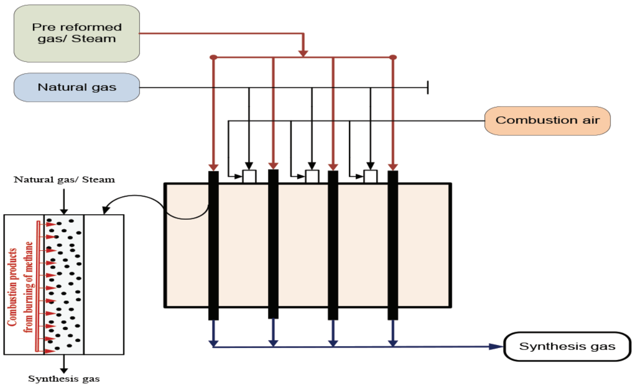

Figure 2. A schematic diagram of conventional steam methane reforming

Table 1: The specification of reactor and operating couditions

Parameter	Value	Unit
Feed composition		mol%
CO_2	1.72	[-]
CO	0.02	[-]
H_2	5.89	[-]
CH_4	32.59	[-]
N_2	1.52	[-]
H_2O	58.26	[-]
Inlet temperature	793	ºK
Inlet pressure	40	bar a
Total feed gas flow	9129.6	Kmol/h
Number of tubes (in 4 rows)	184	[-]
Inside diameter	125	mm
Heated length	12	m
Catalyst volume filled in (total)	27.8	m^3
Design pressure	41	bar g
Design temperature	1063	ºK
Catalyst properties		
Catalyst shape	HOLE 10 rings	
Particle size	19 × 16	mm
Void fraction	0.4	
Heat load on (tube(100% design case	68,730	$Kcal/m^2h$
Reformer duty (100% (design case	248.2	GJ/h
Shell side		
Combustion air		
Temperature	603	ºK
Pressure	1	bar
Flow rate	114,313	sm^3/h
(Feed gas(fuel		
Temperature	307	ºK
Pressure	3	bar
Flow rate	29,608	sm^3/h

2.2. Thermally coupled steam reformer (TCSR)

A conceptual schematic diagram of TCSR is shown in Fig .3. Chemical looping combustion of methane is used as exothermic reaction instead of normal combustion of natural gas in conventional steam reformer. This reactor is consisted of three concentric tubes, the inner tube is used as air reactor of CLC and the outer tube is assumed to be fuel reactor. Endothermic reaction of steam methane reforming takes place on the Ni-based catalyst counter currently in the middle tube. Air fed to the air reactor from the bottom of the reactor and natural gas combined with steam is fed to steam reformer from top of the middle reactor. A small part of steam reformer product stream recycled and combined with CH_4 to use as feed for fuel reactor. Cu as an oxygen carrier enters into air reactor of CLC from top of the reactor, moves down ward and after oxidation exits in the form of CuO from bottom of reactor. Then, copper oxide circulates in a loop and after regeneration transfers to fuel reactor and reduced with CH_4.The specific properties and operational conditions of TCSR are tabulated in Table 2. Table 1 (excluding data in the shell side) is also used for endothermic side of thermally coupled steam reformer.

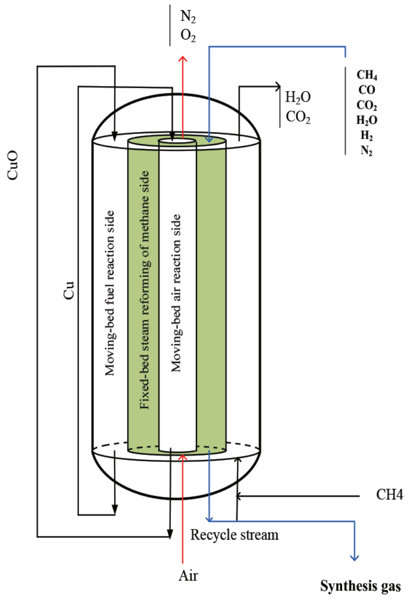

Figure 3. A conceptual schematic diagram of thermally coupled steam reformer

Table 2. The specific properties and operational conditions of TCSR

Parameter	Value
Inlet temperature of endothermic side (*K)	793
Inlet pressure of air reactor (kPa)	101.325
Inlet pressure of fuel reactor (kPa)	101.325
Inner tube or air reactor diameter (m)	0.1
Middle tube or steam reformer diameter (m)	0.1601
Outer tube or fuel reactor diameter (m)	0.1887
Length of the reactor (m)	12
Feed composition	
Air reactor (composition mol %)	
O$_2$	20.94
N$_2$	78.08
Ar	0.98
Oxygen carrier properties (CuO/Al$_2$O$_3$)	
Particle size (mm)*	0.1-0.3

Table 2. Continued...

*Porosity	0.57
*(Apparent density (kg m^{-3}	1800
*(Molar density of CuO (molm^{-3}	80402
*(Molar density of Cu (molm^{-3}	140252
(Flow rate(kg/s	0.01
Obtained from (García-Labiano * (et al., 2004	

3. Reaction scheme and kinetics

3.1. Steam methane reforming (endothermic side)

Three main reaction reactions occurred in steam reformer are steam reforming of methane and the water-gas shift reaction (Equations 1–3). The reaction rates of CR reactions proposed by Xu and Froment are as follows (Xu and Froment, 1989; Xu et al., 2002):

$$R_1 = \frac{k_1}{P_{H_2}^{2.5}}\left(P_{CH_4}P_{H_2O} - \frac{P_{H_2}^3 P_{CO}}{K_I}\right)\times\frac{1}{\varphi^2} \tag{7}$$

$$R_2 = \frac{k_2}{P_{H_2}^{3.5}}\left(P_{CH_4}P_{H_2O}^2 - \frac{P_{H_2}^4 P_{CO_2}}{K_I}\right)\times\frac{1}{\varphi^2} \tag{8}$$

$$R_3 = \frac{k_3}{P_{H_2}}\left(P_{CO}P_{H_2O} - \frac{P_{H_2} P_{CO}}{K_{III}}\right)\times\frac{1}{\varphi^2} \tag{9}$$

$$\varphi = 1 + K_{CO}P_{CO} + K_{H2}P_{H2} + K_{CH_4}P_{CH_4} + K_{H2O}\frac{P_{H2O}}{P_{H2}} \tag{10}$$

The reaction equilibrium constants and Arrhenius kinetic parameters are listed in Table 3. Table 4 shows the Van't Hoff parameters for species adsorption

3.2. Chemical looping combustion (exothermic sides)

In general, metal oxides are used as oxygen carrier in chemical looping combustion. The focus of the literature is on Ni, Cu, Fe and Mn that each one has specific advantage. In this work, Cu is selected as oxygen carrier because reduction of Cu is exothermic while for most other materials, it is endothermic.

Additionally, it is environmentally benign and reactive (Jerndal et al., 2006). The reduction and

Table 3. The reaction equilibrium constants and Arrhenius kinetic parameters for steam reforming reactions

Reaction, j	Equilibrium constant	K_{0j} $\left(\frac{\mathrm{mol}}{\mathrm{kgcats}}\right)$	E_j $\left(\frac{J}{mol}\right)$
1	$K_I = \exp\left(\frac{-26830}{T_s}+30.114\right)(bar^2)$	$1.17\times10^{15}(bar^{0.5})$	240100
2	$K_{II} = K_I \cdot K_{III}(bar^2)$	$2.83\times10^{14}(bar^{0.5})$	243900
3	$K_{III} = \exp(\frac{4400}{T_s} - 4.036)$	$5.43\times10^{5}(bar^{-1})$	67130

Table 4. The Van't Hoff parameters for species adsorption

Components	K_{0i}(bar^{-1})	$\left(\frac{J}{mol}\right)$ ΔHi
CH_4	$10^{-4}\times6.65$	-38280
CO	$10^{-5}\times8.23$	-70650
H_2	$10^{-9}\times6.12$	-82900
H_2O	$10^{5}\times1.77$	88680
$K_{III} = \exp(\frac{4400}{T_s} - 4.036)$		

oxidation reaction of Cu in fuel and air reactor are as follows:

$$2O_2 + 4Cu \rightarrow 4CuO \qquad \Delta H^0_{1073} = -599 kJ/mol \qquad (11)$$

$$4CuO + CH_4 \rightarrow CO_2 + 2H_2O + 4Cu \qquad \Delta H^0_{1073} = -202.5 kJ/mol \qquad (12)$$

One of the main drawbacks of this material is its low melting point (1085ºC). This makes necessary to perform at temperatures lower than its melting point in order to avoid agglomeration and loss of activity (Noorman et al. 2010). In order to describe the kinetics of metal oxide reduction and oxidation, many efforts have been done. In this way, two general types of models can be found in the literature for chemical looping combustion: one is nucleation growth model referred to as Avrami Erofeev models and the other is shrinking core models which are common method (Levenspiel, 1998; Koga and Harrison, 1984). The following equations described the unreacted shrinking core model for gas- solid reactions:

$$\frac{t}{\tau_j} = X_{s,j} \qquad \frac{dX_{s,j}}{dt} = \frac{1}{\tau_j} \qquad \tau_j = \frac{\rho_{m,i} L_i}{b_j k_j C_g^n} \tag{13}$$

Where $\rho_{m,i}$ is the molar density of reactive material in the oxygen carrier, L_i is the layer thickness of reacting solid, b_j is the stoichiometric factor in reaction j (j=oxidation, reduction), k_j is the chemical reaction rate constant in reaction j. The rate of oxidation and reduction can be calculated by following equation:

$$-r_j = \frac{\rho_{m,i}}{b_j} \frac{dX_{s,j}}{dt} \tag{14}$$

In this study, the kinetics data for the reduction and oxidation of CuO/Al_2O_3 with methane and air were used (García-Labiano et al., 2004). Table 5 shows these kinetics parameters for both oxidation and reduction reactions

Table 5. The kinetics parameters of reactions in exothermic side for Cu based oxygen carrier

Kinetic parameters	Fuel reactor	Air reactor
n	0.4	1
E $\left(\frac{kJ}{mol}\right)$	60±3	15±2
$K_0(mol^{-n}m^{3n-2}s^{-1})$	4.5×10^{-4}	4.7×10^{-6}

4. Mathematical model

Fig. 4 shows a schematic diagram for counter-current mode of the heat exchanger reactor configuration. One-dimensional homogenous model including a set of coupled mass and energy balances are taken into consideration. The hypotheses considered in the model of both exothermic and endothermic sides are summarized as follows:

- Steady state condition.
- Gas phase is considered as an ideal.
- Plug flow pattern is assumed.
- Bed porosity in axial and radial direction is constant.
- Heat loss is neglected.
- Axial diffusion of mass and heat are ignored.

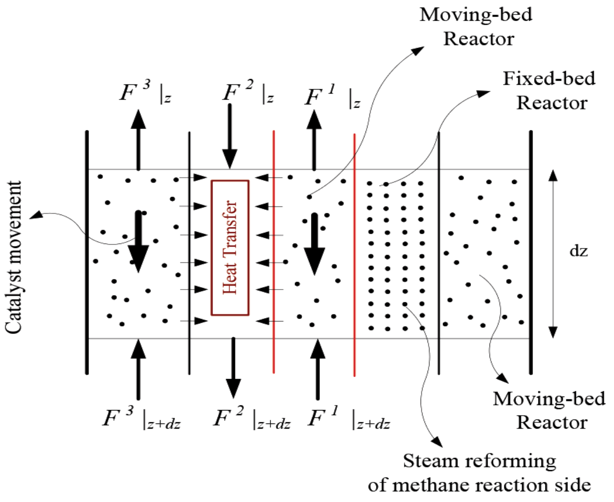

Figure 4. A schematic diagram of counter- current mode for thermally coupled steam reformer (TCSR).

4.1. Packed bed steam methane reformer tube (endothermic side)

Based on the above assumptions and considering the element with length Δz along axial direction, the differential equations describing mole and energy transfers are obtained.

The mass and energy balances for fluid and solid phases are listed in table 6.

Where T_s is temperature of steam reformer side and η is effectiveness factor defined as the ratio of the reaction rate observed on the real rate of reaction.

4.2. Moving bed chemical looping combustion (exothermic side)

There are a few investigations in the modeling of chemical looping combustion reactors. Abad et al. (2010) studied modeling of chemical looping combustion of methane using Cu-based oxygen carrier. Modeling of a 120kw chemical looping combustion reactor using Ni based oxygen carrier was introduced by kolbitch et al. (2009). Kang et al. (2010) investigated the modeling of a counter-current moving bed for fuel and steam reactors in three reactor

Table 6. Mass and energy balance and boundary conditions for solid and fluid phases in packed bed steam methane reformer tube (endothermic side).

Parameter		Value
Mass and energy balance for solid phase	$a_v c k_i^g (y_i^g - y_i^s) + r_i \rho_b = 0$	(15)
	$-\frac{c_p^g}{A}\frac{d(F_t T^g)}{dz} + a_v h_f (T_s^s - T_s^g) - \frac{\pi D_i}{A} U_f (T_s - T_f) - \frac{\pi D_i}{A} U_a (T_s - T_a) = 0$	(16)
	$a_v h_f (T_s^g - T_s^s) + \rho_b \sum_{i=1}^{N} r_i (\Delta H_{fi}) = 0$	(17)
Mass and energy balance for fluid phase	$-\frac{1}{A_a}\frac{d(F_t y_i^g)}{dz} + a_v c k_i^g (y_i^s - y_i^g) = 0$	(18)
Boundary condition	$P_j^g = P_{j0}^g \; y_{i,j}^g = y_{i0,j}^g , \; T_j^g = T_{j0}^g , \; z = 0,$	(19)

chemical looping (TRCL). Their results show that the heat transfer from oxygen carrier to gas phase is fast so that the temperature of gas and solid phases become equal along the reactor. Kang et al., 2012 suggested that a counter-current moving bed is expected to obtain high CO_2 selectivity in comparison with fluidized bed reactor. To obtain mass and energy balances in fuel and air reactor, an element with length Δz was considered. Table 7 shows the equations of mass and energy balances for fluid and solid phases for both air and fuel reactor.

Where C_p^s (J/Kg.K) is the heat capacity of the solids, F^s (kg/s) is the solid loading.

4.3 Auxiliary correlations

In order to complete the mentioned simulation equations, auxiliary correlations containing physical properties of components, mass and heat transfer coefficients should be added, see table 8.

5. Numerical solution

A governing equations of this model consists of a set of differential algebraic equations including mass balances for all sides with given boundary conditions incorporate the reaction rates as well as basic assumptions. In order to solve the set of equations, back-ward finite difference approximation was used. The reactor length is then divided into 100 separate sections and the Gauss-Newton method in MATLAB programming environment was used to solve the non-linear algebraic equations in each section. All parameters of chemical looping combustion reactors like inlet fuel reactor compositions and flow rates are determined by using trial and error method.

6. Results and Discussion

Model validation was carried out by comparing the simulated results of steam reforming side of TCSR with the observed experimental data of the industrial tubular fixed bed steam reformer reactor which is shown in Table 9. According to this table, this simulation results is in good agreement with experimental data. The simulation results of the reactor in the exothermic side are not compared with any reference case .

Table 7. Mass and energy balance and boundary conditions for solid and fluid phases in moving bed chemical looping combustion

Parameter		**Value**
Mass and energy balance for solid phase	$-\frac{1}{A}\frac{d(F^{s}y_{j}^{s})}{dz}+\rho_{b}r_{j}b=0$ $-\frac{cp^{s}}{A}\frac{d(F_{t}^{s}T_{j}^{s})}{dz}+a_{v}h_{f}(T_{j}^{g}-T_{j}^{s})+\rho\sum br_{j}(-\Delta H_{Rxn})=0$	(20) (21)
Mass and energy balance for fluid phase	$\frac{1}{A}\frac{d(F^{g}y_{j}^{g})}{dz}+\rho_{b}r_{j}=0$ $\frac{cp^{g}}{A}\frac{d(F_{t}^{g}T_{j}^{g})}{dz}+a_{v}h_{f}(T_{j}^{s}-T_{j}^{g})+\frac{\pi D_{i}}{A}U(T_{s}^{g}-T_{j}^{g})=0$	(22) (23)
Boundary condition	$z=0;y_{i}^{g}=y_{iout}^{g},y_{i0}^{s}=0,T^{g}=T_{iout}^{g}$	(24)

Table 8. Auxiliary correlations.

Parameter	Equation	Number
component heat capacity	$C_{p}=a+bT+cT^{2}+dT^{3}$	(25)
mixture heat capacity	$C_{p,mix}=\sum_{i=1}^{n}y_{i}\times C_{p,i}$	(26)
viscosity	$\mu=\frac{C_{1}T^{C_{2}}}{1+\frac{C_{3}}{T}+\frac{C_{4}}{T^{2}}}$	(27)
overall heat transfer coefficient	$\frac{1}{U}=\frac{1}{h_{i}}+\frac{A_{i}\ln(D_{o}/D_{i})}{2\pi K_{w}}+\frac{A_{i}}{A_{o}}\frac{1}{h_{o}}$	(28)
heat transfer coefficient between gas phase and reactor wall	$\frac{h}{C_{p}\rho\mu}\left(\frac{C_{p}\mu}{K}\right)^{2/3}=\frac{0.458}{\varepsilon_{B}}\left(\frac{\rho u d_{p}}{\mu}\right)^{-0.407}$	(29)
Pressure drop	$\frac{dP}{dz}=150\frac{(1-\varepsilon)^{2}\mu u_{g}}{\varepsilon^{3}d_{p}^{2}}+1.75\frac{(1-\varepsilon)u_{g}^{2}\rho}{\varepsilon^{3}d_{p}}$	(30)

Table 9. Comparison between model prediction and plant data.

Parameter	Plant	CR
Temperature (°K)	710	720.5
Composition (mol %)	Plant	CR
CO_2	5.71	5.70
CO	3.15	3.18
H_2	31.39	31.45
CH_4	20.41	20.37
N_2	1.29	1.30
H_2O	38.05	38.01
Methane conversion (%)	26.5	26.6

In this section, predicted mole fraction, pressure drop and temperature profiles in the counter current coupled reactor are presented. The results are shown in the following figures. One definition is introduced to examine the methane conversion through the reactor length:

$$\text{Methane conversion} = 100 \times \frac{F_{CH_4,in} - F_{CH_4,out}}{F_{CH_4,in}} \quad (31)$$

6.1.1. Thermal behavior

Fig. 5(a) shows the axial temperature profiles in conventional steam reformer reactor (CR) as well as the endothermic side of thermally coupled steam reformer (TCSR). As seen, the temperature profile of CR is linear while it has a curvy profile in the TCSR. Although the initial temperature of both configurations is the same, the temperature profile of TCSR is higher than that of CR as a result of distribution of solid oxygen carriers in the exothermic side which improves overall heat transfer coefficient. Since the rates of endothermic reactions are increased as temperature increases, hydrogen production is improved in TCSR. In order to make a driving force for heat transfer from exothermic side to endothermic side, the temperature of endothermic side must always lower than that of exothermic side. Fig. 5(b) represents the temperature profile of exothermic side of fuel reactor. In general, the highest temperature in thermally couple reactors is related to exothermic side where heat generation is occurring. Part of generated heat from air and fuel reactors is used for driving endothermic reaction and the rest is used to heat the reaction mixtures in three sides of TCSR. Although steam reforming is an endothermic process, its temperature increased along the reactor; it happens because the generated heat in exothermic side is so higher than consumed heat in endothermic side. The most heat transfer is occurring at the beginning of the reactor because of high temperature difference between endothermic side and exothermic sides. It is understood from Fig. 5(b) that the variation of temperature of fuel reactor is 70 K and the outlet temperature is 1160 K; fortunately, this temperature is lower than melting point of copper so that no agglomeration and loss of activity occur in the chemical looping combustion.

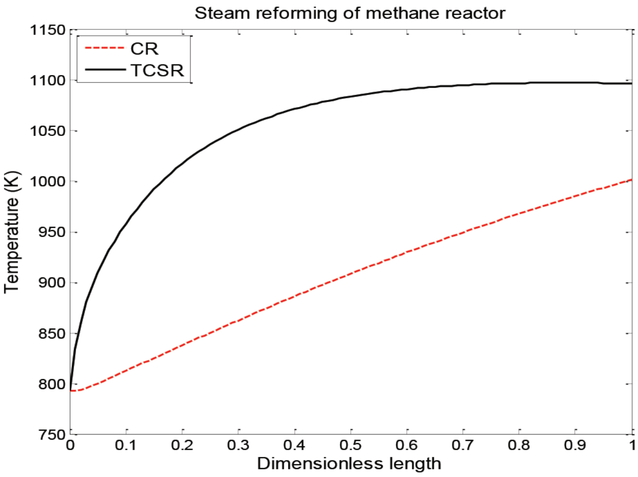

Figure 5(a). Variation of temperature for endothermic side of TCSR and CR.

6.1.2. Molar behavior

The total molar flow rate of endothermic side in CR and TCSR are compared in Fig. 6. The total molar flow rate of TCSR is higher than that of CR. The temperature profile of endothermic side and total molar flow rate have the same trend, because these two parameters are proportional to each other (see fig 5(a)). As total molar flow rate increases, the residence time and conversion decreases.

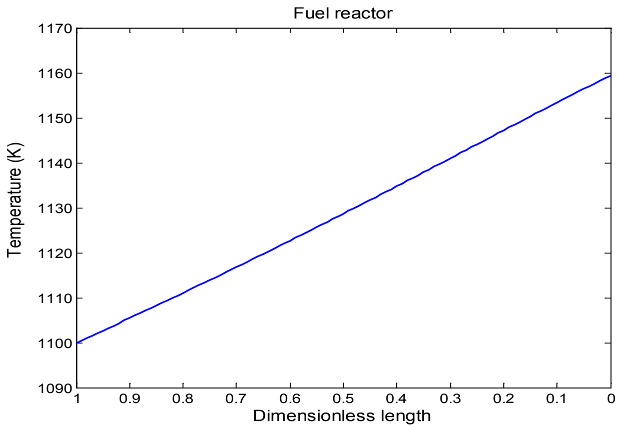

Figure 5(b). Variation of temperature for exothermic side of fuel reactor

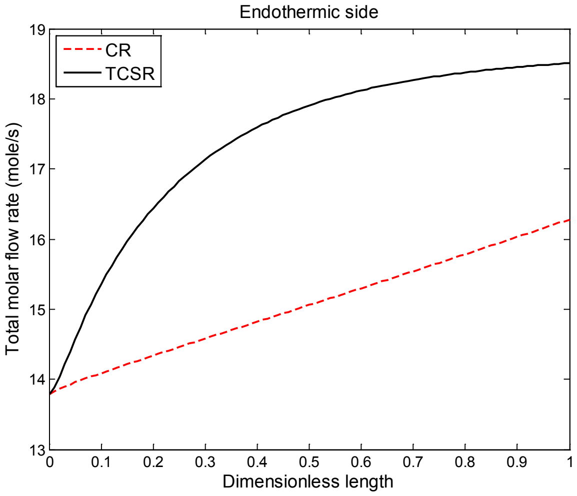

Figure 6. Comparison of total molar flow rate between endothermic sides of TCSR and CR.

Fig.7 (a)-(d) presents the comparison of mole fraction of components in endothermic side of TCSR and CR. Fig.7 (a) and (b) illustrate the mole fraction of hydrogen and carbon monoxide (CO) along the reactor at steady state. Hydrogen and CO are the most desirable products of steam reforming and fortunately their mole fractions increase in the coupled configuration in comparison with CR, because thermal effect of coupled reactor provides a good condition for heat transfer and consequently more production. The CH_4 mole fraction is depicted in Fig. 7 (c). As can be seen, the consumption rate of CH_4 as a main reactant in steam methane reforming process increases in coupled configuration. According to this figure, CH_4 conversion reaches to 52.6 % in TCSR while 26% methane conversion occurs in CR. The difference between CH_4 mole fraction profiles in CR and TCSR is owing to the temperature increase in endothermic side which causes the increase in reaction rate and CH_4 consumption. CO_2 mole fraction as an undesired product in TCSR is compared with the one in CR in Fig.7 (d). At the reactor entrance, the CO_2 mole fraction in TCSR is higher than the one in the CR configuration but at the end of reactor it becomes lower.

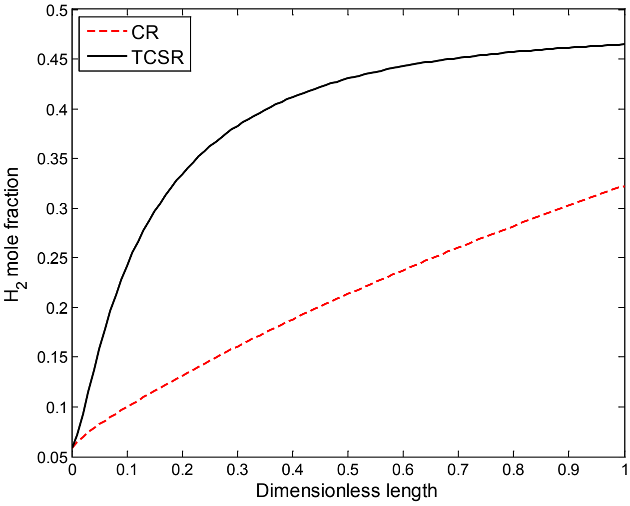

Figure 7(a). Comparison of H_2 mole fraction along the reactor axis between endothermic side of TCSR and CR.

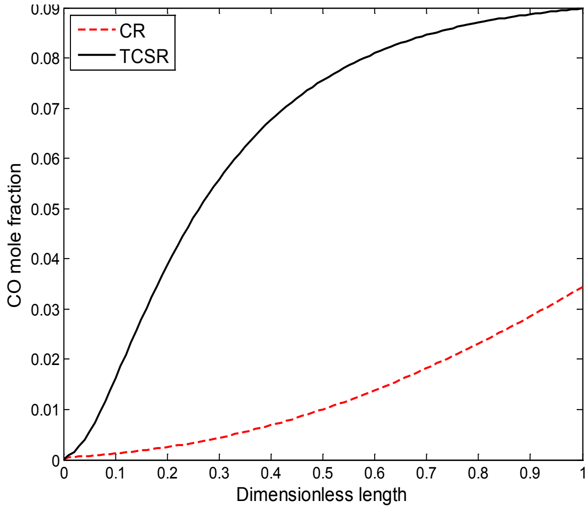

Figure 7(b). Comparison of CO mole fraction along the reactor axis between endothermic side of TCSR and CR.

Fig. 8 (a)-(c) demonstrates the mole fractions of components in exothermic side of fuel reactor. As the reaction scheme in fuel reactor shows, the mole fraction of CH_4, as reactant, decreases linearly along the fuel reactor; it is shown in Fig. 8 (a). H_2O and CO_2 are the main products of reduction reaction in fuel reactor and their mole fraction increases (see Fig 8(b) and (c)) and it can be said that all component behaviors are normal

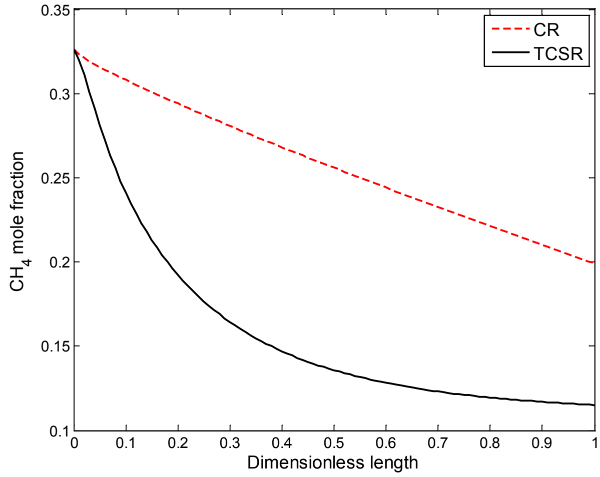

Figure 7(c). Comparison of CH_4 mole fraction along the reactor axis between endothermic side of TCSR and CR.

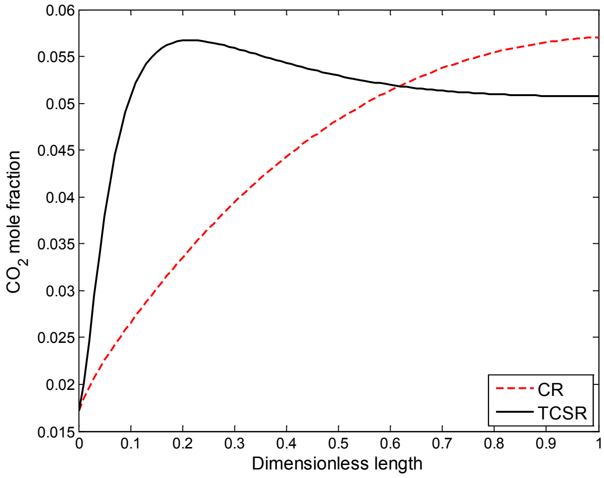

Figure 7(d). Comparison of CO_2 mole fraction along the reactor axis between endothermic side of TCSR and CR.

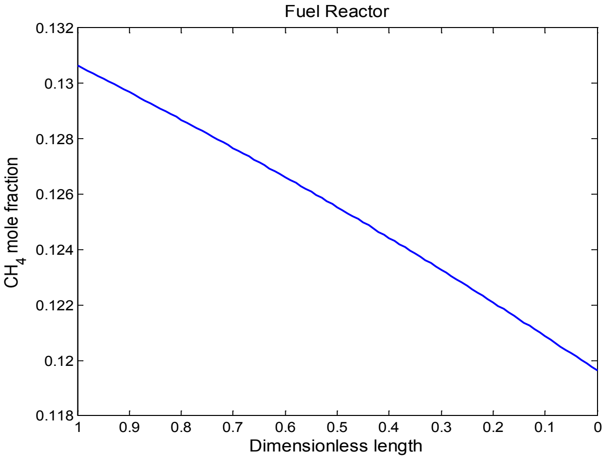

Figure 8(a). Profile of CH_4 mole fraction along the reactor axis in the fuel reactor of exothermic side in TCSR

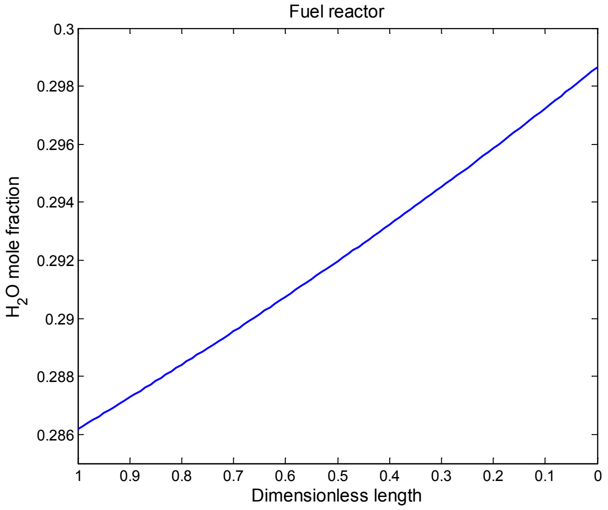

Figure 8(b). Profile of H_2O mole fraction along the reactor axis in the fuel reactor of exothermic side in TCSR

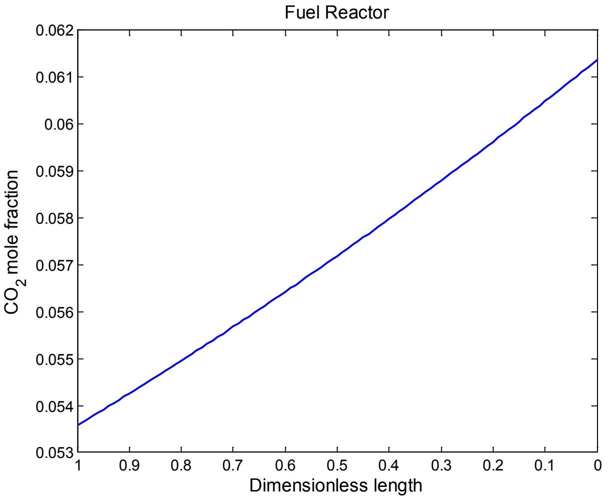

Figure 8(c). Profiles of CO_2 mole fraction along the reactor axis in the fuel reactor of exothermic side in TCSR

6.1.3. Pressure drop

Fig. 9 shows the pressure along steam methane reforming for both conventional and thermally coupled steam reformer. The Ergun Equation (which is equation (23)) usually used to calculate pressure drop through catalytic packed bed.

Since total molar flow rate and temperature profile of thermally coupled steam reformer is higher than temperature profile of conventional steam reformer, the density of gas phase and consequently the velocity and related viscose losses of TCSR become higher. As a result, pressure drop profile through this reactor is higher than conventional steam reformer.

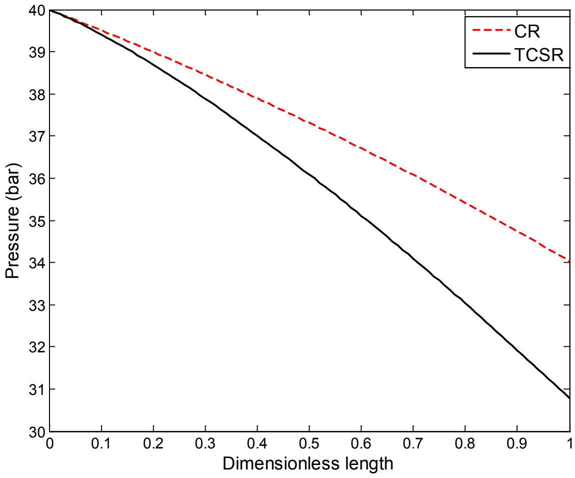

Figure 9. Pressure drop along the endothermic side CR and TCSR.

6.1.4. Influence of Inlet pressure of Methane Steam Reforming

In this section, the reactor performance is investigated for various inlet pressure of the endothermic stream. As it can be seen in Fig 10(a) and (b), by increasing the inlet pressure, the methane conversion and consequently hydrogen mole fraction in the methane steam reforming side decrease due to equilibrium related to steam reforming reactions. Fig 10 (c) shows how total molar flow rate changes with increasing inlet pressure of endothermic side. As seen, total molar flow rate decreases from 19.56 to 17.9 $\frac{mole}{s}$ because of their inverse relationship. Fig 10 (d) illustrates that the pressure drops along the reactor axis increases when the inlet pressure of endothermic stream increases from 30 to 50 bars.

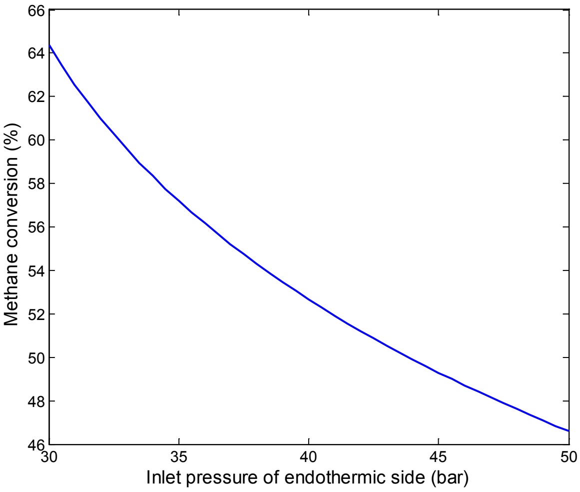

Figure 10(a). Influence of inlet pressure of endothermic stream on methane conversion along the reactor length.

7. Conclusion

Coupling endothermic reaction with an appropriate exothermic reaction improves the thermal efficiency of processes. In this study, a novel thermally coupled steam reformer has been proposed for hydrogen production by using chemical looping combustion as a heat source. Chemical looping combustion is carried out in exothermic side which consists of two moving bed reactor named as air and fuel reactors and supply the necessary heat for endothermic side. Solid metal oxide transfers oxygen between these two reactors. Copper oxide is used in this work because both reduction and oxidation of copper are exothermic.

Steam methane reforming takes place in endothermic side for hydrogen production. Thermally coupled steam reformer consists of three concentric tubes; the inner, middle and outer sides are used for air reactor, steam reformer reactor and fuel reactor, respectively. One dimensional heterogeneous model is used to simulate TCSR and comparison with conventional steam reformer. Thermal and molar behaviors of all sides as well as pressure drop profiles were investigated along the reactors. The results show that an increment about 47% occurs in hydrogen mole fraction in TCSR compared with conventional steam reformer. In addition, the methane conversion in steam reforming reaches to 52.6%. Finally, these preliminary simulation results demonstrate that substitution of huge fired-furnace of conventional steam reformer with chemical looping combustion process is highly efficient for synthesis gas production.

Nomenclature

A_a	Cross section area of each tube (m^2)
av	specific surface area of catalyst pellet (m^2/m^{-3})
b	Stochiometric factor for reaction in CLC
C^g	Gas concentration (mol m^{-3})
cp^g	Specific heat of the gas at constant pressure (j mol^{-1})
cp^s	Heat capacity of oxygen carrier in CLC (j $kg^{-1}k^{-1}$)
Di	Inside diameter of steam reformer (m)
F_t	Total flow rate per each reaction side (mol s^{-1})
K_1	Reaction rate constant for 1st rate equation of steam reforming(mol $kg^{-1}s^{-1}$)
K_2	Reaction rate constant for 2nd rate equation of steam reforming (mol $kg^{-1}s^{-1}$)
K_3	Reaction rate constant for 3rd rate equation of steam reforming (mol $kg^{-1}s^{-1}$)
Kj	Chemical reaction constant of j reaction (j=oxidation, reduction) ($mol^{1-n}m^{3n-2}s^{-1}$)
L_i	Layer thickness of the reacting solid (m)
N	Number of components
n	Reaction order
R_1	First rate of reaction for steam reforming of CH_4 (reaction 4) (mol kg^{-1} s^{-1})
R_2	Second rate of reaction for steam reforming of CH_4(reaction 5) (mol kg^{-1} s^{-1})
R_3	Water gas shift reactor (reaction 6) (mol kg^{-1} s^{-1})
r_j	Rate of reaction occurs in chemical looping combustion based on gas phase (mol m^{-3} s^{-1})
t	Reaction time (s)
T_s	Bulk gas phase temperature related to steam reformer (k)
T_a	Temperature of air reactor (k)
T_f	Temperature of fuel reactor (k)
U_f	Overall heat transfer coefficient between fuel and steam reforming reactors (W $m^{-2}k^{-1}$)
U_a	Overall heat transfer coefficient between air and steam reforming reactors (W $m^{-2}k^{-1}$)
X_s	Solid conversion in the chemical looping reactor

Subscripts

0	Inlet condition
a	Air reactor
f	Fuel reactor
g	Gas phase
i	Chemical species
j	Oxidation, reduction
s	Solid phase

Greek letters

ΔH_{fi}	Enthalpy of formation of component (J mol^{-1})
ΔH_{RXn}	Enthalpy of reaction (J mol^{-1})
p_b	Density of catalyst bed (kg m^{-3})
ρ_{mi}	Molar density of reactive material in the oxygen carrier (mol m^{-3})
η	Effectiveness factor used for the intra particle transport limitation

References

1. Abad, A., Adánez, J., Garcı´a-Labiano, F., F. de Diego, L., Gayán, P., 2010. Modeling of the chemical-looping combustion of methane using a Cu-based oxygen-carrier. Combust Flame. 157, 602-15.
2. Adanez, J., F.de Diego, L., Garcia-Labiano, F., Gayan, P., Abad, A., 2004. Selection of oxygen carriers for chemical looping combustion.

Energy. Fuels. 18, 371-377.

3. (3)Anheden, M., Svedberg, G., 1998. Exergy analysis of chemical looping combustion systems. Energy. Convers. Manage. 39, 1967-1980.
4. Arab Aboosadi, Z., Rahimpour, M.R., Jahanmiri, A., 2011a. A novel integrated thermally coupled configuration for methane-steam reforming and hydrogenation of nitrobenzene to aniline. Int. J. Hydrogen. Energy. 36, 2960-2968.
5. Arab Aboosadi, Z., Jahanmiri, A.H., Rahimpour, M.R., 2011b. Optimization of tri-reformer reactor to produce synthesis gas for methanol production using differential evolution (DE) method. Appl. Energy. 88, 2691-2701.
6. Bhat, S.A., Sadhukhan, J. 2009. Process intensification aspects for steam methane reforming: an overview. AIChE J. 55,408-422.
7. Cho, P., 2005. Development and characterization of oxygen-carrier materials for chemical looping combustion. Doctoral thesis, Chalmers University of Technology, Goteborg, Sweden.
8. Fan, L., Li, F., Ramkumar, S., 2008. Utilization of chemical looping strategy in coal gasification processes. Particuology. 6, 131-142.
9. F. Brown, L., 2001. A comparative study of fuels for on-board hydrogen production for fuel-cell-powered automobiles. Int. J. Hydrogen. Energy. 26, 381-397.
10. García-Labiano, F., F.de Diego, L., Adánez, J., Abad, A., Gayán, P., 2004. Reduction and oxidation kinetics of a copper-based oxygen carrier prepared by impregnation for chemical-looping combustion. Ind. Eng. Chem .Res. 43, 8168-8177.
11. Gosiewski, K., Bartmann, U., Moszczynski, M., Mleczko, L., 1999. Effect of intraparticle transport limitations on temperature profiles and catalytic performance of the reverse-flow reactor for the partial oxidation of methane to synthesis gas. Chem. Eng. Sci. 54, 4589–602.
12. Heinzel, A., Vogel, B., Hubner, P., 2002. Reforming of natural gas-hydrogen generation for small scale stationary fuel cell systems. J. Power. Sources. 105(2), 202-7.
13. Hossain, M.M., L.de Lasa, H., 2008. Chemical looping combustion (CLC) for inherent CO2 separations- a review. Chem. Eng. Sci. 63, 4433-51.
14. Hunter, J.B., McGuire, G., 1980. Method and apparatus for catalytic heat-exchange. US Patent, 4 214 867.
15. Ishida, M., Zheng, D., Akehata, T., 1987. Evaluation of a chemical looping combustion power- generation system by graphic exergy analysis. Energy. 12, 147-154.
16. Itoh, N., Watanabe, S., Kawasoe, K., Sato, T., Tsuji, T., 2008. A membrane reactor for hydrogen storage and transport system using cyclohexane-methycyclohexane mixtures. Desalination. 234, 261-269.
17. Jerndal, E., Mattisson, T., Lyngfelt, A., 2006. Thermal analysis of chemical-looping combustion. Chem. Eng. Res. Des. 84, 795-806.
18. Johansson, M., 2007. Screening of oxygen-carrier particles based on iron-, manganese-, copper-, nickel oxides for use in chemical looping technologies. Doctoral thesis, Chalmers University of Technology, Goteborg, Sweden.
19. Kang K.S., Kim C.H., Bae K.K., Cho W.C., Jeong, S.U., Kim, S.H., Park, C.S., 2012. Modeling a counter-current moving bed for fuel and steam reactors in the TRCL process. Int. J. Hydrogen. Energy. 37, 3251-3260.
20. Kang K.S., Kim C.H., Bae K.K, Cho W.C, Kim S.H, Park C.S., 2010. Oxygen-carrier selection and thermal analysis of the chemical-looping process for hydrogen production. Int. J. Hydrogen. Energy. 35, 12246-54.
21. Koga, Y., Harrison, L.G., 1984. In: Bamford C.H, Tipper C.F.H, Compton R.G. (Eds.), Comprehensive chemical kinetics. Elsevier, Amsterdam. 21, 120.
22. Kolbitsch, P., Pröll, T., Hofbauer, H., 2009. Modeling of a 120 kW chemical looping combustion reactor system using a Ni-based oxygen carrier. Chem. Eng. Sci. 64, 99 –108.
23. Levenspiel, O., 1998. Chemical reaction engineering. John wiley and sons, New York.
24. Lokurlu, A., Grube, T., Hohlein, B., Stolten, D., 2003. Fuel cells for mobile and stationary applications- cost analysis for combined heat and power stations on the basis of fuel cells. Int. J. Hydrogen. Energy. 28(7), 703-11.
25. Lyngfelt, A., Leckner, B., 1999. Technologies for CO_2 separation. In minisymposium on CO_2 capture and storage. Goteborg: Chalmers University of Technology and University of

Gothenburge.

26. Muller-Langer, F., Tzimas, E., Kaltschmidtt, M., Peteves, S., 2007. Techno-economic assessment of hydrogen production processes for the hydrogen economy for the short and medium term. Int. J. Hydrogen. Energy. 32, 3797-810.
27. Nalbandian, L., Evdou, A., Zaspalis, V., 2011. La1-x Srx MyFe1-yO3-s perovskites as oxygen-carrier materials for chemical-looping reforming. Int. J. Hydrogen. Energy. 36, 6657-6670.
28. Noorman, S., van Sint Annaland, M., Kuipers, H, 2007. Packed bed reactor technology for chemical-looping combustion. Ind. Eng. Chem. Res. 46, 4212-4220.
29. Noorman, S., van Sint Annaland, M., Kuipers, J.A.M., 2010. Experimental validation of paced bed chemical-looping combustion. Chem. Eng. Sci. 65, 92-97.
30. Patel, K.S., Sunol, A.K., 2007. Modeling and simulation of methane steam reforming in a thermally coupled membrane reactor. Int. J. Hydrogen. Energy.32, 2344-58.
31. Rahimpour, M.R., Arab Aboosadi, Z., Jahanmiri, A.H., 2012. Differential evolution (DE) strategy for optimization of methane steam reforming and hydrogenation of nitrobenzene in a hydrogen perm-selective membrane thermally coupled reactor. Int. J. Energy. Res. DOI: 10.1002/er.2887.
32. rahimpour, m.r., hesami, m., saidi, m., jahanmiri a., farniaei m., abbasi m., 2013. methane steam reforming thermally coupled with fuel combustion: application of chemical looping concept as a novel technology. energy & fuel. 27, 2351-2362.
33. Richter, H.J., Knoche, K.F., 1983. Reversibility of combustion process. In: Gaggioli R.A, editor. Efficiency and costing, second law analysis of process. ACS Symposium Series. Washington DC. pp.71-85
34. Rostrup-Nielsen J.R., 1993. Production of synthesis gas. Catal. Today. 18,305-324.
35. Ryden, M., Cleverstam, E., Lyngfelt, A., Mattisson, T., 2009. Waste products from the steel industry with NiO as additive as oxygen carrier for chemical looping combustion. Int. J. Greenhouse. Gas. Control. 3, 693-703.
36. Ryden, M., Lyngfelt, A., 2006. Using steam reforming to produce hydrogen with carbon dioxide capture by chemical-looping combustion. Int. J. Hydrogen. Energy. 31, 1271-1283.
37. Ryden, M., Lyngfelt, A., Mattisson, T., 2006. Two novel approaches for hydrogen production; chemical-looping reforming and steam reforming with carbon dioxide capture by chemical looping combustion. WHEC. 16, 13-16.
38. Simpson, A.P., Lutz A.E., 2007. Exergy analysis of hydrogen production via steam methane reforming. Int. J. Hydrogen. Energy. 32, 4811-20.
39. Song, K.S., Seo Y.S., Yoon, H.Y., Cho, S.J., 2003. Characteristics of the NiO/Hexaaluminate for chemical looping combustion. Korean. J. Chem. Eng. 20, 471-5.
40. Son, S.R., Kim, S.D., 2006. Chemical looping combustion with NiO and Fe_2O_3 in a thermo balance and circulating fluidized bed reactor with double loops. Ind. Eng. Chem. Res. 45(8), 2689-2696.
41. Sun, Z., Liu, F., Lin, X., Sun, B., Sun, D., 2012. Research and development of hydrogen fueled engines in china. Int. J. Hydrogen. Energy. 37, 664-681.
42. Tugnoli, A., Landucci, G., Cozzani, V., 2008. Sustainability assessment of hydrogen production by steam reforming. Int. J. Hydrogen. Energy. 33, 4345-57.
43. Villa, R., Cristiani, C., Groppi, G., Lietti, L., Forzatti, P., Cornaro, U., Rossini, S., 2003. Ni based mixed oxide materials for CH4 oxidation under redox cycle conditions. J. Mol. Catal. A: Chem. 204-205, 637–646.
44. Ventura, C., Azevedo, J.L.T. 2010. Development of a numerical model for natural gas steam reforming and coupling with a furnace model. Int. J. Hydrogen. Energy. 35,9776-87.
45. Xu, G., Li, P., Rodrigues, A., 2002. Sorption enhanced reaction process with reactive regeneration. Chem. Eng. Sci. 57, 3893-908.
46. Xu, J., Froment, G., 1989. Methane steam reforming, methanation and water gas shift: I. Intrinsic kinetics. AIChE. J. 35, 88-96.
47. Zhang, X., Han, W., Hong, H., Jin, H., 2009. A chemical intercooling gas turbine cycle with chemical-looping combustion. Energy. 34, 2131-2136.

A New Method to Enhance Separation of Acid Gas from Natural Gas by Mixed Amine Solution

- Abolfazl Gharibi Kharaji and Vahid Madadi Avergani*
  Chemical Engineering, Isfahan University, Isfahan, Iran
- Parviz Darvishi
  Chemical Engineering, Yasouj University, Yasouj, Iran
  *(Corresponding author Email: vmadadi64@eng.ui.ac.ir)

Received: May 1, 2017/ Accepted: May 29, 2017

Abstract

Application of mixed amine solution in gas sweetening unit decreases the operation cost and corrosion rate. Also it increases the amount of sulfur in acid gas stream that exits from sweetening and enters to sulfur recovery units. Gas sweetening unit of Bidboland gas refinery (BGR) was simulated by Hysys software. Simulation of BGR had good agreement with industrial data. The parameters such as CS (carbon dioxide in sweet gas), SSRU (the amount of H2S in outlet acid gas stream from stripper to sulfur recovery unit), RAL (rich amine loading) and HPA (reboiler duty per amine circulation rate), were compared for ten blends of DEA (Diethanolamine) and MDEA (Methyl Diethanolamine). According to technical specified parameters, mixed amine with composition of 40 wt. % MDEA and 10 wt. % DEA identified as a good amine blend for gas sweetening unit in BGR. JOGPT. Because Photonics is produced in DOC, strict adherence to format

Keywords: Gas Sweetening, Bidboland Gas Refinery, Hysys, Mixed Amine, Hydrogen Sulfide

1. Introduction

Natural gas is the most important source after fuel gas because of its clean combustion and reduction of the atmosphere pollution. Natural gas contains impurities such as carbon dioxide, hydrogen sulfide and sometimes traces of Carbonyl sulfide, carbon disulfide and mercaptans.

MDEA selectively removes H_2S from natural gas streams while piperazine acts mainly as a corrosion inhibitor and surfactant. A corrosion inhibitor is a chemical compound which added in small concentration stops or slows down corrosion of metals and alloys. The slower rate of reaction of CO_2 with MDEA is compensated through the addition of small amounts of rate-promoting agents such as DEA or piperazine [1]. So blends of activating primary or secondary amines (such as DEA) can be improved with tertiary amines (such as MDEA) for the removal of carbon dioxide from natural gas [2]. MDEA is a compound that used in oil refinery industry to absorb and strip hydrogen sulfide and carbon dioxide. Due to technological or human malfunctions, MDEA may be found in process waters and afterwards transported to the wastewater treatment plant [3].

Several chemical solvents are available for gas sweetening processes, almost being based on alkanolamine products. Sour gas purifying facilities use the process of chemical absorption by alkanolamines to remove hydrogen sulfide and carbon dioxide from raw natural gas. Hydrogen sulfide must be removed from the gas before using due to its highly corrosively and toxicity. Aqueous solutions of alkanolamines absorb acid gas at lower temperatures and release the acid gases at higher temperatures. This process allows the separation of carbon dioxide and hydrogen sulfide from natural gases.[4] The main alkanolamine products used in the gas sweetening industries are Mononethanolamine (MEA), Diglycolamine (DGA), Diethanolamine (DEA) and Methyl Diethanolamine (MDEA). Advantages and disadvantages for amine types are mentioned in Table 1.

Table 1: Advantages and Disadvantages for Amine Solutions[5, 6]

Advantage	Disadvantage	Amine Type
• Non selective removal • Degrading by mercaptans • High vapor pressure • Needs reclaimer	• Rapidly reaction with acid gases • Largest carrying capacity for acid gases • Separates easily from acid gas • Less circulation rate	Primary Amine
• Less reactive than primary amine • Non selective removal	• Low degrading by mercaptans • High Chemically stable • Low vapor pressure	Secondary Amine
• Less reactive with acid gas • Low absorbing for CO_2	• Selective removal for H_2S • Highly stable • Use with high concentration • Energy saving	Tertiary mine

Recently attention has been focused on using amine blends for gas sweetening due to compensating single amine solution problems. A promising blend has a high capability for loading capacity, high reaction rate, low operating cost, low corrosive tendencies and high resistance to degradation [7]. MDEA is one component that used for the absorption and stripping of hydrogen sulfide and carbon dioxide, as well as and the removal of carbonyl sulfide (CS) from natural gas in natural gas sweetening processes [8, 9].

Compared to the most common alkanolamines, the tertiary amine (MDEA) is known for its lower regeneration cost, its thermal and chemical degradation resistance and lower corrosion rate. In addition, it has capability for selective H_2S removal in the presence of CO_2 and removal of both H_2S and CO_2 simultanously [10]. Glasscock et.al showed that MDEA interfere in DEA kinetics, in other hand increase DEA rate of reaction with addition MDEA [11]. Carbamate ions ($R_2NH^+COO^-$) produced during CO_2 absorptions with primary and secondary amines. While CO_2 absorptions with tertiary amines were accompanied with formation of carbonate and bicarbonate. Since reaction heat of carbamate is higher than carbonate, energy cost of primary and secondary amines expected higher than tertiary amines [12, 13] .

In this study, the effect of mixed amine concentrations were investigated on CO_2 mole fraction of sweet gas (CS), H_2S mole fraction of acid gas stream (SSRU), rich amine loading (RAL) and reboiler duty per amine circulation rate (HPA). RAL is summation of acid gas moles (CO_2+ H_2S) per amine moles and it's dimensionless. In order to define parameters, the best blend of amines was selected.

2. Simulation Description

2.1. Bidboland Gas Refinery (BGR)

Bidboland Gas refinery (BGR) which located in Khuzestan, state of I.R. Iran, is the first gas refinery in Middle East. Sour gas as a feed comes from Aghajari field & Asaluyeh region (Pars Special Energy Economic Zone) with the rate of 240 MMSCFD and maximum of 2.85% acid gas (Bidboland site). Sour gas was treated by four units and reach to pipeline specifications (i.e. less than 4ppm for H_2S). A portion of sweet gas will be sent to IGAT I (Iranian gas transmission pipeline I) and another part goes to NGL (Natural Gas Liquids) plants. For sweetening gas need to be passed through an amine solution. Amine solution at BGR firstly was MEA and after a while due to MEA degradation and high steam consuming need to be regenerated , DEA was replaced and recently sour gas replaced by activated MDEA for a unit.

2.2. Gas sweetening unit

Sour gas that contains CO_2 and H_2S firstly enters scrubber to remove its free liquids, solid materials and any contaminations. The gas from scrubber enters the bottom of absorber and flows upward through column with counter-current contact with aqueous amine solution (Lean Amine) that comes from top of absorber. Chemical reactions between amine and acid gas occurs and amine solution absorbs the acid gas according to the following equations to [6, 14];

(1) $H_2S + R_2NH \rightleftharpoons R_2NH_2^+ + HS^-$

(2) $CO_2 + 2R_2NH \rightleftharpoons R_2NH_2^+ + R_2NCOO^-$

(3) $CO_2 + H_2O \rightleftharpoons H_2CO_3$

(4) $H_2CO_3 + R_2NH \rightleftharpoons R_2NH_2^+ + CO_3H^-$

Reaction is exothermic so the gas temperature increases and sweet gas leaves the top of absorber column and the amine solution with acid gases (Rich Amine) leaves the bottom of the absorber. Absorber in the BGR is packed column with 30 and 3 meters height and diameter respectively, and operates at pressure of 45-60 kg/cm^2. Temperature of lean amine solution is 5-10°C higher than sour gas temperature to prevent forming condensate in absorber column. To regenerate and recycling amine solution, temperature of rich amine must be increased and pressure will be decreased.

In flash drum with suppressing amine pressure to 3-4 kg/cm^2 a part of acid gas removes from rich amine solution and then rich amine passes through tube side of amine/amine heat-exchanger. The rich solution is heated

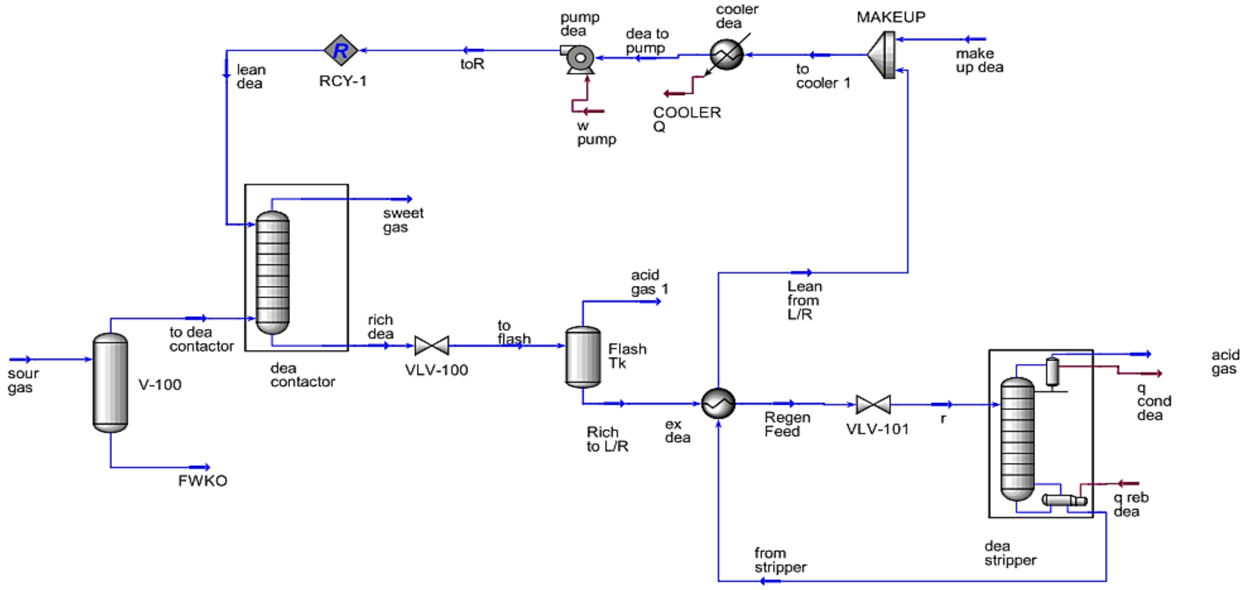

Figure 1: PFD of simulated gas sweetening unit

by regenerated solution (Lean amine) which comes from bottom of regenerator column, so rich amine enters. The regenerator column with 25 and 4 meters for height and diameter respectively which operate at the pressure of 0.4 kg/cm^2 with 19 trays. In regenerator column, rich amine became free from acid gas by heat it up. Temperature of reboiler maintain between 110-116°C by steam flow.

The lean amine drains from bottom of regenerator and release heats at amine/amine heat-exchanger drain and will mix with makes up of water and DEA in order to maintain amine concentration constant and their pressure will increase by pumps and finally will enter to the tops of absorber column. Figure 1 indicates simulated process flow diagram for gas sweetening by DEA solution.

Simulation of gas sweetening unit was performed by Hysys software that equipped with Amine package. Figure 1 indicates process flow diagram for sweetening. First of all, the sour gas was saturated by water stream and then sent to scrubber. The required information for running the program was used by Bidboland data. Flow for makes up was obtained by performing mass balance around the sweetening unit.

3. Results and Discussions

Table 2 clearly showed that results for simulation were compatible with industrial data and had a good agreement with less than 2% relative error. Relative error was calculated by given Equation. Results also showed that H_2S reached to pipeline specification with concentration of 2.1 ppm.

$$Relative\ Error = \frac{|Real\ data - Simulated\ data|}{Real\ data} \quad (5)$$

By comparison of simulation and industrial data, it can be concluded that simulation results were valid, so blends of MDEA and DEA with different mass fractions were used. Results show, while amine concentration increased, energy consumption decreased (discuss later); so the maximum possible mixed amine concentration was used. Typical concentration range for DEA and MDEA are 25-35% and 30-50% by weight in the aqueous solution, respectively [6, 14]. Table 3 shows the high concentration mixed amine solutions that satisfy amine concentration

Table 2: Composition of major components in sour and sweet gas and relative errors with industrial data

Components	Mole fraction of Sour gas in industrial	Mole fraction of Sweet gas in industrial	Mole fraction of Sweet gas in simulation	Relative Error
CO_2	2.17E-02	4.20E-03	4.24E-03	9.64E-03
H_2S	3.30E-03	2.10E-06	2.11E-06	3.54E-03
Methane	8.62E-01	8.81E-01	8.80E-01	1.07E-03
Ethane	6.17E-02	6.29E-02	6.30E-02	1.90E-03
Propane	1.25E-02	1.27E-02	1.27E-02	1.08E-03
i-Butane	1.24E-03	1.25E-03	1.27E-03	1.40E-02
n-Butane	1.78E-03	1.78E-03	1.82E-03	2.22E-02
n-C_4+	3.58E-02	3.62E-02	3.70E-02	2.21E-02

ranges.

The effect of mixed amine concentrations were investigated on CO_2 mole fraction of sweet gas (CS), H_2S mole fraction of acid gas stream (SSRU), amount of energy consumed per amine circulation rate (HPA) and rich amine loading (RAL) which is significant index for corrosion in unit .

Table 3: Different mixed amines that used in simulation

Total mixed amine used in 50 wt. %	Total mixed amine used in 40 wt. %
40% MDEA, 10% DEA	30% MDEA, 10% DEA
35% MDEA, 15% DEA	25% MDEA, 15% DEA
30% MDEA, 20% DEA	20% MDEA, 20% DEA
25% MDEA, 25% DEA	15% MDEA, 25% DEA
20% MDEA, 30% DEA	10% MDEA, 30% DEA
50% MDEA	40% MDEA

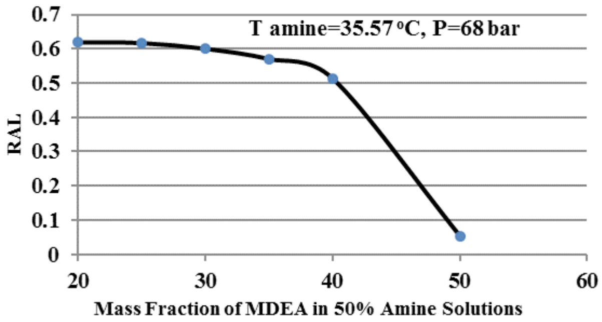

Figure 2: The effect of MDEA concentration on RAL for 50% wt. amine solution

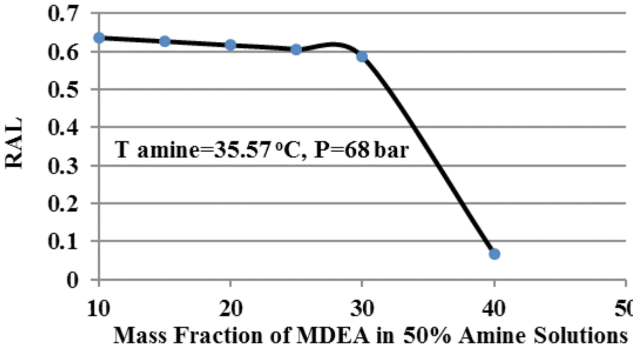

Figure 3: The effect of MDEA concentration on RAL for 40% wt. amine solution

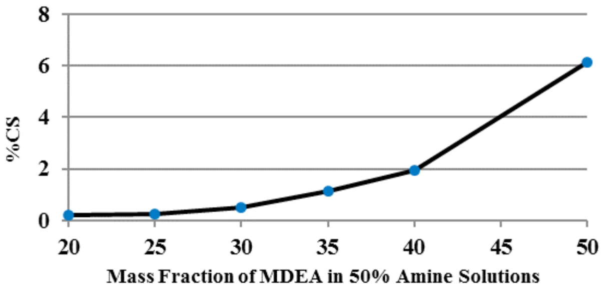

Figure 4: The effect of MDEA concentration on CS for 40% wt. amine solution

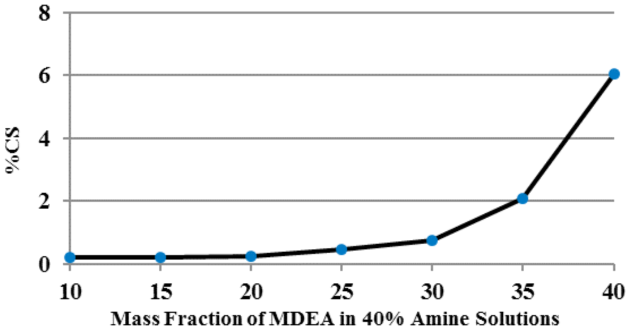

Figure 5: The effect of MDEA concentration on CS for 40% wt. amine solution

The effect of MDEA concentration on rich amine loading, RAL, was shown in figure 2 and 3. Results showed that by increasing in MDEA concentration in two 40 and 50% mixed amine solutions, the amount of RAL decreases.

The results also indicated SSRU and CS parameters were decreased with increase of DEA in amine solution (figure 4 to 7). That behaviors caused from selective removal of H_2S by MDEA, so mass fraction of MDEA was increasable while amount of CS not passing from allowance. With adds up DEA in MDEA solution, order of CS gone down and CS approached to the industrial data. Increase of DEA in MDEA solution greater than 10% wt. had no obvious change in CS parameter, so solution of 10% wt. DEA and 40% wt. MDEA was selected as the best amine blend.

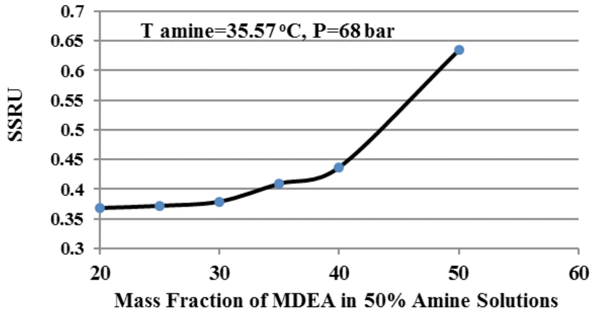

Figure 6: The effect of MDEA concentration on CS for 40% wt. amine solution

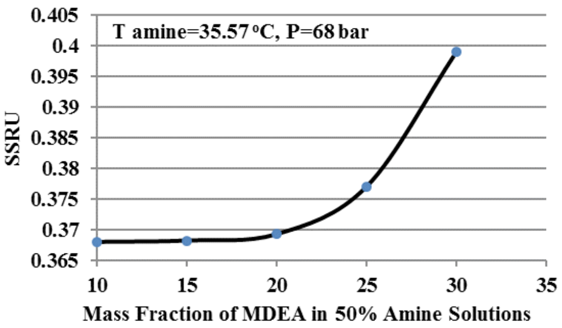

Figure 7: The effect of MDEA concentration on CS for 40% wt. amine solution

HPA parameter was compared for 40 and 50% wt. amine solutions; it was found that HPA for 40% wt. at any blends were greater than 50% wt. with same DEA concentration and amine flow circulation rate. As further work 40% wt. amine solutions were eliminated and results were analyzed for 50% wt. amine solutions. It

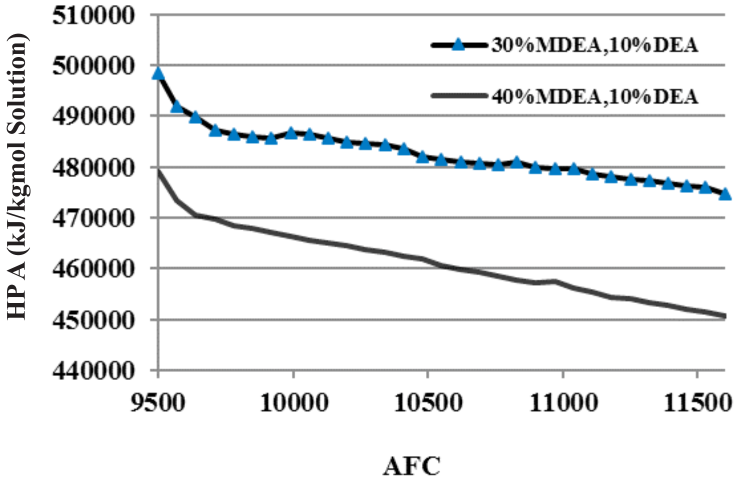

Figure 8: The effect of Amine Flow Circulation on HPA

is necessary to say that HPA represented factor of process economic, unit will be inefficiently while HPA became greater. The figure 8 shows these results. HPA parameter was investigated for mixed amine solution (10% wt. DEA, 40% wt. MDEA) and DEA solution, according to results, for any amine flow rate (AFC) HPA of blend amine was lower than industrial condition (DEA solution). HPA expressed energy consumption in gas sweetening unit and with decrease in HPA process became more economically.

As the results shown in figure 8, in each flow circulation rate, the magnitude of HPA for 50% wt. mixed amine solution is less than 40% wt. Therefore 50% wt. mixed amine by 10% wt. DEA is the best belnd solution for gas sweetening unit in BGR.

Major parameters for real and amine blend solutions were compared in Table 4. Results reveals that replacing of mixed amine with DEA solution, the operation of gas sweetening unit will improve. Investigating of adding MDEA to DEA solution showed that SSRU, RAL and HPA were improved. Expressed parameters had positive effect on SRU efficiency, amount of corrosion and operation costs respectively. While increase of MDEA have no significant effect on CS and SS and sweet gas specifications satisfied allowance, so it can be concluded that mixed amine increased amount of sulfur to SRU and reduced corrosion and operation costs. According to figure 8 and Table 4, blend of 40% MDEA-10% DEA was recommended to BGR to improve the performance of unit.

4. Conclusion

When large amounts of CO_2 are being passed through to the sweet gas at relatively low

Table 4: Comparison of industrial data against offered mixed amine solution

Amine solution	SSRU	CS	RAL	HPA (MJ/m^3)
Real solution	0.157118	4.24E-03	0.470629	217.3832
40% wt. MDEA, 10% wt. DEA	0.160447	4.79E-03	0.257535	146.2427

pressures, it becomes difficult for MDEA to reach pipeline specification for H_2S if the inlet gas contains more than about 1000 ppm H_2S. At these lower pressures, the addition of a more reactive amine clearly enhances the solution ability to remove CO_2. Thus, in situation where MDEA cannot meet the residual gas requirements, the use of amine mixtures can be usually improved the plant performance. At this study, the effect of mixed amine concentrations were studied on CS, SSRU, RAL and HPA parameters in a gas sweetening unit of BGR. According to defined parameters, 40% MDEA-10% DEA such as best blend of amines was selected to reach high amount of SSRU, low RAL and HPA parameters in unit. So this blend was recommended to BGR due to approach the conditions to optimum values in terms of energy consuming, corrosion amount in unit and SRU efficiency.

References

[1] Kohl ALRFC. Gas purification. Houston: Gulf Pub. Co., Book Division; 1985.

[2] Schubert S, Grünewald M, Agar D. Enhancement of carbon dioxide absorption into aqueous methyldiethanolamine using immobilised activators. Chemical engineering science. 2001; 56(21): 6211-6.

[3] Bord N, Crétier G, Rocca JL, Bailly C, Souchez JP. Determination of diethanolamine or methyldiethanolamine in high ammonium concentration matrices by capillary electrophoresis with indirect UV detection: application to the analysis of refinery process waters. Analytical and Bioanalytical Chemistry. 2004; 380(2): 325- 32.

[4] Fürhacker M, Pressl A, Allabashi R. Aerobic biodegradability of methyldiethanolamine (MDEA) used in natural gas sweetening plants in batch tests and continuous flow experiments. Chemosphere. 2003; 52 (10): 1743-8.

[5] Campbell JMMRN. Gas conditioning and processing. Norman, Okla.: Campbell Petroleum Series; 1992.

[6] Gas Processors Association GPSA. Engineering data book : FPS version. Tulsa, Okla. (6526 E. 60th St., Tulsa 74145): Gas Processors Suppliers Association; 2004.

[7] Dawodu OF, Meisen A. Effects of composition on the performance of alkanolamine blends for gas sweetening. Chemical Engineering Communications. 1996; 144 (1):103-12.

[8] Carey TR, Hermes J.E, Rochelle GT. A model of acid gas absorption/stripping using methyldiethanolamine with added acid. Gas Separation & Purification. 1991;5(2):95-109.

[9] Lammers J, Haringa J, Littel R. Effect of polyhydroxyalcohols on CS absorption in aqueous methyldiethanolamine. The Chemical Engineering Journal and the Biochemical Engineering Journal. 1995; 60 (1): 123-9.

[10] Devai I, DeLaune RD. Emission of reduced malodorous sulfur gases from wastewater treatment plants. Water environment research. 1999:203-8.

[11] Glasscock DA, Critchfield J.E, Rochelle GT. CO_2 absorption/desorption in mixtures of methyldiethanolamine with monoethanolamine or diethanolamine. Chemical engineering science. 1991; 46(11): 2829-45.

[12] Behroozsarand A, Shafiei S. Optimal control of amine plant using non-dominated sorting genetic algorithm-II. Journal of Natural Gas Science and Engineering. 2010; 2 (6): 284-92.

[13] Sohbi B, Meakaff M, Emtir M, Elgarni M. The using of mixing amines in an industrial gas sweetening plant. World Academy of Science, Engineering and Technology. 2007; 31(1): 301-5.

[14] Maddox RN. Gas conditioning and processing. Vol. 4: gas and liquid sweetening.1982.

یک روش جدید برای افزایش جداسازی اسید گازی از گاز طبیعی با استفاده از مخلوط محلول‌های آمینی

- ابولفضل غریبی خراجی

دانشجوی دکتری مهندسی شیمی، دانشکده فنی و مهندسی، دانشگاه اصفهان، اصفهان، ایران

- وحید مددی اورگانی*

* نویسنده مسئول، استادیار گروه مهندسی شیمی، دانشکده فنی و مهندسی، دانشگاه یاسوج، کد پستی: ۸۱۹۵۷–۱۳۸۴۷، یاسوج، ایران

(ایمیل نویسنده مسئول: **v.madadi@yu.ac.ir**)

- پرویز درویشی

استادیار گروه مهندسی شیمی، دانشکده فنی و مهندسی، دانشگاه یاسوج، کد پستی: ۸۱۹۵۷–۱۳۸۴۷، یاسوج، ایران

چکیده

استفاده از مخلوط محلول‌های آمینی در واحد شیرین‌سازی گاز هزینه‌های عملیاتی و نرخ خوردگی را کاهش می‌دهد. این در حالی است که این مخلوط‌ها مقدار گوگرد در جریان گاز خروجی از واحد شیرین‌سازی را افزایش می‌دهد و وارد واحد بازیافت گوگرد می‌شود. واحد شیرین‌سازی گاز پالایشگاه گازی بیدبلند با نرم‌افزار Hysys شبیه‌سازی شده است. نتایج حاصل از این شبیه‌سازی تطابق خوبی با داده‌های صنعتی موجود از این واحد دارد. پارامترهایی مانند مقدار دی‌اکسید کربن در گاز شیرین، مقدار گاز سولفید هیدروژن در جریان گاز خروجی از واحد دفع و ورودی به واحد احیاء گوگرد، مقدار محلول آمین غنی‌شده و بار حرارتی بازجوشاننده به ازای نرخ گردش محلول آمین برای ده نمونه مخلوط آمینی متشکل از دی‌اتانول آمین و متیل دی‌اتانول آمین مقایسه شده است. مطابق با پارامترهای خاص تکنیکال، مخلوط آمینی با درصد اجزاء ۴۰ درصد وزنی متیل دی‌اتانول آمین و ۱۰ درصد وزنی دی‌اتانول آمین به عنوان بهترین مخلوط آمینی جهت شیرین‌سازی گاز در پالایشگاه گاز بیدبلند بدست آمده است.

واژگان کلیدی: واحد شیرین‌سازی، پالایشگاه گاز بیدبلند، نرم‌افزار **Hysys**، مخلوط آمینی، سولفید هیدروژن

جایگزینی چرخه شیمیایی احتراق به جای کوره در فرآیند تبدیل بخار با استفاده از کاتالیست مس

- صدیقه کبیری

کارشناسی ارشد مهندسی شیمی- کارمند منطقه ۵ عملیات انتقال گاز

- محمد رضا رحیم پور

دکتری مهندسی شیمی -استاد دانشگاه شیراز بخش مهندسی شیمی

چکیده

این مقاله، به بررسی مدل سازی راکتور کوپلینگ حرارتی دو واکنش کاتالیستی ریفرمینگ متان با بخارآب و چرخه شیمیایی احتراق جهت بهبود میزان تولید هیدروژن می پردازد. کوپلینگ حرارتی دو واکنش گرماگیر و گرماده باعث بهبود بازده حرارتی و در نتیجه افزایش میزان تولید میشود. ریفرمینگ متان با بخارآب فرآیندی گرماگیر است که گرمای آن توسط یک کوره فراهم می شود. در این حالت، لوله های ریفرمرتحت تنش حرارتی بالایی قرار دارند. با جایگزینی این کوره با چرخه شیمیایی احتراق برانیم تا علاوه بر حل این مشکل تولید هیدروژن را در یک فرآیند کوپلینگ افزایش دهیم. چرخه شیمیایی احتراق نوعی احتراق غیر مستقیم است که از دو راکتور هوا و سوخت تشکیل شده است. در این فرآیند از تماس مستقیم سوخت با اکسیژن جلوگیری می شود و شرایط برای واکنش سوخت با یک اکسید فلز فراهم می شود. کوپل این دو واکنش کاتالیستی در یک راکتور سه لوله هم مرکز انجام می شود. راکتور درونی و بیرونی به ترتیب به عنوان راکتورهای هوا و سوخت چرخه شیمیایی احتراق و راکتور میانی راکتور ریفرمینگ متان منظور می شود. راکتور چرخه شیمیایی احتراق بستر متحرک است که مس در آن کاتالیست متحرک است. راکتور ریفرمینگ متان بستر ثابت است که از کاتالیست نیکل پر شده است. شبیه سازی فرآیند با استفاده از یک مدل یک بعدی هتروژن انجام شد. صحت مدل انجام شده با داده های راکتورریفرمینگ متان پالایشگاه گاز زاگرس عسلویه بررسی شد. نتایج حاصل با موارد مشابه در راکتور معمولی ریفرمینگ متان مقایسه شد که افزایش چشمگیر میزان هیدروژن مشاهده شد.

واژگان کلیدی: تولید هیدروژن، ریفرمینگ متان با بخارآب، چرخه شیمیایی احتراق ، کاتالیست نیکل و مس

کاهش مصرف انرژی در واحدهای شیرین‌سازی گاز طبیعی توسط محلول MDEA از طریق اصلاحات ساختاری

- امید صباغ – میثم وحیدی فردوسی – محمد علی فنائی

گروه مهندسی شیمی، دانشگاه فردوسی مشهد

چکیـــــده

در این مقاله، اثر اصلاحات ساختاری بر میزان انرژی مصرفی واحد تصفیه گاز پالایشگاه بیدبلند (اولین پالایشگاه گاز ایران) مورد ارزیابی قرار گرفته است. بدین منظور، از نرم‌افزار Aspen HYSYS (V.8.3) بر پایه روش مبتنی بر سرعت (rate-based)، برای شبیه‌سازی واحد مذکور استفاده شده است. نتایج نشان می‌دهد، درصورتی که میزان CO_2 در گاز ترش ورودی کمتر از ۲ درصد بوده و محلول MDEA نیز به عنوان حلال در نظر گرفته شود، استفاده از برج جذب چند خوراکه، مخلوط‌کننده استاتیکی و جریان جانبی برج جذب، نمی‌تواند منجر به کاهش انرژی مصرفی گردد. این در حالی است که در شرایط مذکور، استفاده از جریان جانبی برج احیاء و یک واحد تبخیر آنی، می‌تواند تا حدود ۱۰ درصد انرژی مصرفی کل واحد را کاهش دهد.

واژگان کلیدی: **Aspen HYSYS**، بهینه سازی ساختاری، **MDEA**، مصرف انرژی، شیرین سازی گاز طبیعی

تاثیر نرمال پارافین ها و رسوبات آسفالتینی بر کشش بین سطحی نفت/گاز، حین تزریق گاز دی اکسید کربن به مخازن نفتی آسفالتینی

- مسعود ریاضی، یوسف کاظم زاده، رفعت پارسایی

بخش مهندسی نفت، دانشگاه شیراز

چکیده

رسوب آسفالتین در مخازن همواره مشکلات متعددی را به همراه داشته است. بنابراین شناخت دقیق مکانیزم رسوب لازمه مقابله با آن می باشد. روش های متعددی جهت شناسایی رسوب آسفالتین وجود دارد. یکی از این روش ها، روش ناپدید شدن کشش بین سطحی می باشد. در این روش با ترسیم نمودار کشش بین سطحی تعادلی بر حسب فشار، مکانیزم رسوب تشریح داده می شود.

در این مطالعه به منظور بررسی دقیق تر رسوب آسفالتین در مخازن نفتی با استفاده از نمودارهای کشش بین سطحی بر حسب فشار، از محلول های سینتیتیک متشکل از تولوئن و نرمال پارافین ها استفاده می شود. به این منظور، محلول های با ترکیب درصد متفاوت از تولوئن و نرمال پارافین هایی همچون نرمال دکان و نرمال هپتان یک بار در حضور آسفالتین استخراج شده از نفت خام و یک بار در عدم حضور آن ساخته می شود. سپس کشش بین سطحی تعادلی آن محلول ها با گاز دی اکسید کربن در فشارهای مختلف اندازه گیری می شود. با ترسیم نمودارهای کشش بین سطحی بر حسب فشار، نقطه شروع رسوب آسفالتین و پارامتر های مختلف موثر، مورد بررسی قرار می گیرد. با توجه به نتایج آزمایش ها، حضور آسفالتین در محلول های سینتیتک باعث تغییر در مقادیر و روند نمودار کشش بین سطحی بر حسب فشار می شود. بدین صورت که افزوده شدن آسفالتین به یک محلول از تولوئن و نرمال پارافین باعث می شود کشش بین سطحی محلول و گاز دی اکسید کربن بر حسب فشار در دو بازه ی مختلف با دو شیب مختلف افت می کند. نتایج تایید می کند که افزایش نرمال پارافین ها باعث تشدید رسوب آسفالتین می شود و همچنین با افزایش میزان رسوبات آسفالتنی موجود در محلول ها، شدت رسوب آن ها نیز افزایش می یابد.

واژگان کلیدی: رسوب آسفالتین، استخراج آسفالتین، کشش بین سطحی، کمترین فشار امتزاجی، تزریق گاز، نرمال پارافین

تغییر ترشوندگی سنگ مخازن گاز میعانی در نواحی نزدیک به چاه به منظور کاهش انسداد مایع، از طریق پوشش‌دهی سنگ با نانوسیال دارای خاصیت ابر آبگریزی و ابر نفت‌گریزی ساخته شده بر پایه‌ی نانوکامپوزیت ZnO/SiO_2

- پوریا اسماعیل‌زاده، محمدتقی صادقی

دانشگاه علم و صنعت ایران، دانشکده مهندسی شیمی، تهران، ایران

- علیرضا بهرامیان

دانشگاه تهران، انستیتو مهندسی نفت، تهران، ایران

چکیده

در مخازن گاز میعانی بر اثر کاهش فشار مخزن به زیر فشار نقطه‌ی شبنم هیدروکربوری سیال مخزن، میعانات گازی از فاز گاز جدا شده، به فاز مایع منتقل می‌شود و در نواحی اطراف چاه تجمع می‌یابند. در صورت بروز این پدیده که به انسداد میعانی مرسوم است نفوذپذیری نسبی فاز گاز و در نتیجه نرخ تولید گاز از چاه به شدت کاهش می‌یابد. یکی از روش‌هایی که پتانسیل قابل توجهی برای رفع این پدیده و افزایش بهره‌دهی چاه در اختیار دارد تغییر ترشوندگی سنگ مخازن گاز میعانی از حالت مایع‌دوست به گازدوست می‌باشد. در این مقاله، از نانوسیالی حاوی نانوکامپوزیت سنتز شده‌ی ZnO/SiO_2 و مواد فلئوردار TFE، PFOS و PTFE برای تغییر ترشوندگی سنگ کربناته‌ی مخزن گاز میعانی از حالت شدیداً مایع‌دوست به حالت ابر آبگریز و ابر نفت‌گریز توأم (ابرگازدوست) استفاده شد. بطوریکه زاویه تماس آب‌نمک و نمونه میعانات گازی روی سطح سنگ از ۰° قبل از پوشش‌دهی، به‌ترتیب به ۱۶۲° و ۱۳۵° درجه پس از پوشش‌دهی با نانوسیال افزایش یافتند. بعلاوه، پسماند زاویه تماس و همچنین زاویه‌ی لغزش آب روی سطح پوشش‌داده شده به ترتیب برابر ۰° و ۲۰°> اندازه‌گیری شد که نشان می‌دهد سنگ پس از پوشش دهی با این نانوسیال دارای خاصیت خودتمیزشوندگی شده است. مشخصه‌یابی سطح سنگ به‌وسیله‌ی آنالیزهای SEM، SP و EDX نشان داد که زبری نانوکامپوزیت ZnO/SiO_2 با مورفولوژی ترکیبی شامل نانوصفحات و نانوذرات کروی، به همراه انرژی سطحی پایین مواد حاوی فلئور سبب بوجود آمدن حالت ابرگازدوستی در سنگ شده است. در ادامه، عملکرد این نانوسیال به‌منظور تغییر ترشوندگی مغزه‌ی کربناته از حالت شدیداً مایع‌دوست به حالت ابر گازدوست تحت شرایط عملیاتی مخزن، با انجام آزمایش‌های جریان سیال در سیستم گاز/مایع از طریق تزریق تک فازی مایع به درون مغزه‌ی اشباع شده از گاز مورد مطالعه قرار گرفت. نتایج آزمایش‌ها نشان داد که تحرک‌پذیری مایع در هر دو سیستم گاز/آب‌نمک و گاز/میعانات گازی بطور قابل ملاحظه‌ای پس از تغییر ترشوندگی سنگ افزایش یافت.

واژگان کلیدی: گازدوست- تغییر ترشوندگی- نانوسیال- نانوکامپوزیت ZnO/SiO_2 - مخزن گاز میعانی- مایع‌گریز

یک طراحی نوین برای مبدل های حرارتی صفحه ای در چرخه مایع سازی تولید LNG

- الهام محمدی
- محمدرضا جعفری نصر*

گروه مهندسی شیمی، دانشکده فنی و مهندسی، واحد علوم و تحقیقات، دانشگاه آزاد اسلامی، تهران، ایران

(*ایمیل نویسنده مسئول: drnasr50@yahoo.ca)

چکیده

تولید ال ان جی(LNG)، فرآیند فشرده و پیچیده ای است که بیش از نیمی از هزینه های آن مربوط به بخش مایع سازی است. در سالهای اخیر مهندسان طراح، تلاش های زیادی جهت بهینه سازی این فرآیند نموده اندکه هدف عمده آنها تلاش در افزایش بازده، بالابردن ظرفیت تولید و به حداقل رساندن هزینه ها بوده است. مهمترین تجهیزات فرآیندی در بخش مایع سازی، مبدل های حرارتی فشرده از نوع صفحه ای یا حلزونی هستند. این مقاله ضمن تشریح شبیه سازی سیکل مایع سازی پروژه ایران ال ان جی با مبرد مخلوط سه گانه به ارائه روشی نوین جهت طراحی مبدل حرارتی صفحه ای به کار رفته در این سیکل پرداخته است. همچنین روشی ساده، برای انتخاب بهترین سطح ثانویه بر اساس توسعه مفهوم شاخص عملکرد حجم(VPI) معرفی گردیده است. مبدل طراحی شده، کمترین سطح و حجم را بدست داده و کاهش سطح انتقال حرارت در آن نقش عمده ای بر کاهش هزینه های سرمایه گذاری فرآیند تولید ال ان جی داشته است. سیکل مایع سازی ایران ال ان جی به بعنوان یک مورد صنعتی در این مطالعه بطورکامل در نظر گرفته شده است. شبیه سازی، سطوح حرارتی سمت سرد و گرم مبدل صفحه ای به کار رفته درفرایند مورد نظر را به ترتیب ۳۰۰۱ m^2 و ۱۹۳۳ m^2 و ضریب کلی انتقال حرارت $425\ W/m^2\ K^{\circ}$ نشان میدهد. در حالیکه با انجام طراحی این مبدل و توسعه الگوریتم طراحی سریع(RDA)، کاهش قابل ملاحظه ای در سطوح سرد و گرم لازم بترتیب به میزان ۵/۲ و ۳/۳ برابر و افزایش ضریب کلی انتقال حرارت ۲ برابر حاصل شده است.

کلمات کلیدی: گاز طبیعی مایع شده، شاخص عملکرد حجم، الگوریتم طراحی سریع

Journal of Gas Technology . Volume 2 . May 2017

1 **A Novel Design for Plate Heat Exchangers in LNG Liquefaction Cycle**
M.R. Jafari Nasr, E. Mohammadi

2 **Wettability Alteration in Near-Wellbore Regions of Gas Reservoirs to Mitigate Liquid Blockage Using Super Water- and Oil-Repellent ZnO/SiO_2 Nanofluid Treatment**
Pouriya Esmaeilzadeh, Mohammad Taghi Sadeghi, Alireza Bahramian

3 **Asphaltene and Normal Paraffin Effect On Gas-Oil Interfacial Tension During CO_2 Injection Into Asphaltenic Oil Reservoir**
Masoud Riazi, Yousef Kazemzadeh, Rafat Parsei

4 **Reducing Energy Consumption in Gas Purification Plants (MDEA Base) by Retrofit Design**
Omid Sabbagh, Maissam Vahidi Ferdowsi, Mohammad Ali Fanaei

5 **Utilizing Chemical Looping Combustion instead of Fired-Furnace in a Steam Methane Reforming for Enhancement of Hydrogen Production in a multi Tubular Reactor**
Sedigheh Kabiri, Mohammadreza Rahimpour

6 **A New Method to an Enhance Separation of Acid Gas from Natural Gas by Mixed Amine Solution**
Abolfazl Gharibi Kharaji, Vahid Madadi Avergani , Parviz Darvishi